# Advanced Manufacturing Systems

## Part 1

Edited by
Daoguo Yang, Tianlong Gu, Huaiying Zhou,
Jianmin Zeng and Zhengyi Jiang

TRANS TECH PUBLICATIONS

# Advanced Manufacturing Systems

Edited by
Daoguo Yang
Tianlong Gu
Huaiying Zhou
Jianmin Zeng
Zhengyi Jiang

# Advanced Manufacturing Systems

Selected, peer reviewed papers from the
International Conference on
Manufacturing Science and Engineering
(ICMSE 2011),
April 9 - 11, 2011, Guilin, P.R. China

*Edited by*

**Daoguo Yang, Tianlong Gu, Huaiying Zhou,
Jianmin Zeng, Zhengyi Jiang**

Trans Tech Publications Ltd
Laubisrutistr. 24
CH-8712 Stafa-Zurich
Switzerland
http://www.ttp.net

Volumes 201-203 of 3-vol.-set
*Advanced Materials Research*
*ISSN 1022-6680*

Full text available online at *http://www.scientific.net*

***Distributed** worldwide by*

Trans Tech Publications Ltd
Laubisrutistr. 24
CH-8712 Stafa-Zurich
Switzerland

Fax: +41 (44) 922 10 33
e-mail: sales@ttp.net

*and in the Americas by*

Trans Tech Publications Inc.
PO Box 699, May Street
Enfield, NH 03748
USA

Phone: +1 (603) 632-7377
Fax: +1 (603) 632-5611
e-mail: sales-usa@ttp.net

# The 2011 International Conference on
# Manufacturing Science and Engineering
# (ICMSE 2011)

## Sponsored by

Guangxi University, China
Guilin University of Electronic Technology, China

University of Wollongong, Autralia

Korea Maritime University, Korea

Hong Kong Industrial Technology Research Centre (ITRC), Hong Kong

## Conference Organization

## Consultative Committee

Academician Prof. Baixin Liu, Tsinghua University, China

Academician Prof. Bingheng Lu, Xi'an Jiao Tong University, China

Academician Prof. Baicheng Liu, Tsinghua University, China

Academician Prof. Yu Zhou, Harbin Institute of Technology, China

Prof. Shandong Tu, East China University Of Science And Technology, China

Prof. Weidong Huang, Northwestern Polytechnical University, China
Prof. Guoning Qi, Zhe Jiang University, China
Prof. Yushun Fan, Tsinghua University, China

## Co-Chairmen

Prof. Jianmin Zeng, Guangxi University, China
Prof. Huaiying Zhou, Guilin University of Electronic Technology, China

Prof. Tianlong Gu, Guilin University of Electronic Technology, China

Prof. Daoguo Yang, Guilin University of Electronic Technology, China

Prof. Zhengyi Jiang, University of Wollongong, AU

Prof. Yun-Hae Kim, Korea Maritime University, Korea

Prof. Shanqing Li, Research Institute, Baosteel, China

## Local Organizing Committee

Prof. Deguang Cao, Guangxi University, China

Prof. Taoshen Li, Guangxi University, China

Prof. Fuyun Liu, Guilin University of Electronic Technology, China

Dr. Mark Fong, Hong Kong Industrial Technology Research Centre

Mrs. Min Xu, Guilin University of Electronic Technology, China

## Technical and Organizing Committee

Prof. Tianlong Gu, Guilin University of Electronic Technology, China

Prof. Xianghua Liu, Northeastern University, China

Prof. Jingtao Han, University of Sci. and Tech. Beijing, China

Prof. Kaiming Wu, Wuhan University of Science and Technology

Prof. Zhengyi Jiang, University of Wollongong, AU

Prof. AKM Nurul Amin, International Islamic University, Malaysia

Prof. Carlos Caceres, The University of Queensland, Australia

Dr. Chunsheng Lu, Curtin University of Technology, Australia

Prof. Lin He, Guizhou University, China

Prof. Jun Wang, Northeastern University, China

Prof. Qiang Wang, University of Jinan, China

Prof. Shao Hui Yin, Hunan University, China

Prof. Wenlei Sun, Xinjiang University, China

Prof. Chun Liang Zhang, Guangzhou University, China

Prof. Jinglong Bu, Hebei Polytechnic University， China

Prof. Xiaoming Jia, Hebei Polytechnic University, China

Prof. Jianmin Zeng, Guangxi University, China

Prof. Daoguo Yang, Guilin University of Electronic Technology, China
Prof. Huarui Xu, Guilin University of Electronic Technology, China
Prof. Yuan Gao, Guilin University of Electronic Technology, China

Prof. Yun-Hae Kim, Korea Maritime University, Korea

Prof. Junyou Shi, Qingdao University of Science & Technology, China

Prof. Yin Biao Guo, Xiamen University, China

Prof. Ming Dong, Shanghai Jiao Tong University, China

Prof. Wenbo Du, Beijing University of Technology, China

Prof. Hongzhen Guo, Northwestern Polytechnical University, China

Prof. Wenji Xu, Dalian University of Technology, China

Prof. Shiming Ji, Zhejiang University of Technology, China

Dr. Dongbin Wei, University of Wollongong, Australia

Prof. Geun Jo Han, Dong-A Univeristy, Korea

Dr. Gui Wang, The University of Queensland, Australia

Prof. Jong Kook Lee, Chosun University, Korea

Prof. Ken-ichi Manabe, Tokyo Metropolitan University, Japan

Prof. Jeng-Haur Horng, National Formosa University, Taiwan

Prof. Jianzhong Zhou, Jiangsu University, China

Prof. Xiaoqin Zhou, Jilin University, China

Prof. Wenjun Meng, Taiyuan University of Science and Technology, China

Prof. Haoran Geng, University of Jinan, China

Prof. Shuguang Gong, Xiangtan University, China

Prof. Yijian Huang, Huaqiao University, China

Prof. Changhe Li, Qingdao Technological University, China

Prof. Cheng Li, Zhengzhou University, China

Prof. Jialu Li, Tianjin Polytechnic University, China

Prof. Zhiyi Liu, Central South University, China

Prof. Yongcheng Lin, Central South University, China

Prof. Xiaoping Liao, Guangxi University, China

Prof. Deping Liu, Zhengzhou University, China

Prof. Jia-Horng Lin, Feng Chia University, Taiwan

Prof. Kyung-Man Moon, Korea Maritime University, Korea

Dr. Mark Fong, Hong Kong Industrial Technology Research Centre

Prof. P. S. Pa, National Taipei University of Education, Taiwan

Prof. Sagar Kamarthi, Northeastern University, USA

Prof. Meihong Liu, Kunming University of Science and Technology, China

Prof. Dehong Lu, Kunming University of Science and Technology, China

Prof. Yongjin Chen, KunMing University of Science and Technology., China

Prof. Shaojian Ma, Guangxi University, China

Prof. Qingsen Meng, Taiyuan University of technology, China

Prof. Furen Xiao, Yanshan University, China

Prof. Kailin Pan, Guilin University of Electronic Technology, China

Prof. Jingang Qi, Liaoning University Of Technology, China

Prof. Pengcheng Wang, Inner Mongol University of Technology, China

Prof. Shoujun Wang, Tianjin University of Technology, China

Prof. Shahrum Abdullah, University Kebangsaan Malaysia, Malaysia

Prof. Toshio Haga, Osaka Institute of Technology, Japan

Prof. Walid Mahmoud Shewakh, Beni Suef university, Egypt

Dr. Yuantong Gu, Queensland University of Technology, Australia

Prof. Yu-Shiang Wu, China Univerisity of Sci. and Tech., Taiwan

Prof. Jun Xiao, Wuhan University of Technology, China

Prof. Ligang Yao, Fuzhou University, China

Prof. Zhaohui Zhang, Beijing Jiaotong University, China

Prof. Xiaoping Zhou, Hubei University Of Technology, China

Prof. Jian Gao, Guangdong University of Technology, China

Prof. Changsheng Li, Northeastern University, China

Prof. Xiaoming Sang, Hebei Polytechnic University, China

Prof. Ping Zou, Northeastern University, China
Prof. Zhihai Han, Xi’an Jiao Tong University, China

# Preface

The International Conference on Manufacturing Science and Engineering is the premier forum for the presentation of new advances and research results in the fields of Manufacturing Science and Engineering. The conference brings together leading researchers, engineers and scientists in the domain of interest from around the world. The 1st International Conference on Manufacturing Science and Engineering, ICMSE 2009, was successfully held from Dec. 26 -28, 2009 at Zhuhai, China. The 2nd international conference on Manufacturing Science and Engineering, ICMSE 2011, is held in Guilin, China, between 9 and 11 April 2011. Delegates from more than 20 countries or districts attended those conferences.

The present volumes provide up-to-date, comprehensive and worldwide state-of-the art knowledge of the manufacturing science and engineering, including: manufacturing process technology, advanced engineering materials, new and advanced materials, advances in mechanical design and advanced manufacturing systems. All papers included in those volumes have already passed the strict peer-reviewing by 2-5 expert referees and been accepted for publication.

The editors hope that those volumes will not only provide the readers a broad overview of the latest advances but also provide the researchers a valuable summary and reference in this field.

We would like to express our sincere appreciations to all the authors for their contributions to those books. We are indebted to all the referees for their constructive comments on the papers. Thanks are also given to Trans Tech Publications for producing those volumes.

*Prof. Daoguo Yang*
*Guilin University of Electronic Technology, China*

*Prof. Tianlong Gu*
*Guilin University of Electronic Technology, China*

*Prof. Huaiying Zhou*
*Guilin University of Electronic Technology, China*

*Prof. Jianmin Zeng*
*Guangxi University, China*

*Prof. Zhengyi Jiang*
*University of Wollongong, Australia*

# Table of Contents

## 1. CAD/CAM/CAE

## 2. Energy Storage and Energy Development

## 3. Mining Machinery Manufacturing

## 4. New Energy Equipment and Manufacturing

## 5. Cloud Manufacturing and Extreme Manufacturing

## 6. Bio-Manufacturing

## 7. Enterprise Informationization

## 8. Integrated Manufacturing System

## 9. Quality and Safety of Products

## 10. Products Processing and Storage

## 11. Production and Operation Management

## 12. Industrial Design

## 13. Engineering Optimization

## 14. Product Design and Development

## 15. Quality Monitoring and Control of Manufacturing Process

## 16 Metallurgy Engineering

## 17. Industrial Robotics and Automation

## 18. Measure Control Technologies and Intelligent Systems

## 19. Transmission and Control of Fluid

## 20. Mechanical Control and Information Processing Technology

## 21. Embedded System

## 22. Other Related Topics

# 1. CAD/CAM/CAE

*Advanced Materials Research Vols. 201-203 (2011) pp 3-8*
*© (2011) Trans Tech Publications, Switzerland*
*doi:10.4028/www.scientific.net/AMR.201-203.3*

# Hot-Stamping Process Simulation and Optimize Research for Collision Beam of Automobile Door

Chao Wang [1, a], Bin Zhu [1, b], Yisheng Zhang [1, c], Jie Shi [2, d], Han Dong [2, e]

[1]State Key Laboratory of Material Processing and Die and Mould Technology, Huazhong University of Science and Technology, Wuhan 430074, China

[2]Central Iron and Steel Research Institute, National Eng. Research Center of Advanced Steel Technology, Beijing, 100081, China

[a]wangchao8321@163.com, [b]zhubin26@gmail.com, [c]zhangys@mail.hust.edu.cn, shijie@nercast.com, [e]donghan@nercast.com

**Keywords:** Advanced High-Strength Steel; Hot-Stamping; Finite Element; Simulation; Coupled Thermo-Mechanical; Collision Beam

**Abstract:** Hot-stamping molding for ultra-high-strength steel have some similarities with traditional cold-stamping molding in the aspects of molding process and die design. But due to the effect of temperature variation of blank, hot-stamping have some differences in ultra-high-strength products design, material selection and forming process design. Some special forming defects, such as local thinning, cracking and wrinkling, could appear in hot-stamping process due to these differences. In order to obtain uniform phase structure and get high-quality products, it is very important to be able to predict and control the blank temperature and the consistence of blank cooling rate. The thermo-mechanical characteristics of hot-stamping are studied with the material of ADVANCE1500 (22SiMnTiB). Based on the results of simulations and experiments, conclusion are drawn that the complexity of the product and the blank which contacts with die asynchronously causes the uneven distribution of the blank temperature. This is the key factor that leads to the poor mobility of the blank material and local thinning, cracking, wrinkling and other defects in forming process. Proper clearance between punch and die can reduce the probability of defects which could contribute to the improvement of hot-stamping process.

## Introduction

In the modern automotive industry, the use of ultrahigh-strength steels in structural and safety components is rapidly increasing in order to meet the steadily rising requirement for vehicle safety and reducing environmental pollution in the automotive industry[1]. However, traditional cold stamping process will bring on a large amount of residual stress retaining in shaped component which may result in severe spring-back after cold-stamping. Moreover, in traditional cold stamping process, great forming force is generated and complex shapes can hardly be formed[2].

In hot stamping process, the blanks are completely austenitized at temperature of between 900ºC and 950ºC for about four to ten minutes inside a continuous-feed furnace and subsequently transferred to an internally cooled die set via a transfer unit. At high temperature, the material has excellent formability, so that complex shapes can be formed in a single stroke. The blanks are stamped and cooled down under pressure for a specific amount of time according to the sheet thickness after drawing depth is reached. During this period the shaped part is cooled in the closed die set which is internally cooled at a cooling speed, and completing martensitic transformation. Finally, the part leaves the hot-stamping about 150 ºC and with high mechanical properties: an ultimate tensile strength of 1500MPa or much higher and little spring-back [3-5]. chematic of hot-stamping process is shown in Fig.1 and finite element model of Collision beam is shown in Fig.2.

In this paper, ADVANCE1500 is selected as AHSS, and the finite element analysis is used to research the result and get the solution which leads to the defects of collision beam during the process of hot-stamping.

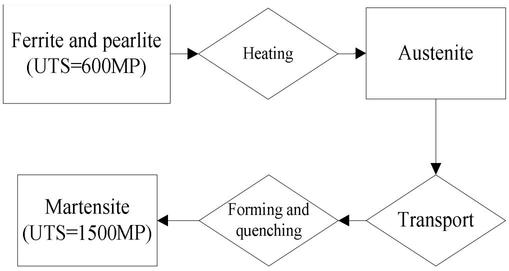

Figure 1 Schematic of hot-stamping process

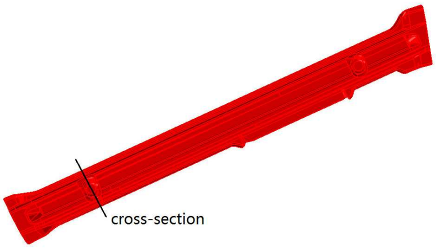

Figure 2 Finite element model of Collision beam

## Hot-stamping FE model of collision beam

**Definitions of material properties for hot-stamping process.** The shaped parts of the collision beam sizing 1300mm × 300mm have low drawing depth which made up of several complex surfaces. This could bring a great deal of difficulty in forming blanks into collision beam components. So hot stamping process is selected which could overcome most difficulty. The thickness of the blank is 1.8mm. The gap between punch and die at the end of quenching is 2mm. The coefficient of friction between mould and blank is 0.3. The drawing depth of experiment and simulation is 35mm.

ADVANCE-1500 is selected as experimental materials. The chemical analysis of the ADVANCE- 1500 steel is given in Table 1. In order to get reliable modeling and numerical simulation of hot-stamping process, the determination of the thermo-mechanical material properties is one consideration. Besides, it is more important to consider the relationship between stress and strain by temperature. This relationship was estimated by hot tensile tests on GLEEBLE mechanical system and the constitution equation has been generated according this relationship. The thermal conductivity between blank and mould change with the pressure and clearance between blank and die[6]. The other material properties are given in Table1 to Table 4.

$$\sigma = K\varepsilon^{m} \tag{1}$$

where：

$$\mathrm{m} = 0.3515(\mathrm{Z/A})^{0.0434}, \mathrm{K} = 353.58(\mathrm{Z/A})^{0.094}, \mathrm{Z} = \mathrm{A}[\ln\sinh(\alpha\sigma_{\varphi})], A = 1.27E20, a = 0.00373$$

Table 1 Chemical analysis of ADVANCE1500

| C | Si | Mn | Ti | B | Mo | S | p |
|---|---|---|---|---|---|---|---|
| 0.2 | 0.85 | 1.64 | 0.022 | 0.001 | 0.01 | 0.001 | 0.005 |

Table 2 Coefficients of heat conduction at different temperatures

| Temperature, ºC | 20 | 100 | 200 | 400 | 600 | 800 |
|---|---|---|---|---|---|---|
| Heat conduction, W/(m·K) | 50.1 | 46.1 | 44.8 | 39.8 | 34.3 | 26.4 |

Table 3 Young's modulus at different temperature

| Temperature, ºC | -20 | 20 | 100 | 150 | 200 | 300 | 400 | 450 | 475 | 600 | 850 |
|---|---|---|---|---|---|---|---|---|---|---|---|
| Young's modulus, GPa | 208 | 205 | 203 | 200 | 196 | 186 | 170 | 158 | 151 | 6.5 | 5.9 |

Table 4 Coefficients of thermal expansion at different temperatures[7]

| Temperature, ºC | 100 | 200 | 300 | 400 | 850 | 900 | 950 |
|---|---|---|---|---|---|---|---|
| Thermal expansion,/ºC×10-5 | 1.93 | 1.97 | 2.12 | 2.17 | 2.62 | 2.78 | 3.08 |

Table 5 Specific heats at different temperatures

| Temperature, ºC | 50 | 100 | 400 | 850 | 900 |
|---|---|---|---|---|---|
| Specific heat, J/(kg·K) | 465 | 471 | 479 | 987 | 1019 |

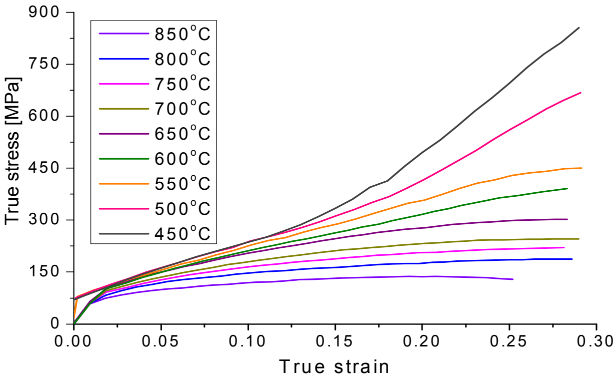

Figure 3 Influence of the temperature on flow curve

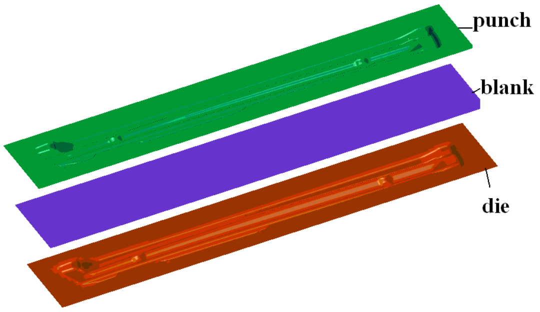

Figure 4 Schematic illustration of tools and blank used within hot-stamping process

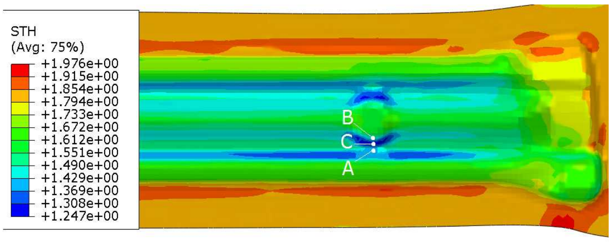

Figure 5 Thickness distribution at the end of holding stage

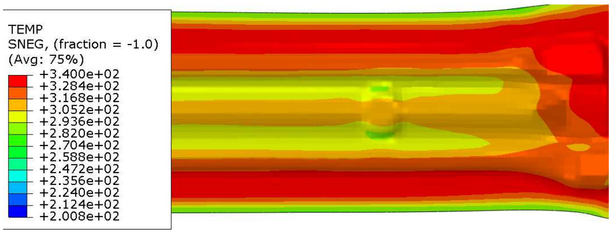

Figure 6 Temperature distribution at the end of holding stage

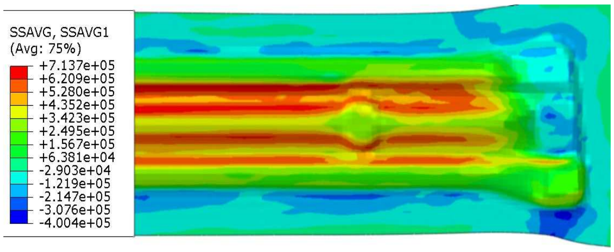

Figure 7 Mises stress distribution at the end of holding stage

Figure 8 Experiment result of hot-stamping of collision beam

**Definitions of analysis steps.** In hot stamping process, excessive BHF could rapidly cool down the blank and hold back the material flow which would bring on risks of component cracking. So in this hot-stamping experiments and simulations, it is unnecessary to use the model that does not have BHF (Figure 4) though this would acquire a component of severe wrinkling in some areas. The hot-stamping of collision beam may divide into following three stages: a. Heating and transportation.(at this stage, the blank is heated up to 850°C - 900°C in oven and fully austenitic, and is delivered to the mould by mechanical equipment). b. Forming stage (at this stage, punch move down and the blank is adequately shaped). c. Holding stage (at this stage, the shaped component is hold in the mould for about 6 seconds, cools rapidly and quenches simultaneously). Figure 5 shows the displacement-time curve in direction of punch movement at forming stage and holding stage.

## Result and Analysis

**Analysis of formability.** According to the results of simulation (Figure 6), the shaped component appears obvious thinning areas at the corner of protruding zones (point out in Figure 6), the thickness of the thinnest area has decline 30% and reach 1.247mm. Figure 5 shows the distribution of shaped component temperature at the end of holding stage. It can be seen that the protruding zones (point A and point B in Figure 5) of the shaped component has good contact with mould and cools down more rapidly than other zones. Some of the protruding zones have cooled to 200°C below. Figure 7 shows the distribution of Mises stress. The thinnest area in Figure 5 (point C in Figure 5) also have greatest Mises stress, reaching up to 713.8MPa (Figure6-c). So the places near point C (in Figure 5) have greater possibility of cracking than other places. Figure 8 shows the shaped component in experiment. It can be seen that the component also appears local cracking in the same zone compared with the simulation results.

**Analysis of Contact.** In order to clearly observe the contacts between blank and mould, the internal temperature distribution of the mould and shaped component, stress and strain distribution during the forming stage and holding stage, a cross-section simulation has been performed. The position of the cross-section has been pointed out in Figure 2. This cross-section is across the cracking areas, the results of which can contribute to explaining the reason of cracking.

Figure 9 shows the simulation results of cross-section temperature distribution at the end of forming stage and holding stage (points A, B, C in Figure 9 point out the same spots on the blank compared with the points A, B, C in Figure 6). It can be seen that the protruding zones (point A and B in Figure 9) of the blank which have intimate contact with mould have good thermal conductivity condition and cool down more rapidly than the areas nearby (point C). In addition, point A and point B take priority over point C of contacting with mould first and material near point A and B flow slowly due to the effect of friction. This would result in reducing the thickness of point C. Thus, a gap could occur between blank and mould (shown in Figure 9-c). So the areas near point C would have bad contact with the mould and have higher temperature than the areas nearby. Moreover, the fact that pre-defined gap between blank and mould is larger than the thickness of blank is another key reason for the appearance of local gap between blank and mould after forming.

Figure 10 shows the cross-section stress distribution at the end of holding stage. It can be seen that the areas near the point C have great amount of residual stress. As shown in Figure 9-a, at the end of forming stage, the temperature of most part of the blank is still above the recrystallization temperature. So the residual stress can reduce during this period of time. As the temperature drops, thermal expansion coefficients of the blank significantly reduced and the blank shrinks, while protruding zones (like point A and B in Figure 9-c) in good contact with mould would hinder the process of shrinkage. Thus, the part between protruding zones would get a pull force and the residual stress could increase, which would increase the risks of crack at that part.

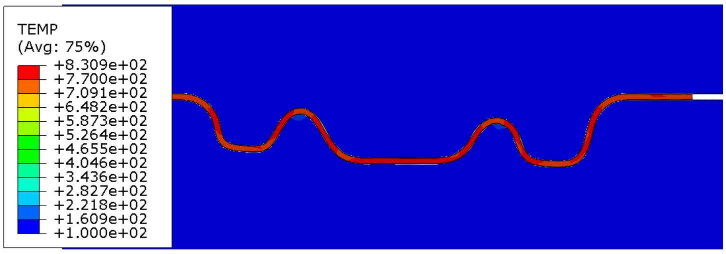

a. cross-section temperature distribution at the end of forming stage

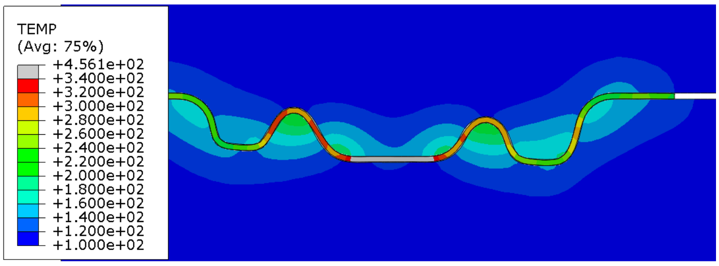

b. cross-section temperature distribution at the end of holding stage

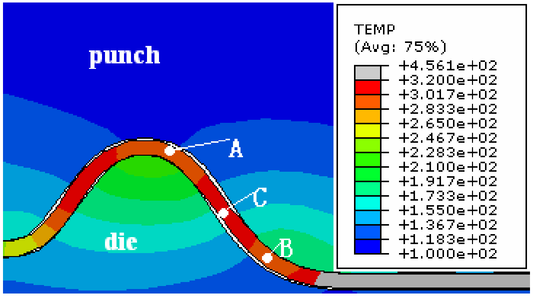

c. Enlargement of cross-section temperature distribution at the cracking position at the end of holding stage

Figure 9 Cross-section temperature distribution at the end of forming stage and holding stage

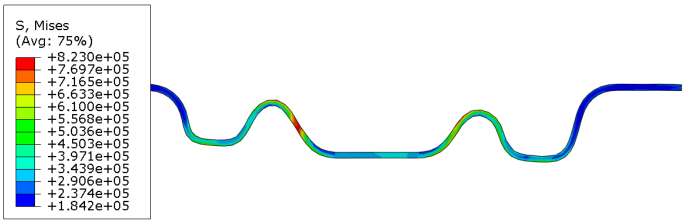

Figure 10 Cross-section stress distribution at the end of holding stage

## Analysis of gap between punch and die

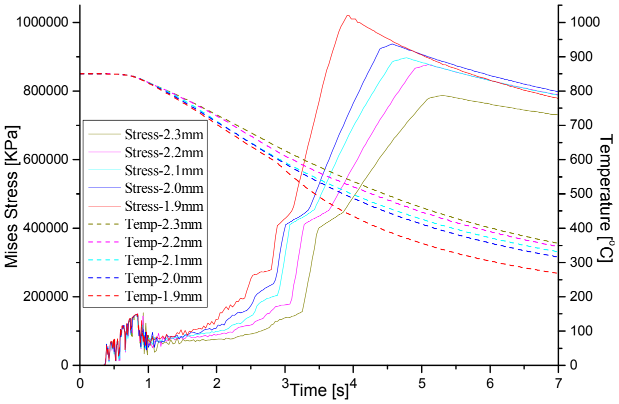

Figure 11 The stress and temperature curves at different time on local cracking areas

In order to ensure the success of hot-stamping, there must be a gap between punch and die which could affect the quality of the shaped component. Figure 11 shows the stress and temperature curves at different time on local crack part (point C in Figure 9-c). The left and right vertical axis represents strain and temperature respectively. The solid line and dotted line represent stress curve and temperature curve. As can be seen from figure, with the gap increasing between punch and die, the cooling rate at pint C decreases and the residual stress at the end of holding stage also gradually declines. Moreover, there is a dramatic growth in stress near 600ºC at the holding stage. The reason might be that the microstructure of the blank transforms from austenite to martensite near 600ºC which leads to the sudden increase of Young's modulus and yield strength. In addition, the shaped component appears spring-back during the cooling period of time, which results in dramatic increasing in stress. The maximum stress is over 1GPa. As shown in Figure 11, with increasing of the clearance between punch and die, the stress at point C decreases. But oversize clearance will make the blank forming incomplete and get unqualified components. So proper gap between punch and die can reduce the residual stress and risks of shaped component cracking after forming and get qualified components.

## Conclusion

(1) It is the fact that the different areas of the blank contact with the mould in sequence make the shaped component uneven temperature distribution. Thus the local cracking appears. The first-contact areas on the blank cool down rapidly and have poor mobility. This would make the post-contact areas which are between the first-contact areas greatly thin by the pull force which could leads to the appearance of clearance between punch and die. So the thermal conductivity of post-contact areas decreases. Because of the rapid cooling and uneven temperature distribution, the first-contact areas harden and the microstructure transforms form austenite into martensite. Under the effect of the thermal expansion and contraction, the residual stress of the post-contact areas gradually increases. This would lead to the increase of cracking risks. The experimental results of hot-stamping also prove the conclusion above.

(2) It can reduce the risks of cracking after forming stage to change the clearance size between punch and die. With the reduction of the clearance between punch and die, the cooling rate of blank increase and the residual stress grows at the end of holding stage. Then the risks of cracking increase. But oversize clearance will make the blank forming incomplete and get unqualified components. So it can effectively reduce the risks of the local crack to adjust the clearance size between punch and die. This can provide the reference for the process design of hot-stamping.

## Reference

[1] Merklein, M., Lechler, J., Geiger, M.: CIRP Annals - Manufacturing Technology. 2006, 55(1): 229-232.

[2] Turetta, A., Bruschi, S., Ghiotti, A.: Journal of Materials Processing Technology. 2006, 177(1-3): 396-400.

[3] Firat, M.: Materials and Design. 2007, 28(4): 1311-1320.

[4] Firat, M.: Materials and Design. 2007, 28(4): 1298-1303.

[5] Firat, M.: Materials and Design. 2007, 28(4): 1304-1310.

[6] Naderi, M., Uthaisangsuk, V., Prahl, U., Bleck, W.: Steel Research International. 2008, 79(2): 77-84.

[7] Liu.: Journal of Materials Engineering and Performance. 2010.

*Advanced Materials Research Vols. 201-203 (2011) pp 9-14*
*© (2011) Trans Tech Publications, Switzerland*
*doi:10.4028/www.scientific.net/AMR.201-203.9*

# The Interpolation Algorithm of Feed Rate Control Based on Trigonometric Acceleration-Deceleration and Machine Dynamics Conditions

Lei Jiang[a], Guofu Ding[b], Binbin Xie[c] and Jianmin Wang[d]

Southwest Jiaotong University, Chengdu 610031, P.R. China

[a]jianglei0506@163.com, [b]dingguofu@163.com, [c]xiebb5688@163.com,
[d]wjm_20040812@163.com

**Keywords:** Feed Rate Control; Trigonometric Acceleration-Deceleration Condition; Machine Dynamics Condition; NURBS Curve; Interpolation

**Abstract.** According to the requirements of high-speed machining, the feed rate control algorithm based on the acceleration-deceleration control and dynamics conditions is proposed. This algorithm not only satisfies the continuity of displacement, feed rate, acceleration and jerk of the feed movement, but also meets the dynamics condition of high-speed machining. Furthermore, the algorithm is applied to NURBS curve interpolation and optimizes the acceleration-deceleration intervals. At last, the algorithm is verified by simulation. This interpolation algorithm of feed rate control reduces the impact, machine vibration of feed, and improves the surface accuracy and quality of high-speed machining.

## Introduction

High-speed machining means cutting with high speed and high feed rate. It has many advantages such as high cutting efficiency, high surface quality, long tool life, small cutting force and so on. High-speed machining has been widely used in aerospace manufacturing. At present, more and more parts with complex surfaces become the cutting object of high-speed machining. NURBS curve can describe geometry characteristics of cutting surface completely. Therefore, the feed path expressed by NURBS interpolation command is the programming development of high-speed machining.

High-speed machining requires machine tools to have high motion precision. And it demands higher requirements of acceleration-deceleration controlling ability for feed rate frequent changes due to the tool path curvature frequent change. How to achieve the control goals of machining smoothly and quickly is the key question of high-speed machining development. Currently, the acceleration-deceleration control has linear, exponential, parabola, S curve, higher functions algorithm and so on[1-5]. Although these algorithms could make feed rate smooth, there still have mutation in acceleration or jerk. And it can not completely avoid the feed impact of high-speed machining.

In this paper, acceleration-deceleration control algorithm based on trigonometric condition and machine dynamics condition is proposed. The control algorithm is used in NURBS interpolation calculation to realize the optimization of acceleration-deceleration intervals. This algorithm can not only guarantee the continuity of feed movement displacement, velocity, acceleration and jerk in high-speed machining, but also meet the dynamics demands of machine tools.

## The algorithm of feed rate control

Meeting the acceleration-deceleration conditions of trigonometric function and machine dynamics is the sufficient condition to achieve the continuity of feed movement displacement, velocity, acceleration and jerk, stability of cutting process in high-speed machining.

**Trigonometric acceleration-deceleration condition.** The goal of acceleration-deceleration control algorithm is to achieve the smoothness of displacement, velocity, acceleration, jerk of the feed path. This goal demands displacement function has third-order derivative at least, which ensures the machine can reach predetermined position at predetermined feed rate shock-free and vibrationless. Trigonometric function has infinite derivatives, so constructing a triangular acceleration-deceleration function can achieve these goals. In this paper, using the monotone increasing characteristic of cosine function in $[\pi, 2\pi]$, we construct the acceleration function as:

$$a(t)=\frac{1}{2}\left[\cos\left(\frac{2t}{t_m}-1\right)\pi+1\right]a_{\max} \tag{1}$$

where $a_{max}$ is the maximum acceleration, $t$ is time variable, $t_m$ is the whole time of acceleration process. Acceleration function meets the demands that the acceleration-deceleration interval is monotone and the accelerations at start and end are zero.

Define $v_1$, $v_2$ as the feed rates at start and end respectively. Integrating Eq. (1) we can obtain the feed rate function:

$$v(t)=v_1+\int_0^t a(t)dt=v_1+\left[\frac{t_m}{2\pi}\sin\left(\frac{2t}{t_m}-1\right)\pi+t\right]\frac{a_{\max}}{2} \tag{2}$$

and

$$t_m=\frac{2(v_2-v_1)}{a_{\max}} \tag{3}$$

Deviating Eq. (2) we obtain feed jerk function:

$$J(t)=-\frac{a_{\max}\pi}{t_m}\sin\left(\frac{2t}{t_m}-1\right)\pi \tag{4}$$

Integrating Eq. (2) we obtain the feed displacement function:

$$S(t)=\int_0^t v(t)dt=v_1t+\frac{a_{\max}}{2}\left[\frac{t^2}{2}+\frac{t_m^2}{4\pi^2}\cos\left(\frac{2t}{t_m}-1\right)\pi\right] \tag{5}$$

From Eq. (1), (2), (4), we know that trigonometric acceleration-deceleration condition divides the whole accelerating process into increasing-acceleration section $OT_1$ and decreasing-acceleration section $T_1T_2$, as shown in Fig. 1(a). For the same reason, the whole decelerating process is divided into increasing-deceleration section $OT_1$ and decreasing-deceleration section $T_1T_2$, as shown in Fig. 1(b).

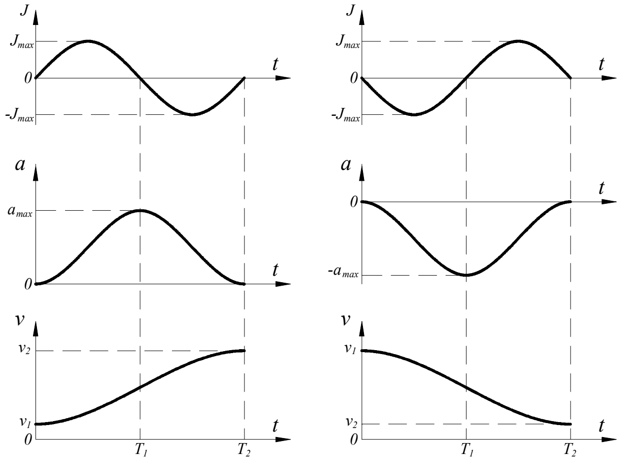

(a) Accelerating process (b) Decreasing process

Fig. 1 Kinematic graphics of trigonometric acceleration-deceleration

**Machine Dynamics Condition.** Machine feed includes rotation of screw and linear motion of table. We define the total mass of the table and workpiece as $m$, screw lead as $l$, rotational inertia as $I$, motor angular velocity as $\omega$, angular acceleration as $\varepsilon$, table linear feed rate as $v$, linear acceleration as $a$, axial cutting force as $F_c$, the servo motor maximum output torque as $M_{max}$. The motor shaft torques equivalent to inertia force, cutting force and resistance are defined as $M_i$, $M_c$ and $M_f$ respectively. We can obtain the following machine dynamics condition function[6]:

$$\begin{cases} M_i = -\operatorname{sgn}(a) I_e \varepsilon = -\operatorname{sgn}(a)\left(I + I'\right)\varepsilon = -\operatorname{sgn}(a)\left(I + m\left(\dfrac{l}{2\pi}\right)^2\right)\dfrac{2\pi a}{l} = -\operatorname{sgn}(a)\left(\dfrac{2\pi I}{l} + \dfrac{ml}{2\pi}\right)a \\ M_c = \dfrac{F_c l}{2\pi} \\ M_f = \dfrac{F_f l}{2\pi} \\ \left|M_i + M_c + M_f\right| \le M_{\max} \end{cases} \tag{6}$$

Affected by the depth of cutting, feed rate and cutting speed, $F_c$ could be simplified as

$$F_c(t) = -\operatorname{sgn}(v) K_c |v|^{\alpha} \tag{7}$$

where $K_c$ is the cutting force factor relatives to the feed rate.

Taking Eq. (7) into (6), we can obtain the machine dynamics constraint function of single axis:

$$\left| -\operatorname{sgn}(a_j)\left(\frac{2\pi I_j}{l_j} + \frac{m_j l_j}{2\pi}\right)a_j + \frac{l_j}{2\pi}\left(-\operatorname{sgn}(v_j) K_c \left|v_j\right|^{\alpha}\right)\right| \le M_{j\max} \tag{8}$$

where $j$ represents $X$, $Y$, $Z$ axis, $a_j$, $v_j$ represent $a$, $v$ projection in the axis of $j$.

## NURBS curve interpolation algorithm

NURBS curve could be expressed as a sub-vector rational function, the rational expression is

$$\mathbf{P}(u) = \frac{\sum_{i=0}^{n} B_{i,k}(u) W_i V_i}{\sum_{i=0}^{n} B_{i,k}(u) W_i} \tag{9}$$

where $V_i$ is the control points, $W_i$ is the control point weighting factor, and $B_{i,k}(u)$ is the basis function for the $k$ times B-spline.

**NURBS curve pre-interpolation.** The purpose of NURBS pre-interpolation is to obtain interpolation parameters and initial interval distribution. Based on Taylor series expansion, NURBS pre-interpolation parameter function is[7]:

$$u_{i+1} = u_i + \frac{S_i}{\left\|\dfrac{dp(u)}{du}\right\|_{u=u_i}} - \frac{\Delta L^2 \left(\dfrac{dp(u)}{du} \cdot \dfrac{d^2 p(u)}{du^2}\right)}{2\left\|\dfrac{dp(u)}{du}\right\|^4_{u=u_i}} + O(T^3) \tag{10}$$

where $S_i$ is step length of the $i$ interpolation cycle, $T$ is interpolation cycle and $v_i$ is instantaneous feed rate of the $i$ interpolation cycle (default is instructions rate $v_c$).

Every interpolation points are at NURBS curve, so there is no radial error. However, due to chord substitute curve in each interpolation cycle, there still has approximate error as following:

$$\delta_i = \rho_i - \sqrt{\rho_i^2 - \left(\frac{f_i}{2}\right)^2} \tag{11}$$

where $\rho_i$ is curve radius of the $P(u_i)$ point.

The maximum feed rate, which satisfies the precision of $i$ interpolation cycle could be expressed as:

$$v_{\delta i} = \frac{2\sqrt{2\rho_i\delta - \delta^2}}{T} \tag{12}$$

and normal acceleration is:

$$a_{ni} = \frac{v_{\delta i}^2}{\rho_i} \tag{13}$$

Define $a_{ni_j}$, $v_{\delta i_j}$ represent the projection of $a_{ni}$, $v_{\delta i}$ in the $j$ axis respectively. Taking them into (4), we can obtain the maximum feed rate satisfies the condition of $j$ axis dynamics. To satisfy the dynamics condition of three feed axes, the feed rate restricted by machine dynamics conditions is:

$$v_{a_n i} = \min\left\{v_{\max a_n i_j}\right\} \tag{14}$$

Define the instruction feed rate as $v_c$, the instantaneous feed rate of the $i$ interpolation cycle as $v_i = \min\left\{v_{\delta i}, v_{a_n i}, v_c\right\}$. If $v_i < v_c$, taking $v_i$ into the Eq. (11), we can obtain the $u_{i+1}$ amended. At the same time, we can obtain feed length sequence of each interpolation cycle. Through pre-interpolation, the feed rate will be changed in the interval where the curvature is large, so the intervals of different feed rate appear.

**NURBS curve interpolation.** The purpose of NURBS interpolation is to amend the feed rate under trigonometric acceleration-deceleration conditions.

**Acceleration-deceleration interval.** By analyzing NURBS parameters and feed rate sequence of pre-interpolation, we can obtain the parameters of the acceleration-deceleration intervals. Usually it starts by the constant feed rate $v_c$ to deceleration, then accelerate to $v_c$. At the maximum curvature point, it reaches minimum feed rate, i.e. the end of deceleration and the start of acceleration.

**The $a_{max}$ of trigonometric acceleration-deceleration.** The normal and tangential acceleration of feed motion is interaction achieved by $X$, $Y$, $Z$ axes. From Eq. (5), we know that the largest tangential acceleration is at the mid-point of interval. Therefore, we can obtain the $a_{max}$ of trigonometric acceleration-deceleration algorithm by calculating the minimum of the largest tangential accelerations of 3 axes, i.e. $a_{max} = \min\{\, a_{j\tau max} \,\}$ at the mid-point of interval. From Eq. (8), we can obtain:

$$a_{j\tau\max}\boldsymbol{\tau}_j + a_n\boldsymbol{n}_j = a_{jmax} = \left|\frac{M_{j\max} - \dfrac{l_j}{2\pi}\left(-\operatorname{sgn}(v_j)K_c\left|v_j\right|^{\alpha} + u_jN_j + \mu_jv_j\right)}{\left(\dfrac{2\pi I_j}{l_j} + \dfrac{m_jl_j}{2\pi}\right)}\right| \tag{15}$$

where $a_n$, $a_\tau$ are the normal and tangential acceleration respectively. $\boldsymbol{n}_j$, $\boldsymbol{\tau}_j$ are the unit normal and tangential vector component of $j$ axis at interval midpoint.

According to the acceleration $a_{max}$, we can obtain new feed rate sequence of interpolation cycle in each acceleration-deceleration interval from Eq. (2). According to Eq. (5), (10), we can interpolate from start to end of the intervals by trigonometric function.

**The correction of acceleration-deceleration intervals.** Through the interpolation of NURBS, we can obtain parameters of interpolation and feed rate that contain a series of acceleration-deceleration intervals. Because the interpolation processes are calculated independently, it may modify intervals even interfere with adjacent one as the results of the start and end feed rates, acceleration and other limiting factors. It is necessary to correct it.

Define *F*, *B* as the forward and backward adjacent acceleration-deceleration intervals, the corresponding parameters of NURBS are [$u_{F_1}, u_{F_2}$], [$u_{B_1}, u_{B_2}$], the start and end feed rates are [$v_{F_1}, v_{F_2}$], [$v_{B_1}, v_{B_2}$], the maximum accelerations are $a_{\max_F}$, $a_{\max_B}$ respectively and $v_{F_2} = v_{B_1}$, $u_{F_1} < u_{B_1}$. According to above parameters, the intervals could be divided into two types:

(1) Type 1 $u_{F_2} \le u_{B_1}$

Type 1 refers the intervals are not interfering, as shown in Fig. 2. In this case, the feed rates meet the actual movement requirements. It needs no correction of the interpolation intervals.

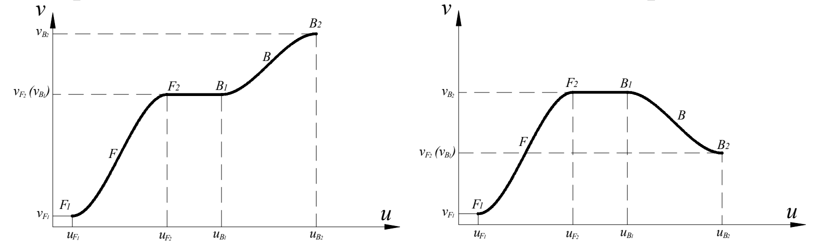

Fig. 2 Type 1

(2) Type 2 $u_{B_1} < u_{F_2}$

Type 2 refers the two adjacent intervals that interfere partly or even complete overlap. The physical meaning is the feed rate cannot attain the predetermination in the interval due to $a_{max}$ limitation. In this case, interpolation must be corrected to ensure that there is no interference between adjacent intervals. Using iteration method to construct new intervals that combine the original ones, it makes the whole process continuous and smooth.

There are 3 cases of adjacent intervals based on $u_{B_1} < u_{F_2}$.

Case 1 is $a_{\max F} \cdot a_{\max B} < 0$ and $u_{B_1} < u_{F_2} < u_{B_2}$, as shown in Fig. 3. The parameters of new interval are [$u_{F_1}, u_{B_2}$], the start and end feed rates are [$v_{F_1}, v_{B_2}$] respectively.

Case 2 is $a_{\max F} \cdot a_{\max B} < 0$ and $u_{B_2} \le u_{F_1}$, as shown in Fig. 4. The parameters of new interval are [$u_{F_1}, u_{F_2}$], the start and end feed rates are [$v_{F_1}, v_{B_2}$] respectively.

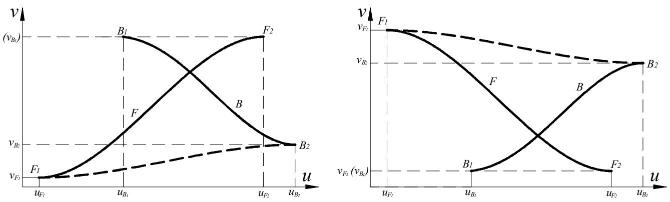

Fig. 3 Case 1 of type 2

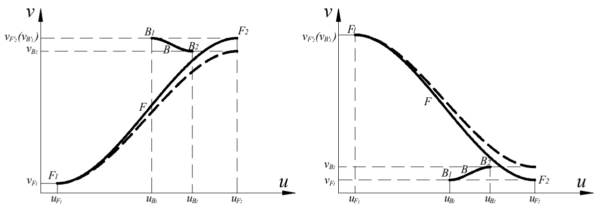

Fig. 4 Case 2 of type 2

The other cases are $a_{\max F} \cdot a_{\max B} > 0$ and $u_{B_1} \le u_{F_2} \le u_{B_2}$ or $a_{\max F} \cdot a_{\max B} > 0$ and $u_{B_2} \le u_{F_2}$, as shown in Fig. 5. The start and end feed rates of new interval are [ $v_{F_1}$ , $v_{B_2}$ ] respectively, $a_{\max} = \min(a_{\max F}, a_{\max B})$, and the parameter of start is $u_{F_1}$.

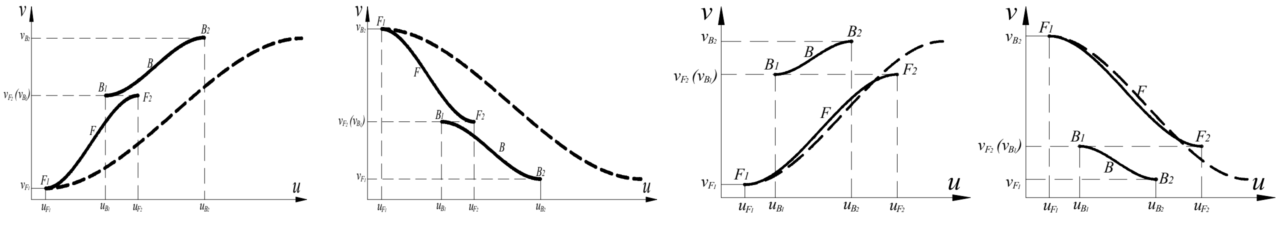

Fig. 5 The other cases of type 2

After constructing new intervals to combine the original ones, the intervals may still intervene with subsequent ones, and it need to continually compare and correct it to ensure all the adjacent interval types are $u_{F_2} \le u_{B_1}$. At last, we can obtain the new interval parameters by Eq. (2), (5) and (10).

## Example

We choose a third-order NURBS curve as the interpolation example, as shown in Fig. 7.

Suppose interpolation cycle as 0.001s, interpolation accuracy as 0.001mm, command feed rate as 300mm/s, each motor power as 400W, the mass of each axis as 50kg, screw lead as 5mm. Fig. 8, Fig. 9 are the contrast charts of normal interpolation and new interpolation algorithm. It shows new control algorithm adjusts feed rate in the large curvature point and makes feed rate, acceleration smooth.

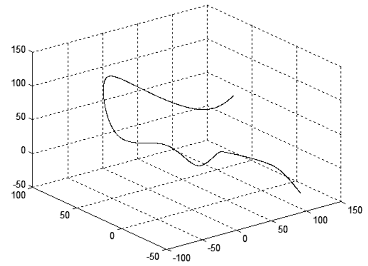

Fig. 7 NURBS curve

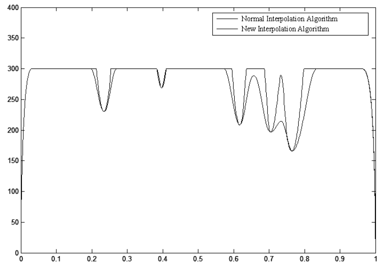

Fig. 8 Feed rate comparison chart

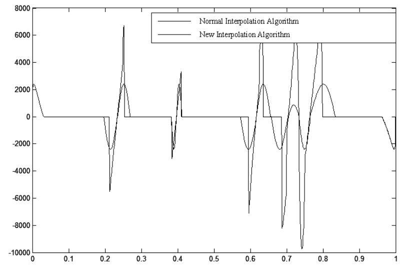

Fig. 9 Acceleration comparison chart

## Conclusion

In this paper, the feed rate control algorithm based on trigonometric acceleration-deceleration and machine dynamics conditions is proposed. This algorithm not only satisfies the continuity of displacement, feed rate, acceleration and jerk of the feed motion, but also meets the dynamics condition of the machine. The algorithm can applied to NURBS interpolation calculation using iteration correction technology to achieve the optimization of acceleration-deceleration intervals. The algorithm reduces the impact, machine vibration of feed motion. And it is benefit to improve the surface accuracy and quality of high-speed machining.

## Acknowledgements

This work is supported by The Young Teachers Fund of Southwest Jiaotong University, The Fund for New Century Excellent Talents of China, The Special Fund of High-end CNC Machine Tools and Basic Manufacturing Equipment of China (2009ZX04014-051-03) and The Fundamental Research Funds for the Central Universities of China (SWJTU09ZT06).

## References

[1] M C Tsai, C W Cheng, and Cheng M Y: International Journal of Machine Tools and manufacturing. Vol. 43(2003), p. 1217-1227

[2] S.Bedi, I Ali, N Quan: Transactions of the ASME Journal of Engineering for Industry. Vol. 115(1993), p. 329-336.

[3] S S Yeh and P L Hsu: Computer Aided Design. Vol. 31(1999), p. 347-359.

[4] Mi Ching Tsai, Chung Wei Cheng: Transactions of the ASME Journal of Manufacturing Science and Engineering. Vol. 125(2003), p. 449-460.

[5] Yong T, Narayanaswami R: Computer Aided Design. Vol. 35(2003), p. 1249-1259.

[6] Peng Fang-yu, He Ying, Luo Zhong-cheng, Li Bin: Huazhong Univ. of Sci. & Tech. (Nature Science Edition). Vol. 33(2005), p. 80-83, In Chinese.

[7] Du Dao-shan, Yan Cun-liang, Li Cong-xin: Journal of Shanghai JiaoTong University. Vol. 40(2006), p. 843-847, In Chinese.

*Advanced Materials Research Vols. 201-203 (2011) pp 15-23*
*© (2011) Trans Tech Publications, Switzerland*
*doi:10.4028/www.scientific.net/AMR.201-203.15*

# An Approach to Multi-Constrained 3D Modeling for Curtain Wall System Based on Spatial Point-Line Model

Zhenzhong Hu[1,a], Fangqiang Yu[2,b], Guoxing Li[3,c] and Zhongli Wang[3,d]

[1]Graduate School at Shenzhen, Tsinghua University, Shenzhen 518055, China;

[2]Department of Civil Engineering, Tsinghua University, Beijing 100084, China;

[3]Zhuhai King Glass Engineering Co. Ltd., Shenzhen 518040, China

[a]hu.zhenzhong@sz.tsinghua.edu.cn, [b]fqyu007@163.com,

[c]lgx@kge-group.com, [d] wzl@kge-group.com

**Keywords:** CAD; 3D Modeling; Curtain Wall; Multi-Constrained; Shenzhen Airport Terminal 3

**Abstract.** The accurate spatial 3D models and corresponding coordinates of every key point are needed to determine the sizes, shapes, and locations of installation for all curtain wall elements in the process of production and construction. To solve the transition problems between architectural design and construction design of curtain wall system, four kinds of single-constrained computer-aided 3D modeling algorithm for spatial point-line models were discussed in detail. Then, a multi-constrained iterative 3D modeling process was proposed by considering coupling relationships amongst the various constraints. A 3D modeling system named T3-CW-CAD was developed and applied to the Shenzhen Airport Terminal 3. The application results showed that the presented-algorithm can meet the overall demand for automatically generating multi-layer 3D models according to spatial point-line model, along with sizes and other restraints amongst curtain wall elements, therefore playing a key role in guiding the production and construction of curtain wall system.

## Introduction

After the architectural and structural designs of a modern complex building with a curtain wall system have been finished, the design of its curtain wall is needed before the whole construction drawings are printed out. Normally, the architectural design describes the outline of the building, while the structural design is intended to make the result of the architectural design bear its weight and applied loads, whereas the curtain wall design is purposed for detail determination of curtain wall elements and their relations, in order to meet the requirements in the architectural design for the appearance of commercial or large-scale public buildings. Usually, the outline of a building, which is the foundation for curtain wall design, is depicted with 3D point-line models (that is, the construction members of a building such as steel plates and glasses are represented by models made up of points and lines in 3 dimensions, with no thickness, single-layered and simplified) in its architectural design. However, in order to fabricate and install the curtain wall elements, precise 3D models and coordinates of key points are necessary for determination of the size, shape, and location of every element. Therefore, calculations concerning the curtain wall, which shall be performed according to 3D point-line models provided by the architectural designer and the interrelations between the construction elements, are needed.

## Task Description

At present, existing CAD systems for curtain wall design are mainly used for site layout of construction elements, formation of checkerwork drawing, material management and structural calculation and analysis [1, 2]. There are also researches on conceptual design of the architecture and curtain wall by conducting Building Information Model (BIM) [3, 4]. However, scanty research or application on 3D modeling of curtain wall based on the spatial point-line model, which is the general result form from architectural design. Although, some automatic methods to transform a 2D model into a 3D one have arisen, they cannot meet most of the requirements because some strict preconditions are need. For instance, some methods depend on not only the existing 2D projection views with assigned layout, but the coordinates and relations of every spatial point as well [5, 6]. For another method, coordinates transformation of engineering drawings is needed before analyzing the interrelationship among projection systems, in order to support 3D reconstruction from orthographic views [7]. However, as the result of architectural design is represented by fractals [8], it is necessary to generate the outline of each layer and coordinates of each key point on the basis of the point-line model and the interrelations among the elements and among different layers, so that detail fabrication drawings of elements and construction blueprints can be produced. In addition, 3D constraints are more complex than 2D constraints and a lot of calculation and analysis are needed for modeling under each kind of constraint. In this particular field, mature CAD systems and corresponding engineering applications are still needed.

On the other hand, there are inevitable interplays among constraints, which means a model which has been modified under one constraint may become ineffective under another constraint. To perform a modeling with more than one constraints, traditionally, Genetic Algorithm or Simulated Annealing Algorithm are used to find an optimized solution [9, 10]. However, as 3D modeling of a curtain wall calls for colossal computation, these algorithms become unsatisfactory. In this case, iterative modeling, in which the priority of each constraint is determined by discussing the relationship between them so that the constraints can be used in proper order, is applied to work out a complete 3D model.

More and more buildings' outlines become irregular as the buildings become more and more complex and their spans larger and larger, so that it is almost impossible to build up 3D models manually. Therefore, a method for computer to model rapidly is needed to aid the design and construction of curtain wall system.

In the following part of the paper, the modeling methods for four separated constraints that affects on the 3D modeling process from spatial point-line model are firstly summarized. They are intersection constraint, coplanar constraint, constraint on minimum board thickness, and constraint on the inclination. Then by analyzing the interplays among these constraints, an iterative modeling method is proposed and applied to an on-going engineering project. At last, the features of the iterative modeling method are discussed.

## 3D Modeling Method under Single Constraint

**Intersection Constraint.** Here we name planes that meet at a single intersecting point as point sharing planes. The deviated planes, which are generated based on the original point sharing planes and their own normal directions and designated displacements, usually cannot meet at one point, as shown in Fig. 1(a). However, the requirement of intersection constraint means that deviated planes based on original point sharing planes are required to be a set of new point sharing planes as shown in Fig. 1(b).

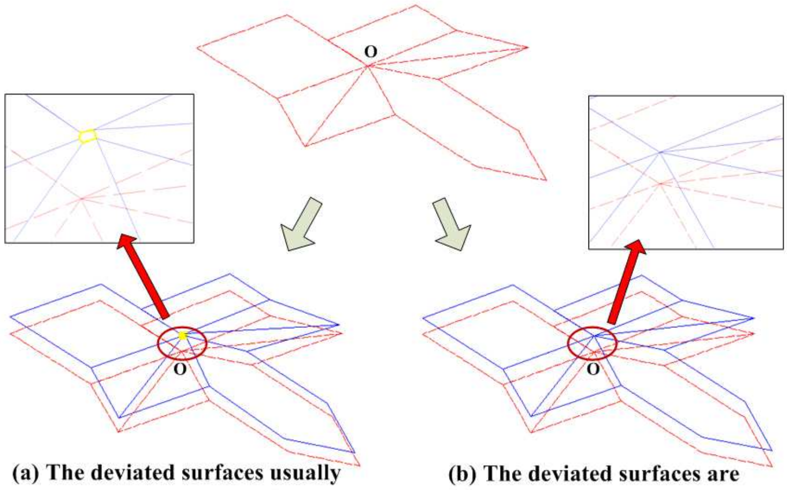

(a) The deviated surfaces usually do not meet at one point

(b) The deviated surfaces are required to meet at one point

Fig. 1 Intersection constraint of several planes

To be universally known in 3D spaces, three planes that are not paralleled determine a single intersecting point. As a result, in order to meet the requirement of intersection constraint and to determine the point where planes meet, the following steps should be adhered to.

1) Choose three reference planes according to the priority of each plane and the relations between the normal vectors of the planes (Algorithm 1);

2) Form three deviated planes by allowing the reference planes to deviate designated displacements;

3) Work out the intersecting line between two of the deviated planes (Algorithm 2);

4) Work out the intersection point between the intersecting line and the third deviated plane (Algorithm 3);

5) Set the point as the intersecting point of all the planes; see Fig. 1(b).

*Algorithm 1 (For determination of the reference planes).*

To deternine the reference planes, start from the original intersecting point (See Fig. 1), traverse its adjacent planes according to their priorities, then decide if each plane can be selected as a reference plane according to the relations of plane normals (see Fig. 2(b)). If a plane is selected, it was then added to the reference planes list. The final reference planes list can be determined if the number of the reference planes amounts to 3 or the traversing has been completed.

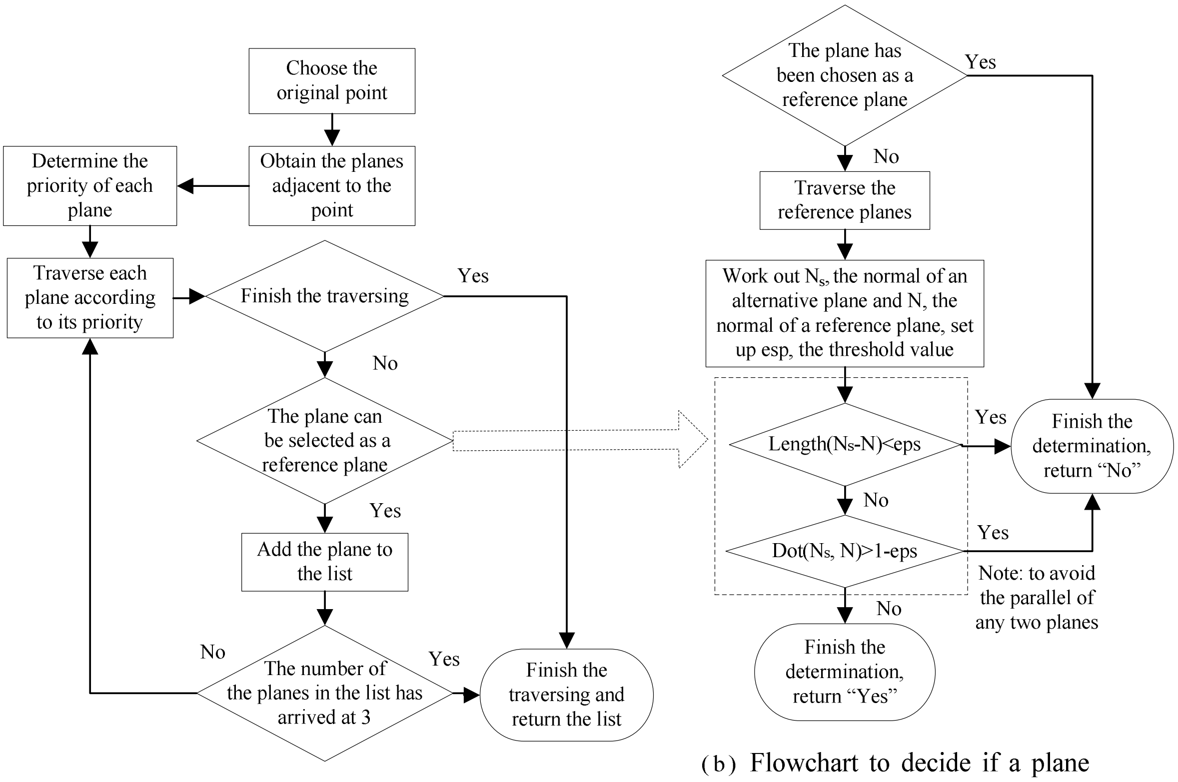

(a) Flowchart for determination of reference planes

(b) Flowchart to decide if a plane can be chosen as a reference plane

Fig. 2 Flowchart for algorithm of plane selection

*Algorithm 2 (For determination of the intersecting line of two planes).*

If $P_s$ and $P_t$ are the vertexes of two planes and U, V are their normal vectors, P is a point on the intersecting line and it is possible to set $P_z = 0$, then the following expressions will be concluded by the following Eq. 1.

$$\begin{cases} P_x = (P_s \cdot UV_y - P_t \cdot VU_y)/(U_xV_y - V_xU_y) \\ P_y = (P_s \cdot UV_x - P_t \cdot VU_x)/(U_yV_x - V_yU_x) \\ P_z = 0 \end{cases} . \quad (1)$$

Otherwise, it is possible to set $P_x = 0$ or $P_y = 0$, then the coordinates of P can be worked out in the same way.

Having known the coordinates of P, the direction of the intersecting line N can be found as Eq. 2.

$$N = U \times V . \tag{2}$$

*Algorithm 3 (For determination of coordinates of the intersecting point).*

If N is the normal vector of a plane and P is any point on the plane, $P_1$, $P_2$ are two points on a straight line and $P_t$ is the point where the plane and the straight line meet, then Eq. 3 can be concluded.

$$P_t = P_1 + t(P_2 - P_1) . \tag{3}$$

The following expression can be concluded as Eq. 4.

$$t = -(P_1 - P) \cdot N / (P_2 - P_1) \cdot N . \tag{4}$$

If the denominator in the expression is zero, it will be concluded that the straight line parallels the plane. However, if the numerator is zero, it means that $P_1$ is the intersecting point or the line is on the plane.

**Coplanar Constraint.** The points in a 3D polygon representing the outline of an element which are not in a plane will make the fabrication difficult. Therefore, it is a must to ensure the coplanarity of these points by fitting a plane and finely adjust the points so that they can meet the requirements of planar constraint.

*Algorithm 4 (For planar fitting).*

If the plane is represented by the following Eq. 5.

$$z = a_0 + a_1 x + a_2 y + e . \tag{5}$$

Replace x, y, z with the coordinates of each boundary point to work out the values of $a_0$, $a_1$, $a_2$ [11] as shown in Eq. 6.

$$\begin{bmatrix} n & \sum x_i & \sum y_i \\ \sum x_i & \sum x_i^2 & \sum (x_i \cdot y_i) \\ \sum y_i & \sum (x_i \cdot y_i) & \sum y_i^2 \end{bmatrix} \begin{Bmatrix} a_0 \\ a_1 \\ a_2 \end{Bmatrix} = \begin{Bmatrix} \sum z_i \\ \sum (x_i \cdot z_i) \\ \sum (y_i \cdot z_i) \end{Bmatrix} . \tag{6}$$

Finally, form a new plane with these values so that the boundary points of each plane become coplanar in it.

**Constraint on Minimum Board Thickness.** Normally, the deviated plane formed with the above-mentioned two methods does not parallel the original reference plane. The pipeline and other structures inside the curtain wall requires that the minimum space between the exterior surface of a board and the interior one should not be less than a specific value. Therefore, the minimum space between surfaces should be worked out and if a minimum space is not satisfactory, tiny adjustments of the coordinates shall be done. In the process as shown in Fig. 3, the foot of a perpendicular from a 3D point to a plane and the shortest distance between a point and a polygon should be worked out, which is detailed in the following Algorithm 5 and Algorithm 6.

*Algorithm 5 (For the foot of a perpendicular from a 3D point to a plane).*

If N is the normal vector of a plane , $P_{on}$ is a point on the plane, $P_t$ is a foot of a perpendicular from a P, a vertex, to the plane, then Eq. 7 can be concluded.

$$P_t = P + t \cdot N . \tag{7}$$

Then the following Eq. 8 can be concluded.

$$t = -(P - P_{on}) \cdot N / N \cdot N . \tag{8}$$

If the numerator equals to zero, it can be concluded that the vector between P and $P_{on}$ is perpendicular to the plane and the vertex is in the plane.

*Algorithm 6 (For shortest distance between a 2D point to a polygon).*

1) Decide if the point is in the plane; if yes, $d_{min}$=0; otherwise go to step 2);
2) Work out $d_i$, the minimum distance between the point and each edge of the polygon (i=1...n, n equals the number of the edges);
3) $d_{min} = \min\{d_i\}$.

**Constraint on the Inclination.** As the structure at the utmost exterior of a building, the curtain wall has to be suitable for drainage. Therefore, the polygons which do not meet the requirements on drainage must be rotated for a proper angle $\alpha$ (See Algorithm 7 for calculation of $\alpha$ ) to adjust its inclination (see Fig. 4 for flowchart of the algorithm).

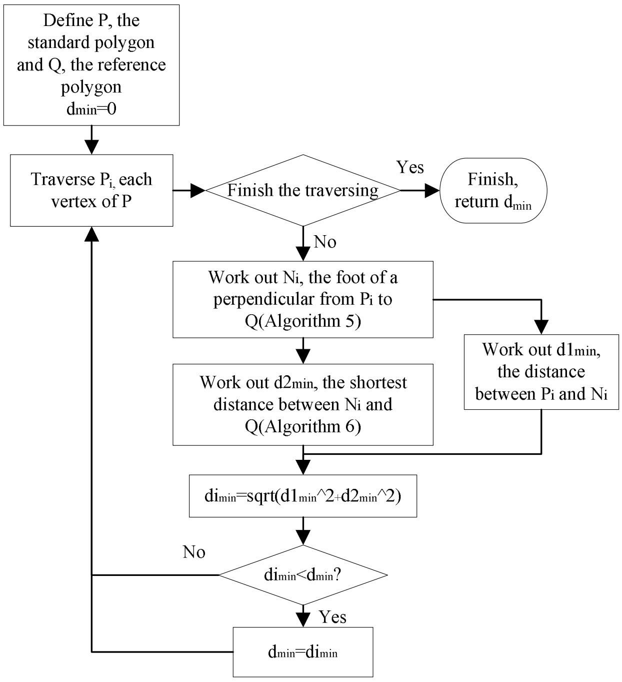

Fig. 3 Flowchart for algorithm of minimum distance calculation between two polygons

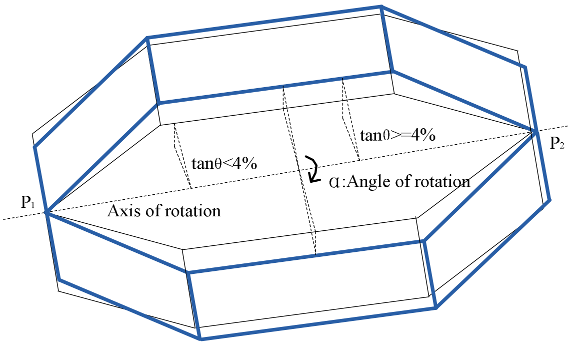

Fig. 4 Shape modification of a curtain wall element

*Algorithm 7 (For calculation of the turning angle).*

Suppose P is a 3D point whose coordinates are (x,y,z). It is rotated by $\alpha$, an angle reference to a rotation axis $P_1P_2$ to form a new 3D point P'(x',y',z'). The coordinates of $P_1$, $P_2$ are $(x_1,y_1,z_1)$, $(x_2,y_2,z_2)$. T is defined as a tranformation matrix, then Eq. 9 can be concluded:

$$\overline{P'}(x', y', z', 1) = T \cdot \overline{P}(x, y, z, 1) . \tag{9}$$

Then the following Eq. 10 can be concluded:

$$T=\begin{bmatrix}1&0&0&-x_1\\0&1&0&-y_1\\0&0&1&-z_1\\0&0&0&1\end{bmatrix}R(\alpha)\begin{bmatrix}1&0&0&x_1\\0&1&0&y_1\\0&0&1&z_1\\0&0&0&1\end{bmatrix} \tag{10}$$

Where, if $c=\cos(\alpha)$ , $s=\sin(\alpha)$ , $\vec{u}=\vec{P_2}-\vec{P_1}$ , then $R(\alpha)$ is the transformation matrix [12] for a turning around an axle passing the original point whose direction vector is $\vec{u}$ for $\alpha$ radian degree, as shown in Eq. 11.

$$R(\alpha)=\begin{bmatrix}c+(1-c)\vec{u}_x^{\,2} & (1-c)\vec{u}_y\vec{u}_x-s\vec{u}_z & (1-c)\vec{u}_z\vec{u}_x+s\vec{u}_y & 0\\(1-c)\vec{u}_x\vec{u}_y+s\vec{u}_z & c+(1-c)\vec{u}_y^{\,2} & (1-c)\vec{u}_z\vec{u}_y-s\vec{u}_x & 0\\(1-c)\vec{u}_x\vec{u}_z-s\vec{u}_y & (1-c)\vec{u}_y\vec{u}_z+s\vec{u}_x & c+(1-c)\vec{u}_z^{\,2} & 0\\0&0&0&1\end{bmatrix} \tag{11}$$

## 3D Modeling under Multi-Constraints

**Analysis of the Interplays among the Constraints.** Although the above-mentioned constraints interplay each other, not every pair of contraints have effect on each other. For example, under the coplanar constraint, the fine adjustment of vertex coordinates of a polygon is necessary, which can be done after intersection constraint takes effect, therefore, coplanar constraint doesn't go against the intersection constraint, but it may influence the inclination of an element and finely modify the minimum thickness of an element. See Table 1 for all the interplays.

Table 1 Analysis of the coupling effect amongst the constraints

| | Intersection Constraint | Coplanar Constraint | Constraint on Minimum Board Thickness | Constraint on the Inclination |
|---|---|---|---|---|
| Intersection Constraint | | | √ | |
| Coplanar Constraint | | | √ | √ |
| Constraint on Minimum Board Thickness | √ | √ | | √ |
| Constraint on the Inclination | | √ | √ | |

**Working Process for the Iterative Modeling Method.** Owing to the interplays among the constraints, which vary with the order of action, reasonable working process will greatly improve the efficiency of modeling. On the other hand, every time the model has been constrained, it is necessary to check if the model meet the requirements of the rest constraints; if no, iterative modeling method should be applied until all the requirements are met. Therefore, the working process is the key for 3D modeling of curtain wall system under more than one constraints.

Table 1 indicates that adjustment of the coordinates of the elements' vertexes to meet the requirements on minimum board thickness will lead to the fact that the modeling can not meet other constraints and vice versa. Therefore, the constraint on minimum thickness is the most important one. On the other hand, the plane fitting and plane rotation can be done after the intersection constraint has taken effect so that the fitted and rotated plane can be treated as forced plane to ease the modeling process. Based on these principles, the modeling can be done iteratively according to Fig. 5.

As illustrated in Fig. 5, model checking is done to decide whether the model meet the requirements on minimum board thickness. If yes, finish the modeling; otherwise, firstly decide if the parameters for modeling are convergent in an iterative process as below.

If $\delta_i$ is the minimum deviation value of a board thickness from requirement that determined by the following equation

$\delta_i$ = the minimum board thickness after $i^{th}$ iteration - the required minimum thickness (11)

then the parameter is considered to be convergent if $\delta_{i+1} < \delta_i$ ($\delta_{i+1}, \delta_i > 0$).

According to the interplay analysis mentioned above, as the model is under the influence of more than one constraints, the effect of a constraint on the model may be changed after another constraint on the model has been finished. For example, allowance of two surfaces to depart from each other along the normal direction so that the minimum board thickness meet the requirement will lead to unsatifactory inclination of other board for drainage. For another instance, forced intersection of several plane will influence the distances between the plane and reference plan. Under extreme condition, the requirement on the minimum thickness can not be fulfilled no matter which direct will be taken to move the intersection point, when the parameters become inconvergent. In these cases, parameters including the elements' shape, thickness, drainage inclination and drainage method, have to be modified.

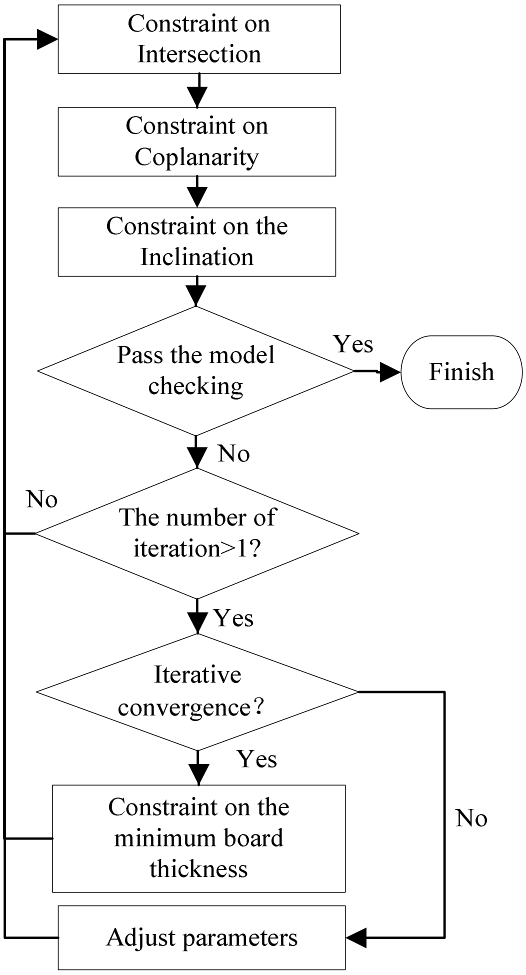

Fig. 5 Flowchart for iterative 3D modeling approach

## Engineering Application

The above-mentioned method has been applied to the modeling of the curtain wall system of the T3 terminal of Shenzhen Airport, which is a key project for expansion of the Shenzhen Airport. The curtain wall system is made up of glass panes and metal boards arranged in a way to form a special concavo-convex texture on a free formed surface. The architectural designer has given the point-line model of the curtain wall in the manner of 3D coordinates (See Fig. 6 (a)), which serves as the central line of the steel structure (See Fig. 6 (c), (d)). Multi-constrained, the inner outline and outer one of the steel boards and the glass panes have to be determined and it is a requisite that the minimum board thickness is 240 mm (See Fig. 6 (b)) and the inclinations of the glass panes be not less than 4%.

The study is based on the platforms of AutoCAD® 2007 , Visual studio .NET® and Object ARX .NET® and object-oriented modularize method is used to design and develop a CAD system (T3-CW-CAD) for the modeling of the curtain wall system of the T3 terminal of Shenzhen Airport. Fig. 7 shows the effects of the 3D modeling and iterative process at the corridor of the tower and the huge roof.

The iteration shows that the time needed for every adjustment is longer than that in previous step and the deviation of the minimum thickness from the requirement becomes smaller and smaller, which means it is a convergent process. The application indicates that the method can meet the requirements of modeling of T3 terminal, which is based on point-line model and multi-constrained.

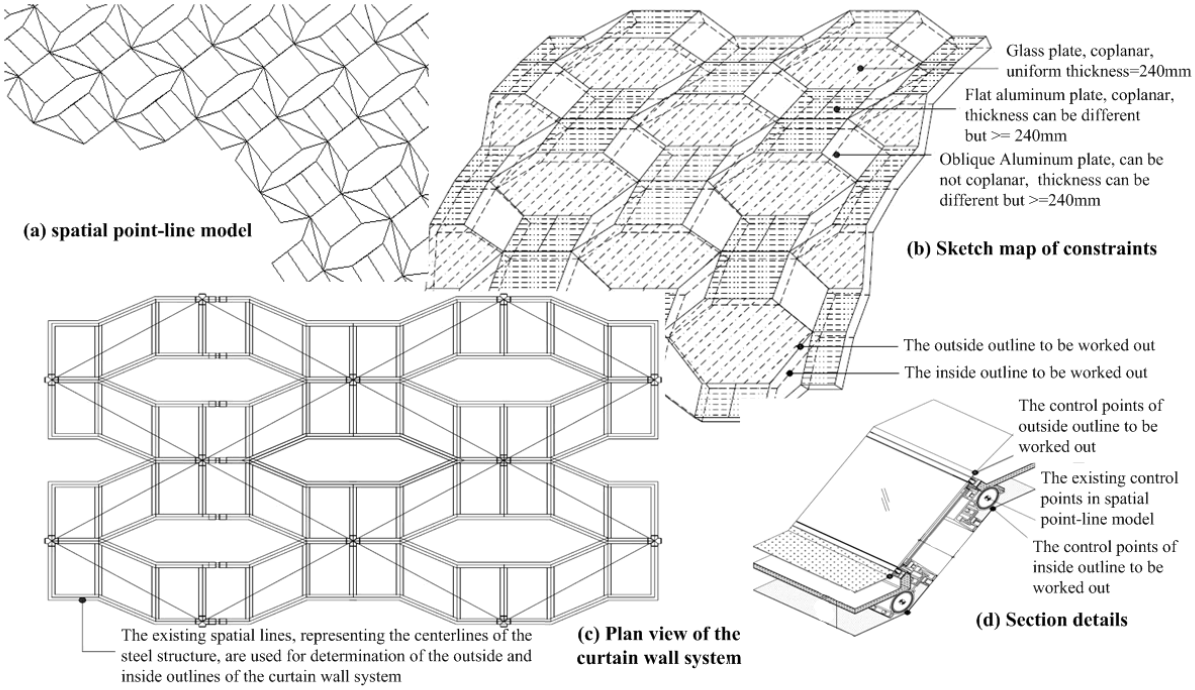

**(a) spatial point-line model**

**(b) Sketch map of constraints**

Glass plate, coplanar, uniform thickness=240mm

Flat aluminum plate, coplanar, thickness can be different but >= 240mm

Oblique Aluminum plate, can be not coplanar, thickness can be different but >=240mm

The outside outline to be worked out

The inside outline to be worked out

The existing spatial lines, representing the centerlines of the steel structure, are used for determination of the outside and inside outlines of the curtain wall system

**(c) Plan view of the curtain wall system**

The control points of outside outline to be worked out

The existing control points in spatial point-line model

The control points of inside outline to be worked out

**(d) Section details**

Fig. 6 3D modeling requirements for curtain wall system of Shenzhen Airport Terminal 3

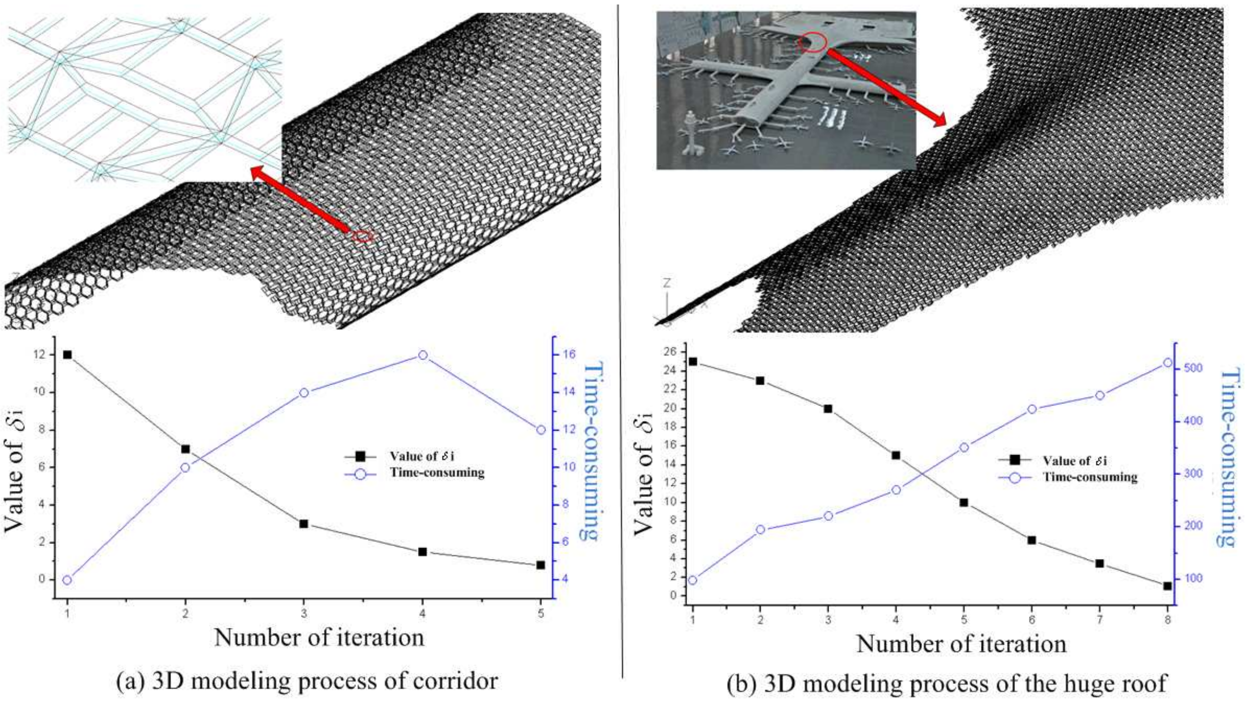

(a) 3D modeling process of corridor

(b) 3D modeling process of the huge roof

Fig. 7 Application of the iterative 3D modeling approach

## Conclusions

The modeling method presented in this paper is mainly featured by:

1) Such single constraint as intersection, coplanarity, minimum board thickness and bodily form have been respectively and cooperatively taken into the consideration;

2) The iteration will help the realization of automatic modeling and model checking process to greatly improve the efficiencies in description of the fractals of architectural design result and detailed design of the elements;

3) The 3D modeling approach can meet the requirements of the curtain wall designer that the integrative multi-layered 3D models must be produced automatically based on the point-line models and the dimensions of elements and interplays determined during the design process. Therefore, the method plays an important role in helping design construction drawing and produce the elements of curtain wall system and their installations.

## Acknowledgements

This work was supported by the National Natural Science Foundation of China (No. 51008168) and China Postdoctoral Science Foundation funded project (20090460361).

## References

[1] Jie Wu, Ming Gong, Qilin Zhang: Computer Aided Engineering, Vol. 16 (2007), p. 22-24. (In Chinese)

[2] Xiaosong Zeng, Qiong Tan: Journal of Yuzhou University (Natural Sciences Edition), Vol. 21 (2004), p. 269-271. (In Chinese)

[3] Naruo Kano, in: *Proceedings of ISAAC*, Kolkata, India, (2006), p.18-20

[4] Paola Sanguinetti: Revista del Centro de Investigación, Vol. 8(sup) (2008), p. 49-53

[5] I. V. Nagendra, U. G. Gujar: Computers & Graphics, Vol. 12 (1988), p. 111-114

[6] B. Aldefeld: Computer Aided Design, Vol. 15 (1983), p. 59-64

[7] Aijun Zhang, Changqian Zhu, Zhe Wang: Journal of Southwest Jiaotong University, Vol. 36 (2001), p. 57-61. (In Chinese)

[8] Oezguer Ediz, Guelen Cagdas: Computer Aided Design, (2007), p. 1-7

[9] K. L. Mak, Z. G. Guo, in: *IEEE Systems and Information Engineering Design Symposium*, Charlottesville, USA, (2004)

[10] Jun Lv, Boqin Feng, Bo Li: Journal of Xi'an Jiaotong University. Vol. 39 (2005), p. 1299-1302. (In Chinese)

[11] P. C. Raymond, C. C. Steve: *Numerical methods for engineers (fifth edition)* (McGraw-Hill Science Engineering publications, 2005)

[12] Francis S Hill, Jr., Stephen M Kelley: *Computer graphics: using OpenGL (third edition)* (Prentice Hall Press publications, 2009)

*Advanced Materials Research Vols. 201-203 (2011) pp 24-29*
*© (2011) Trans Tech Publications, Switzerland*
*doi:10.4028/www.scientific.net/AMR.201-203.24*

# A Novel Symbolic OBDD Algorithm for Generating Mechanical Assembly Sequences Using Decomposition Approach

Zhoubo Xu[1,2,a], Tianlong Gu[2,b], Liang Chang[2,c] and FengYing Li[1,2,d]

[1]School of Electronic Engineering, Xidian University, Xi'an, 710071, China

[2]School of Computer Science and Engineering, Guilin University of Electronic Technology, Guilin 541004, China

[a]xzbli_11@guet.edu.cn, [b] cctlgu@guet.edu.cn, [c]changl@guet.edu.cn, [d]lfy@guet.edu.cn

**Keywords:** Ordered Binary Decision Diagram; Assembly Sequence Planning; Cut-Set; Symbolic Algorithm.

**Abstract.** The compact storage and efficient evaluation of feasible assembly sequences is one crucial concern for assembly sequence planning. The implicitly symbolic ordered binary decision diagram (OBDD) representation and manipulation technique has been a promising way. In this paper, Sharafat's recursive contraction algorithm and cut-set decomposition method are symbolically implemented, and a novel symbolic algorithm for generating mechanical assembly sequences is presented using OBDD formulations of liaison graph and translation function. The algorithm has the following main procedures: choosing any one of vertices in the liaison graph $G$ as seed vertex and scanning all connected subgraphs containing seed vertex by breadth first search; transforming the problem of enumerating all cut-sets in liaison graph into the problem of generating all the partitions: two subsets $V_1$ and $V_2$ of a set of vertices $V$ where both the induced graph of vertices $V_1$ and $V_2$ are connected; checking the geometrical feasibility for each cut-set. Some applicable experiments show that the novel algorithm can generate feasible assembly sequences correctly and completely.

## Introduction

Assembly sequence planning is significant for the design of assembly. It is one of the fundamental research branches of design for product lifecycle. Since 1984, a number of assembly sequence planning systems have been developed; these systems fall into two major categories: those using a direct generation approach and those using disassembly principle. The first approach derives the assembly sequences by putting together separated parts into final assembly; the short coming of this approach is that it may lead to the problem of backtracking when an already assembled part is an obstacle for later assembly operations. The second approach generates the assembly sequences by disassembly principle to decompose the final assembly into separated parts for obtaining the disassembly sequences based on an assumption that the sequence of assembly is the reverse of disassembly sequence, this approach can avoid backtracking. For the most assembly, the assembly sequences can be transformed into the disassembly sequence.

Cut-set decomposition method [1,2] is the most commonly used method for generating disassembly sequence, scanning all cut-sets is the main component of the decomposition method. The traditional algorithms for finding all cut-sets are composed of three steps. First, a spanning tree of the graph is constructed. Second, the fundamental system of cut-sets relative to that spanning tree is found. And third, all the combinations of fundamental cut-sets are computed. The shortcoming of these algorithms is $2^{n-1}$-1 cut-sets (include true cut-set and false cut-set) are generated by them. When the number $n$ is increased, this may lead to the so-called combinatorial explosion.

Homen de Mello and Sanderson presented a more efficient approach to enumerated cut-set [2]. Firstly, all the connected subgraphs having the number of nodes smaller than or equal to a half of the number of nodes in the whole graph is found. For each of these subgraphs, the set of edges of the whole graph that have only one end in the subgraph defines a cut-set if their removal leaves the whole graph with exactly two components. Sharafat and Ma'rouzi proposed a novel algorithm for scaning all minimal cut-sets of a graph based on the breadth-first search method in conjunction with edge contraction [3]. The experimental results showed that their algorithm was much better than traditional algorithms.

Assembly sequence planning is a typical NP-complete problem under assembly process constraint. It is well known that the number of feasible assembly sequences increases exponentially with the number of parts or components composing the whole products. A practicable strategy to combat or ease combinatorial complexity problem to some extent is using implicitly symbolic representation and manipulation technique. Ordered binary decision diagram (OBDD) or variant thereof can realize implicit representation and search of state space or variable combination, which is one of the most efficient symbolic technique. Efficient symbolic algorithms have been devised for hardware verification, model checking, testing and optimization of circuit [4,5]. Hachtel and Somenzi developed the OBDD-based symbolic algorithm for maximum flow in 0-1 networks that can be applied to very large graph (more than $10^{36}$ edges) [6]. Recently, there has emerged a class of OBDD-based approaches in mechanical assembly sequence planning. Gu, Xu and Yang proposed symbolic OBDD representations for mechanical assembly sequences[7], the experimental results show that the storage space of OBDD based representation of all the feasible assembly sequences is less than that of AND/OR graph do. Gu and Liu developed an algorithmic procedure using a direct generation approach to generate all feasible assembly sequences by putting together the separated parts into final assembly from the OBDD of liaison graph and translation relation [8], but this procedure leads to the problem of backtracking when an already assembled part is an obstacle for later assembly operations. Xu and Gu presented a novel scheme to integrate constraint satisfaction problem model with the symbolic ordered binary decision diagram for the assembly sequence planning [9], but this procedure also leads to the problem of backtracking.

In this regard, this paper presents a symbolic OBDD algorithm for assembly sequence based on symbolic OBDD assembly model of liaison graph and translation function, the algorithm is developed by integrating the idea of Sharafat's recursive contraction algorithm with cut-set decomposition method, and generates disassembly sequences by decomposing final assembly into separated parts. In this algorithm, assembly sequences are represented by AND/OR graph, the nodes in the AND/OR graph correspond to subassemblies which are represented by OBDD, and the hyperarcs correspond to assembly tasks in which two subassemblies are joined to yield a larger more complex subassembly. The experiment results show that the algorithm can generate geometrically feasible assembly sequences completely and correctly.

## Symbolic formulation of assembly knowledge

**Symbolic OBDD representation of liaison graph.** Liaison graph is one of the role model for generating assembly sequences. Liaison graph is a undirected connected graph $G=<V,E>$, where $V$ is a set of vertices which corresponding to the parts in the assembly, $E$ is a set of edges, in which one edge for each pair of parts that have at least one contact.

Given an assembly and its liaison graph $G=<V,E>$, we can convert the liaison graph to an OBDD by encoding the parts of the assembly or the elements in $V$ with a length-$n$ binary number, where $n=\lceil \log_2|V| \rceil$. Each encoded node in $V$ corresponds to a vector of binary variables $X=(x_0,x_1,\ldots,x_{n-1})$. For any edge $(u,v)\in E$ can be represented by binary vector $(X,Y)=(x_0,x_1,\ldots,x_{n-1},y_0,y_1,\ldots,y_{n-1})$, where $X=(x_0,x_1,\ldots, x_{n-1})$ and $Y=(y_0,y_1,\ldots,y_{n-1})$ are the binary encodings of node $u$ and node $v$, respectively. For example, we use an simple assembly shown in Fig.1a, this assembly includes 6 parts, and its liaison graph is presented in Fig.1b. So we need only length-3 binary number to encoding the parts in the assembly. Let part 1, 2, 3, 4, 5 and 6 correspond to binary number 001, 010, 011, 100, 101 and 110 respectively, the characteristic function of $E$ is derived as following:

$$\Phi_C(x_0,x_1,y_0,y_1)=x_0'x_1'x_2y_0'y_1y_2'+x_0'x_1'x_2y_0y_1'y_2'+x_0'x_1'x_2y_0y_1'y_2+x_0'x_1x_2'y_0y_1'y_2+x_0x_1'x_2'y_0y_1'y_2+ \\ x_0'x_1x_2y_0y_1'y_2'+x_0'x_1x_2y_0y_1'y_2+x_0'x_1x_2y_0y_1y_2'+x_0x_1'x_2y_0y_1y_2'$$

The OBDD for this characteristic function is shown in Fig.1c.

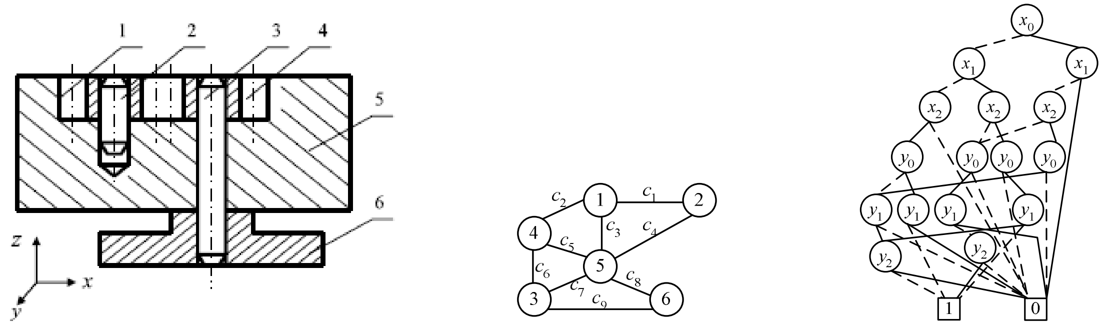

(a) A assembly (b) Liaison graph G (c) OBDD for Liaison graph

Fig.1 An simple assembly

**Symbolic OBDD representation of translation function**. The liaison graph provides only the necessary conditions but not sufficient to assembly two components. To be a feasible assembly operation, it is necessary that there is a collision-free path to assembly parts. Gottipolu and Ghosh defined contact and translational functions to represent the connectivity and the relative motion between parts of the assembly [10]. In fact, contact function can derive from liaison graph and translational function directly. In this regard, we use liaison graph and translational function as assembly model.

Translational function $T$: $P\times P\rightarrow\{0,1\}^6$, where $P$ is a set of parts, $\{0,1\}^6$ is a 0-1 vector space with six dimension, each dimension correspond to the one of six directions of triorthogonal Cartesian coordinate system. Here, directions 1, 2, 3, 4, 5 and 6 indicate the six directions +X, +Y, +Z, –X, –Y, and –Z of X, Y and Z axes respectively.

Let $(a, b)\in P\times P$, the correspond value of $T$ function is 0-1 vector space with six dimension ($T_1(a,b)$, $T_2(a,b)$, $T_3(a,b)$, $T_4(a,b)$, $T_5(a,b)$, $T_6(a,b)$), where $T_i(a,b)=1$ ($i=1,2,\dots,6$) if the part $b$ has the freedom of translational motion with respect to the part $a$ in the direction $i$, $T_i(a,b)=0$ if the part $b$ has no freedom of translational motion with respect to the part $a$ in the direction $i$.

For example, Table 1 shows the translational function $T$ for the assembly shown in Fig.1a.

According to the encoding method introduced in the above section, the $i$th component of translational function $T$ can be represented by the following characteristic function:

$$\Phi_{T_i}(x_0, x_1, \ldots, x_{l-1}, y_0, y_1, \ldots, y_{l-1}) = \begin{cases} 1, & if \quad T_i(a,b) = 1 \\ 0, & otherwise \end{cases} . \tag{1}$$

So, for the assembly shown in Fig.1, the shared binary decision diagram (SBDD) [11] for translation function is shown in Fig.2. For clearly, the edge point to sink node 0 is omitted in SBDD shown in Fig.2.

Table1 $T$ function for the assembly shown in Fig.1

| Pair | $T_1$ | $T_2$ | $T_3$ | $T_4$ | $T_5$ | $T_6$ | Pair | $T_1$ | $T_2$ | $T_3$ | $T_4$ | $T_5$ | $T_6$ | Pair | $T_1$ | $T_2$ | $T_3$ | $T_4$ | $T_5$ | $T_6$ |
|---|---|---|---|---|---|---|---|---|---|---|---|---|---|---|---|---|---|---|---|---|
| (1,2) | 0 | 0 | 1 | 0 | 0 | 1 | (3,1) | 0 | 1 | 1 | 1 | 1 | 1 | (5,1) | 0 | 0 | 1 | 0 | 0 | 0 |
| (1,3) | 1 | 1 | 1 | 0 | 1 | 1 | (3,2) | 0 | 1 | 1 | 1 | 1 | 1 | (5,2) | 0 | 0 | 1 | 0 | 0 | 0 |
| (1,4) | 1 | 0 | 1 | 0 | 0 | 1 | (3,4) | 0 | 0 | 1 | 0 | 0 | 1 | (5,3) | 0 | 0 | 1 | 0 | 0 | 1 |
| (1,5) | 0 | 0 | 0 | 0 | 0 | 1 | (3,5) | 0 | 0 | 1 | 0 | 0 | 1 | (5,4) | 0 | 0 | 1 | 0 | 0 | 0 |
| (1,6) | 1 | 1 | 0 | 1 | 1 | 1 | (3,6) | 0 | 0 | 1 | 0 | 0 | 1 | (5,6) | 1 | 1 | 0 | 1 | 1 | 1 |
| (2,1) | 0 | 0 | 1 | 0 | 0 | 1 | (4,1) | 0 | 0 | 1 | 1 | 0 | 1 | (6,1) | 1 | 1 | 1 | 1 | 1 | 0 |
| (2,3) | 1 | 1 | 1 | 0 | 1 | 1 | (4,2) | 0 | 1 | 1 | 1 | 1 | 1 | (6,2) | 1 | 1 | 1 | 1 | 1 | 0 |
| (2,4) | 1 | 1 | 1 | 0 | 1 | 1 | (4,3) | 0 | 0 | 1 | 0 | 0 | 1 | (6,3) | 0 | 0 | 1 | 0 | 1 | 1 |
| (2,5) | 0 | 0 | 0 | 0 | 0 | 1 | (4,5) | 0 | 0 | 0 | 0 | 0 | 1 | (6,4) | 1 | 1 | 1 | 1 | 1 | 0 |
| (2,6) | 1 | 1 | 0 | 1 | 1 | 1 | (4,6) | 1 | 1 | 0 | 1 | 1 | 1 | (6,5) | 1 | 1 | 1 | 1 | 1 | 0 |

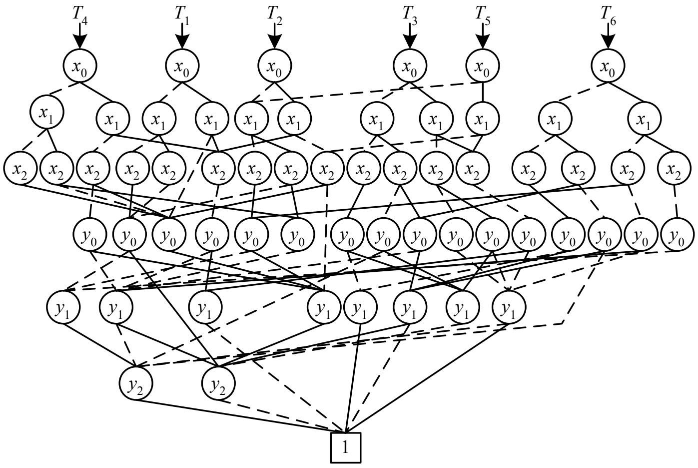

Fig.2 SBDD for translation function

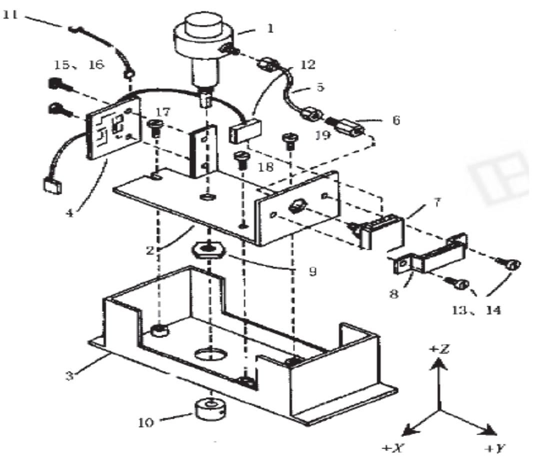

Fig.4 An electrical controller

**The algorithm for generating all assembly sequences**

Based on an assumption that the sequence of assembly is the reverse of that of disassembly, we applying the assembly by disassembly principle to decompose the final assembly into separated parts for obtaining the disassembly sequences. The decompositions are enumerated by enumerating the cut-sets of the assembly's liaison graph, and each cutest corresponds to a decomposition. For two disjoint sets $V_1$ and $V_2$ of vertices in a graph $G=<V, E>$, a graph consisting of vertex set $V_1$ and edge set $E_1=\{<v,w>\in E|v,w\in V_1\}$ is designated as a induced subgraph for vertex set $V_1$ of $G$ and is denoted by $G[V_1]=<V_1, E_1>$. As is well known, a necessary and sufficient condition for a cut $\omega=\{<v,w>\in E|v\in V_1, w\in V_2\}$ to be an cut-set in graph $G$ is that the induced subgraphs $G[V_1]$ and $G[V_2]$ of $G$ are both connected, Thus the problem of enumerating all the cut sets in $G$ is reduced to that of generating all the partitions of $V$ into two subsets $V_1$ and $V_2$ such that $V_1\cup V_2=V$, $V_1\cap V_2=\varnothing$, and both $G[V_1]$ and $G[V_2]$ are connected.

The algorithm for generating all assembly sequences is shown in Fig.3, which takes the OBDDs of the assembly's liaison graph $C(x,y)$, translation function $T(x,y)$, a set of parts of the assembly $PSet(x)$ as input. In the procedure, assembly sequences are represented by AND/OR graph, the nodes in the AND/OR graph correspond to subassemblies which are represented by OBDD, and the hyperarcs correspond to assembly tasks in which two subassemblies are joined to yield a larger more complex subassembly.

```
GAAS($C(x,y)$, $T(x,y)$, $PSet(x)$) {
  $open=PSet(x)$;
  $closed=\varnothing$;
  while ($open$ is not empty) {
    $V_1(x)$=Pop($open$);
    Push($closed$, $V_1(x)$);
    $L(x,y)$= Generate_Vertex_Induced_Subgraph(
          $V_1(x)$,$C(x,y)$);
    $seed(x)$=Pick_One_Minterm($V_1(x)$);
    $clist$=Find_Connected_Subgraphs_Include_Seed
          ($seed(x)$,$L(x,y)$);
    while($clist$ is not empty) {
      $s_1(x)$=Pop($clist$);
      $s_2(x)$= $V_1(x)$-$s_1(x)$;
      $G_2(x,y)$=Generate_Vertex_Induced_Subgraph
          ($s_2(x)$,$L(x,y)$);
      $CFlag$=Check_Connection($G_2(x,y)$);
      if($CFlag$) {
        $GFlag$=Check_Geometrical_Feasible(
              $s_1(x)$,$s_2(x)$,$T(x,y)$);
        if($Gflag$) {
          Insert_Assemble_Task($s_1(x)$,$s_2(x)$,$V_1(x)$,
                $and\_or\_graph$);
          Insert_Subassembly($s_1(x)$,$s_2(x)$,$open$,
                $closed$);
        }
      }
    }
  }
  return($and\_or\_graph$);
}
```

Fig.3 Pesudo-code for generating all assembly sequence

Procedure GAAS uses the lists *closed* and *open* to store the pointers to OBDD of the subassembly whose decompositions into smaller subassemblies, respectively, have and have not been generated. The procedure takes one subassembly from *open* at a time, moves it to *closed*, and calls procedure Generate_Vertex_Induced_Subgraph() in line 6 to generate the induced subgraph of vertex set which corresponding to the set of parts in subassembly. Given graph $C(x,y)$ and vertex set $V_1(x)$, the induced subgraph $L(x,y)$ of vertex set $V_1(x)$ is computed as follows:

$$L(x,y)=V_1(x) \wedge C(x,y) \wedge V_1(y). \tag{2}$$

After that, procedure Pick_One_Minterm() in line 7 is called to pick one minterm from the OBDD $V_1(x)$, and then the procedure Find_Connected_Subgraphs_Include_Seed() in line 8 is called to find all connected subgraphs which include vertex $seed(x)$ in the subgraph $L(x,y)$, and all connected subgraphs's vertex sets are stored in the list *clist*. In the procedure, subgraph $L(x,y)+L(y,x)$ is visited in a breadth-first search (BFS) manner which starts from the seed vertex $seed(x)$, the vertices reached for the first time and not in $seed(x)$ is store in BDD $t(x)$. For each minterm $m(x)$ of $t(x)$, let $r(x)=seed(x)+m(x)$, so the induced subgraph for $r(x)$ is a connected graph, vertices $r(x)$ is inserted into connected subgraph list *clist*. After that, let $r(x)$ is a seed vertex, and repeats the above method until BFS is performed $n$-1 times ($n$ is the number of parts in the assembly).Thus, we get all connected subgraphs with 1,2,3,…,$n$-1 vertices (there may be no such subgraph with $i$ vertices, $2 \le i \le n-1$) respectively, and all of these include vertices $seed(x)$.

For the liaison graph shown in Fig.1b, we suppose initial value of the $seed(x)$ is 1 (for convenience, we use part's number to represent its OBDD), all connected subgraphs with $seed(x)$ are found as follows: Starting from *seed*, the liaison graph is traversed in a BFS manner, we will get the set of vertices $t$={2,4,5} reachable from the *seed* in 1 step, thus all the connected graphs with 2 vertices which include *seed* are found, namely the induced subgraph of vertex set {1,2}, {1,4} and {1,5} are connected graphs. After that, we set the above vertex sets to *seed* one by one, suppose we first set *seed*={1,2}, then starting from {1,2}, the liaison graph is traversed in a BFS manner, we will get the set of vertices $t$ reachable from the {1,2} in 1 step, where $t$={4,5} in which the vertices in *seed* is already removed. Thus we will get all the connected graphs with 3 vertices which include *seed* {1,2}, namely the induced connected graph of vertices{1,2,4} and {1,2,5}. For the same reason, when we choose *seed*={1,4}, we will get the induced connected graph of vertices {1,4,5} and {1,3,4}, and so on, at last we get all connected subgraphs of liaison graph which induced by vertices {1}, {1,2}, {1,4}, {1,5}, {1,2,4}, {1,2,5}, {1,4,5}, {1,3,4}, {1,3,5}, {1,5,6}, {1,2,4,5}, {1,2,3,4}, {1,2,3,5}, {1,2,5,6}, {1,3,4,5},{1,4,5,6}, {1,3,4,6},{1,3,5,6}, {1,2,3,4,5}, {1,2,4,5,6}, {1,2,3,4,6}, {1,2,3,5,6} and {1,3,4,5,6}, and all of these are inserted into *clist*.

For each vertices set in *clist*, it need to check the feasibility of decompositions, which include two step, one step is check connectivity, the other step is check geometrical feasibility. If the decomposition is feasible, then insert the assembly task into AND/OR graph *and_or_graph*, and if the subassembly is not in the list *open* or *closed*, then put subassembly on the list *open*.

For example, for induced connected subgraph of vertices {1}, compute another subgraph with vertices {1,2,3,4,5,6}-{1}={2,3,4,5,6}, and then check whether or not the decomposition of {1,2,3,4,5,6} into {1} and {2,3,4,5,6} is feasible. Firstly, procedure Check_Connection () in line 13 is used to check the connectivity of the induced graph of {2,3,4,5,6}. If the result is connected then return *true*, else return *false*. Because the procedure returns true, the induced graph of {2,3,4,5,6} is a connected graph. The decomposition of an assembly into $s_1(x)$={1} and $s_2(x)$={2,3,4,5,6} is corresponding to a cut-set of liaison graph. Secondly, the procedure Check_Geometrical_Feasible() in line 15 is used to check geometrical feasibility for subassembly $s_1(x)$ and subassembly $s_2(x)$. If subassemblies $s_1(x)$ and $s_2(x)$ are geometrically feasible, insert the assembly task into AND/OR graph *and_or_graph*, i.e., {1} and {2,3,4,5,6} are geometrically feasible. If the geometrically feasible subassembly is not in the list *open* or *closed*, insert subassembly into *open*, so subassemblies {1} and {2,3,4,5,6} are both inserted into *open*.

## Experiments

The symbolic algorithms proposed in this paper have been implemented in windows XP and the software package CUDD [12]. Geometrically feasible assembly sequences of some applicable assemblies, such as assembly shown in Fig.1 and electrical controller (Fig.4), were generated by the prototype tool GAAS using Microsoft Visual C++. In both cases, GAAS are run on a P4 3GHz with 512MB of memory. For the assembly shown in Fig.1, the AND/OR graph for that product contains 44 nodes and 133 hyperarcs, and the CPU time is 0.031 seconds for generating all assembly sequences. In electrical controller case, the AND/OR graph for the product contains 1530 nodes and 9659 hyperarcs, and the CPU time is 871.359 seconds for generating all assembly sequences.

## Conclusions

A symbolic OBDD algorithm for generating mechanical assembly sequence is presented based on Sharafat's recursive contraction algorithm and cut-set decomposition method. The geometrically feasible assembly sequences are verified and generated symbolically and implicitly using efficient OBDD structures and manipulations. Some applicable experiments show that the novel algorithm can generate feasible assembly sequences correctly and completely.

## Acknowledgments

This work has been supported by National Natural Science Foundation of China (60963010, 60903079, 61063002) and Key Natural Science Foundation of Guangxi Province (0832006Z).

## References

[1] D.F. Baldwin, T.E. Abell, M.M.Lui, et al.: IEEE transactions on Robotics and Automation. Vol. 7(1991), p.78

[2] L.S. Homen de Mello, A.C.Sanderson: IEEE Transaction on Robotics and Automation. Vol. 7(1991), p.228

[3] A.R. Sharafat, O.R. Ma'rouzi: A novel and efficient algorithm for scanning all minimal cutsets of a graph. ArXiv preprint math. CO/0211436 (2002).

[4] R. Drechsler, D. Sieling: International Journal on Software Tools for Technology Transfer. Vol. 3(2001), p. 112

[5] R.E. Bryant: ACM Computing Surveys.Vol. 24(1992), p. 293

[6] G.D. Hachtel, F.Somenzi: Formal Methods in System Design. Vol. 10(1997), p.207

[7] T.Gu, Z. Xu , Z.Yang: Computer-Aided Design, Vol. 40(2008), p.411

[8] T.Gu, H.Liu: Formal Methods in System Design, Vol. 33(2008), p.29

[9] Z.Xu, T.Gu: Journal of Computer-Aided Design & Computer Graphics, Vol. 22(2010), p.803(In Chinese)

[10] R.B. Gottipolu, K. Ghosh: Computers in Industry. Vol. 50(2003), p.251

[11] S. Minato, N.Ishiua, S. Yajima: Proceedings of the 27th ACM/IEEE Design Automation Conference, New York, 1990, p.52

[12] F. Somenzi. CUDD:CU Decision Diagram Package Release 2.3.1. http://vlsi.Colorado.edu/.

*Advanced Materials Research Vols. 201-203 (2011) pp 30-35*
*© (2011) Trans Tech Publications, Switzerland*
*doi:10.4028/www.scientific.net/AMR.201-203.30*

# The Analysis of the Temperature Field and Deformation of Cylinder Liner Base on Finite Element Method and Experiment

Kun Li[a], Tiexiong Su[b], Xiaojie Li , Shixin Xing

School of Mechanical and Electronic Engineering, North University of China, Taiyuan 030051 China

[a] fendou1981@tom.com, [b] @nuc. .

**Keywords:** ; mp F ; D mation; F m ; Exp m

**Abstract.** The distortion of the cylinder liners of internal combustion engines has a significant affect on engine operation. It can affect the oil consumption, the blow-by, the wear behavior and, due to friction, the fuel consumption. In order to achieve future requirements regarding exhaust emissions and fuel consumption, the development of low distortion engine blocks will play a significant role. Finite element method with experimental data were used to calculate and analysis the temperature field and machine assembly of a 150 engine cylinder liner in this paper. It can provide a theoretical basis for the controlling of the cylinder liner deformation.

## Introduction

The internal combustion engine combustion chamber is formed by the cylinder head, piston, cylinder liner and piston rings. Modern passenger car engines are designed to operate increasingly higher rated engine speeds with higher thermal loads. To reduce engine weight and length, the heat load of the engine will become more and more baptismally. This leads to high temperatures in the siamesed area and to an increase in liner deformation. The deformation of the cylinder liner could damage the piston rings seal, and further affects the engine's economy, power and emissions characteristics [1-2]. To reduce the cylinder liner deformation can reduced radial clearance between piston and cylinder bore. This can reduce the impact of the piston to the cylinder liner and reduce the vibration and noise of the engine. The method of cylinder deformation measurement be combined with the FEM calculations for the crankcase is an effective and cost-reducing tool.

## Three-Dimensional solid model and Fem-Calculations model

The finite element calculation method is based on the three-dimensional solid models. The three-dimensional solid models are concluded by the bearing caps, crankshaft, main bearings, cylinder head, cylinder liner, cylinder head gasket, cylinder head bolts, bearing cap bolts and so on. The three-dimensional solid models are shown as figue1and figue2. The Combined model is shown as figure3. The component materials are shown as Table 1.

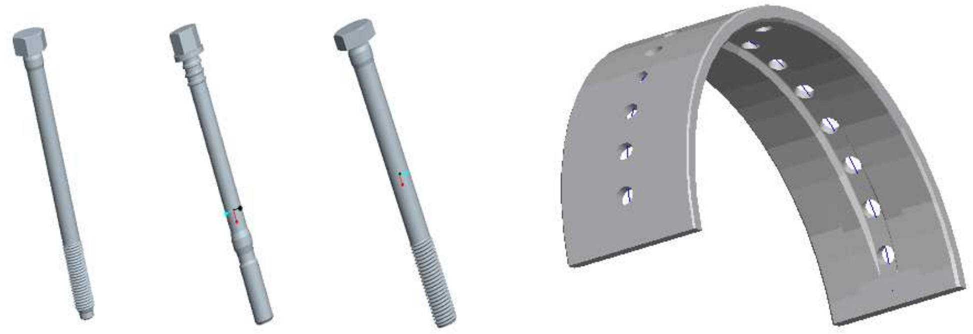

Figure1. The cylinder head bolts model and Main bearing model

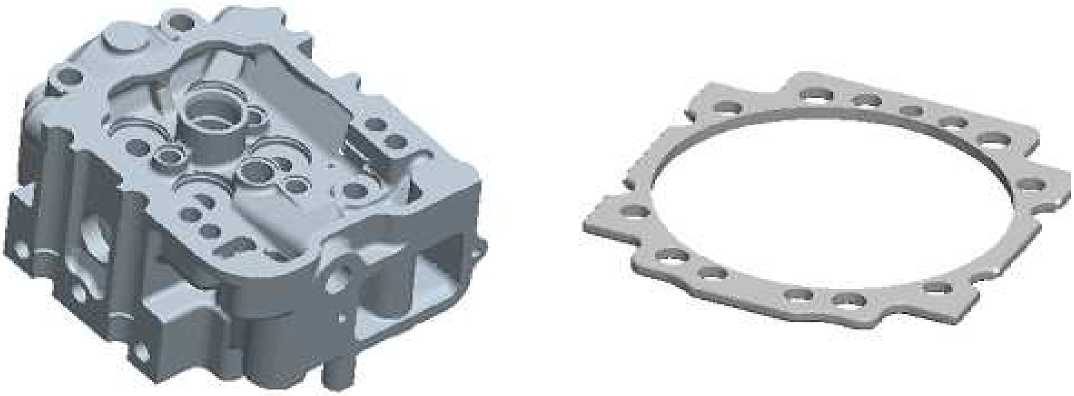

Figure2. The cylinder Head model and cylinder head gasket model

## The finite element analysis boundary conditions

It is important to provide accurate boundary conditions for a bore distortion calculation. Some simplifications are made to reduce the calculation time.

2.1 The displacement boundary conditions

The rigid body displacement constraints; body, cylinder, cylinder head, crankshaft, cylinder gasket, main bearing caps the cut surface of symmetry displacement constraints.

2.2 The contact boundary conditions

The model established the contact boundary conditions between the cylinder head and cylinder gasket, cylinder and cylinder gasket, cylinder liner and the body, the body with the main bearing caps, crank and block, crankshaft and main bearing caps and bolts and the body, cylinder head and main bearing caps.

2.3 The force boundary conditions

The loads acting on the liner come from a variety of conditions, for example: Assembly of the cylinder head and cylinder head gasket (assembly loads); Thermal expansion variations between the cylinder block and cylinder head; Gas pressure during fired operation Temperature gradients during fired operation. All of them are stated as Table 2 and Table 3.

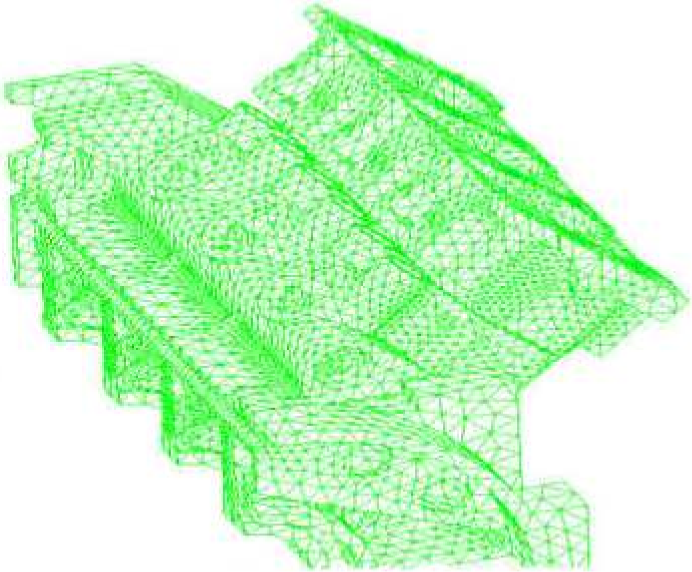

Figure 3. The combined finite element model of half-body

Table1. The material of the solid models

| The part | The material |
|---|---|
| Engine block | QT500-7 |
| Main bearing cap | 42CrMo |
| Bolts | 42CrMo |
| Cylinder liner | Cr-Mo cast iron copper |
| Rubber sealing ring | Viton |
| Cylinder head | Special cast iron |
| Cylinder head gasket | ZL301 |

Table 2 The size of the bolt preload (unit: N)

| | |
|---|---|
| The preload of the inside main bearing cap bolt | 63269N |
| The preload of the outside main bearing cap bolt | 44815N |
| Cylinder head bolt tightening force | 134464N |

Table 3 The forces of the left second cylinder when the engine outbreak (unit: N)

| | The first cylinder | The second cylinder | The third cylinder |
|---|---|---|---|
| Gas pressure | 2424 | 2.223e5 | 207.8 |
| Connecting rod force | 19671.8 | 186078.2 | 20417.2 |
| Connecting rod force | -4863.8 | 6905.9 | 4290.4 |

**The calculation of the cylinder temperature distribution**

The temperature distribution along the height of the cylinder liner has regular. It is shown as formula 1 and formula 2.

$$\alpha_m(h)=\alpha_m(0)\cdot(1+k_1\beta)\cdot e^{-\sqrt[3]{\beta}};\ T_{res}(h)=T_{res}(0)\cdot(1+k_2\beta)\cdot e^{-\sqrt{\beta}} \qquad (1)$$

Which: $\beta=h/s(0\le\beta\le1)$; $k_1=0.573(S/D)^{0.24}$; $k_2=1.45k_1$ (2)

where is the average heat transfer coefficient of gas working cycle, is the average temperature of the gas work cycle ,β is the ratio of the axial position h to the stroke S, k1is the average temperature of gas equivalent,k2 is the average heat transfer coefficient of gas equivalent.

All of the significant aspects of thermal heat flux and material behavior must be considered. The flux from the piston and gas to the liner–a combustion simulation program, that is based on the Woschni equations shown as formula 1 and formula 2, calculates the piston thermal load. The average gas temperatures shown as Figure4, and the heat transfer coefficients (HTC) from the gas to the liner as a function of cylinder height shown as Figure 5 [3-4]. These boundary conditions are applied to the gas side. The input data to the combustion simulation program are improved by the experience from measured and calculated temperatures. The assumed wall temperatures have a great influence on the resulting thermal heat flow. An iterative procedure is necessary. The temperature nephogram of the cylinder liner by simulating is shown as Figure6.The temperature distribution along the wall of the cylinder as shown as Figure7.

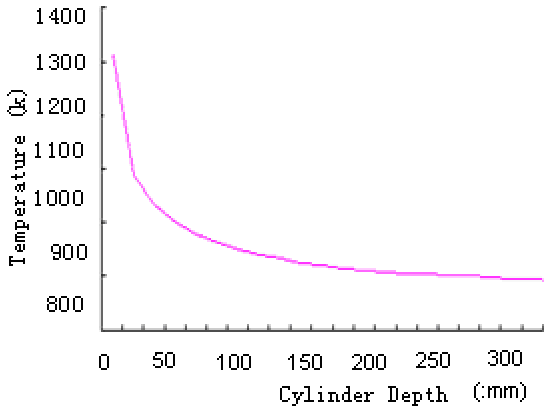

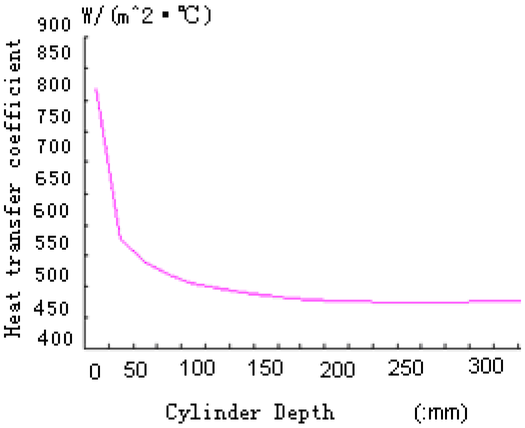

Figure 4. The average temperature of the gas along the cylinder height. Figure 5. The average heat transfer coefficient along the cylinder height .

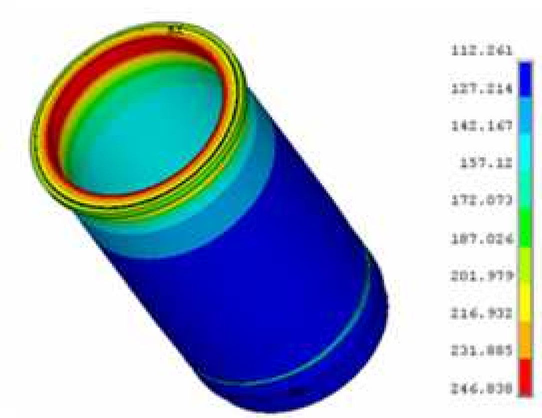

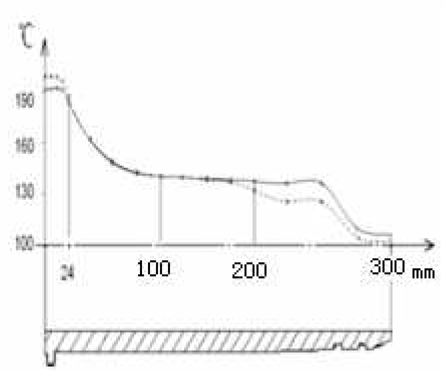

Figure 6.The temperature cloud of the cylinder liner . Figure 7.The temperature distribution along the wall of the cylinder .

## The calculation and analysis of the cylinder deformation under thermo-mechanical coupling

The deformations of the engine body and cylinder liner under Thermo-mechanical coupling are calculated by finite element methods. Based on the Large-scale commercial software ANSYS .Take the temperature filed Calculated by the 3 as the boundary conditions in the computing environment. Set the relevant boundary conditions, such as 2.1-2.3 above. The deformation and stress of the engine body and cylinder liner are shown as Figure 8- Figure 11.

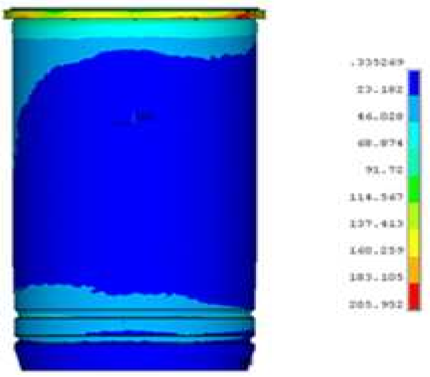

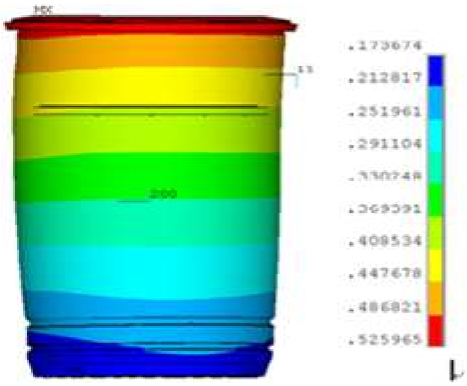

Figure 8.The equivalent stress contour of cylinder. Figure 9.The overall deformation cloud of cylinder

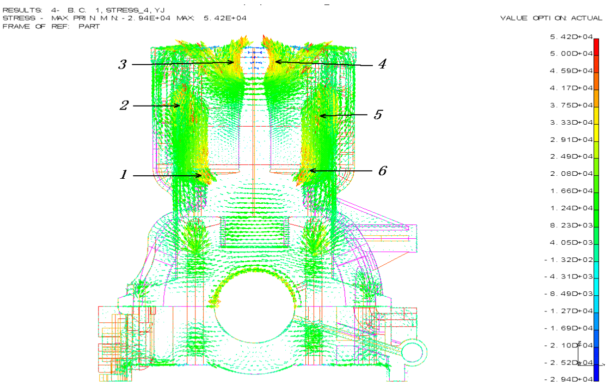

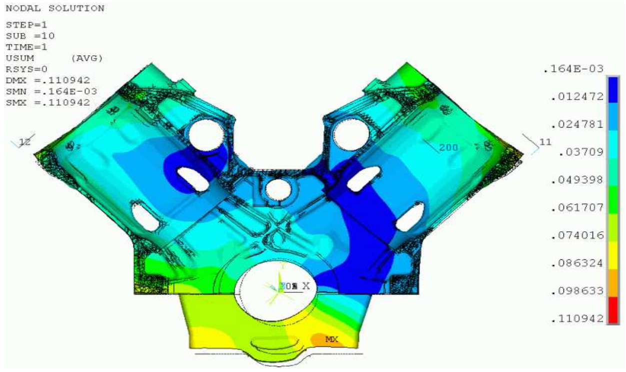

Figure10. The maximum principal stress under thermo-mechanical coupling. Figure11.The deformation of the engine body under thermo-mechanical coupling.

## Experiments arrangement and the results compared

The validation of Finite Element Analysis results by measurement is important with respect to the reliability of predictive thermo-mechanical analysis; therefore, verifications are indispensable. In the following text, the measurements are carried out on a 12V150 diesel engine. Strain gauges are attached to the corresponding position of the cylinder and the engine body. The strain gauges can measure the deformation, when the engine cold-static, tensioned. The measurement of the liner geometry is performed after assembling the cylinder head and the cylinder head gasket. This gives reference to the tension after engine assembly and enables one to evaluate the influence of the bolt forces on the liner distortion. They also can measure the deformation when the engine fired. The cylinder contour will be scanned, corresponding to the stroke movement of the piston. This requires the installation of up to 8 eddy current sensors in the production piston of the engine. The arranged of the strain gauges as shown in Figure12.

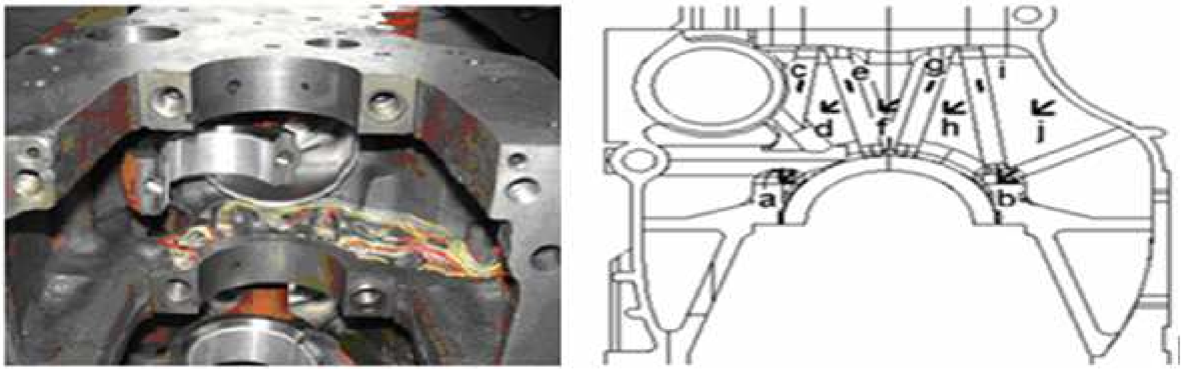

Figure12. The arrangement of the strain gauges

The method presented here for measuring cylinder deformation in operational fired engines represents a suitable tool for adapting the tribological system piston/piston ring/cylinder liner to future requirements [5]. These measurements are also of significant value in calibrating analytical models, enhancing the accuracy and reliability of subsequent analysis. The comparison of the Measurement results and FEA results are shown in Figure 13and Figure 14.

The FEA results and experimental results show good agreement. In other words, the finite element model and boundary condition settings are correct. The trend that the results of the cylinder liner deformation performance are reliable. Analysis conclusion based on the results obtained by the finite element method is credible.

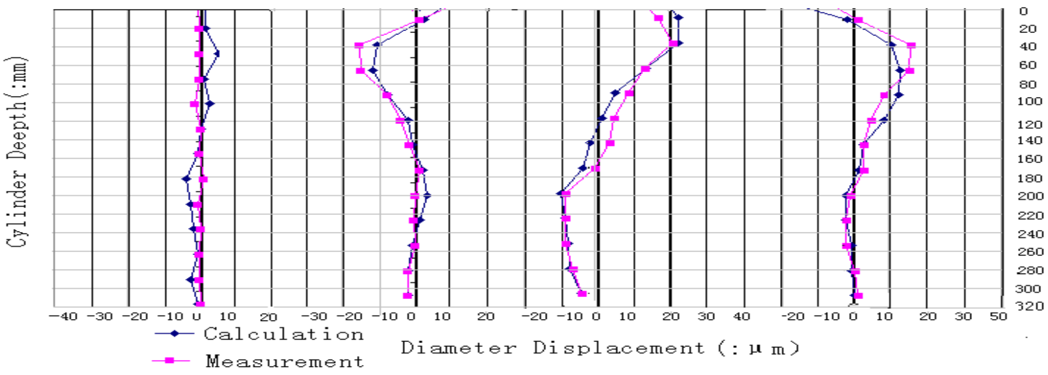

Figure13. Calculated and Measured Bore Distortion, Cold Assembly

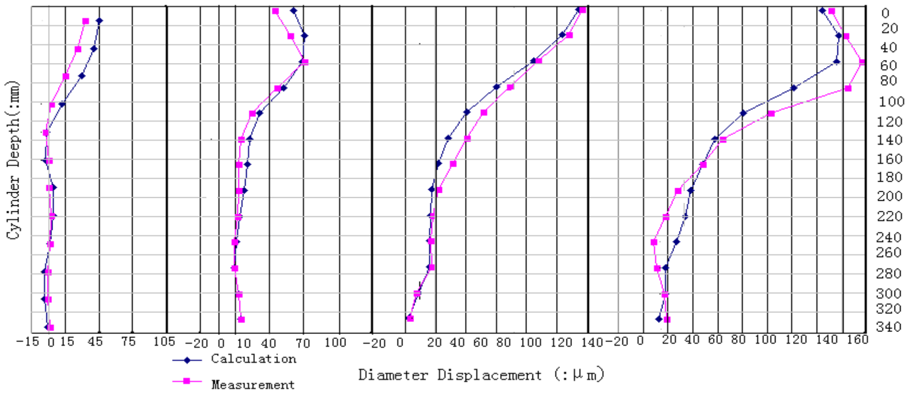

Figure14. Calculated and Measured Bore Distortion, Loads at 5000 rpm, WOT

## Conclusions

1. Cylinder temperature decreased gradually from top to bottom, the maximum temperature of 200 ℃, the internal wall temperature is higher than outside. Heat transfer coefficient has important implications on the cylinder temperature distribution.

2. Cold-static, and after assembling the cylinder head and the cylinder head gasket. The bolt forces depth has some influence on the deformation of the cylinder linger.

3. Cylinder radial deformation increases, the coupling effect in the heat, when the engine fired under thermo-mechanical coupling. The deformation of the piston thrust side significantly higher than the other side.

4. Control the deformation of the engine block can reduce the deformation of the cylinder liner.

## References

[1] Grogeneweg M.A. Current Application of Finite Element Analysis to Diesel Engine Component Design [J].SAE Paper 870813.

[2] Gilson A.Vicentini, Jan Vatavuk. Study of Sea Transportation Effects on Corrosion of Cast Iron Cylinder Liners [J].SAE Paper 2001-01-3978.

[3] Pranz Koch, Poul Decker. Cylinder Liner Deformation Analysis-measurements And Calculation [J] .SAE Paper 980567.

[4] J.Abraham, D.R Amoth,J.Mannisto.3D Steady-State Wall Heat Fluxes and Thermal Analysis of a Stratified-Charge Rotary Engine [J].SAE Paper 910706.

[5] Yang Shiwen , Zhang Yi , Su Tiexiong , et al. Distortion analysis and structural parameters optimization of cylinder liner of heavy duty diesel engines[J] . Chinese Internal Combustion Engine Engineering, 2003, 24 (2) : 252 29. (in Chinese).

*Advanced Materials Research Vols. 201-203 (2011) pp 36-39*
*© (2011) Trans Tech Publications, Switzerland*
*doi:10.4028/www.scientific.net/AMR.201-203.36*

# Problems in the Application of Commercial CAD/CAE Software and Improvement Methods

Cheng Wang [a], Xiongwei Yang [b] and Baokun Yang [c]

Key Laboratory for Strength and Vibration of Mechanical Structures, Xi'an Jiaotong University, Xi'an 710049 China

[a]wc071@163.com, [b] xiongwei@stu.xjtu.edu.cn, [c]yang.bk@stu.xjtu.edu.cn

**Keywords:** CAD/CAE; Commercial Software; Problems; Software engineer; Improvement Methods.

**Abstract.** CAD / CAE technology has led traditional product design and analysis to digital. However, commercial CAD / CAE software also has its problems. Problems in the application of commercial CAD / CAE software are summarized in these this paper. From perspective development of software engineer, new technology such as integrated design, design reuse, intelligence and automation, workflow customization, application development, experimental and simulation complement each other are introduced to overcome these problems in this paper.

## Introduction

With the development and application of computer, CAD / CAE technology has led a revolution in product design and analysis. Traditional design–prototype performance testing- manufacturing techniques process is difficult to adapt modern production requirements. Using computer systems, CAD / CAE technology provides a reliable guarantee for enterprise to improve product design capabilities, shorten product research and development cycles, and improve product performance. It is an integrated environment oriented to product design, analysis and management, and also a new measure to reconstruct traditional industry and improve technological innovation as well as technical strength. From global R&D, simulation accounts for a significant large proportion and plays a more and more important role. Design and analysis of a great number of foreign companies rely on simulation. For example, Boeing has realized the digital design of Boeing aircraft.

From the perspective of CAD / CAE users, many problems exist in the application of commercial CAD/CAE software for digital design at present. Problems in the application of commercial CAD / CAE software are summarized in these this paper.

From perspective development of software engineer, new technology such as integrated design[1], design reuse[2], intelligence and automation[3], workflow customization, application development [4], experimental and simulation complement each other are introduced to overcome these problems in the application of commercial CAD / CAE software in this paper.

## Problems in the Application of CAD/CAE Commercial Software

**Difficulties of Information Transmission among Software.** The process of CAD / CAE is divided into several steps, and each different step uses different commercial software. In order to achieve efficient and fast access, most commercial software adopt private and incompatible binary file format to achieve efficient and fast access, which results in information transmission difficulty among different software. However, the same model needs to be modified in the application of different software, which brings forward heavy workload and is highly fallible.

**Difficulties in Guarantee Accuracy of Simulation Results Page.** The core principles and algorithm of commercial software are trade secrets, and are not open to the public. The accuracy of simulation results depend on familiarity with software kernel. At the same time, in pursuit of general-utility, a lot of parameters need to be set in commercial software, but any parameter setting mistake may greatly affect the simulation results, which is a too high starting point for an engineer who has rare experience.

**Difficulties in Fulfilling the Individuation Requirements of Enterprises.** Commercial CAD/CAE Software pursues general-utility, while the actual situations of each enterprise and application requirements vary. It is very difficult to establish a unified platform to meet the application under various conditions. And the situations that commercial software does not meet demand of the enterprise frequently emerge. Because of the limitations of algorithm adopted by commercial software, there exists computing capability and suitable application bound limit in dealing with engineering practice issues; It is also very difficult to debug when error emerge. The situation of commercial software does not meet the enterprise demand must Emerge.

## Improvement Methods

**Integrated Design.** CAD/CAE integrated design can realize the share of information and model, maintain the unity of data and improve the efficiency of information transformation. A CAD / CAE integrated software platform with unified file format standard and use style, groupware and modular design and sales mode, user-friendly, will be suitable for the working habits of the technical personnel. And it will also reduce the time to learn and get familiar with machinery construction and minimize the difficulty in training. The framework of CAD / CAE integrated software platform is shown as in Figure 1.

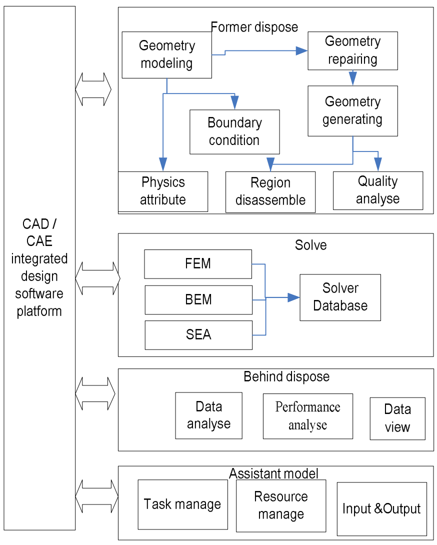

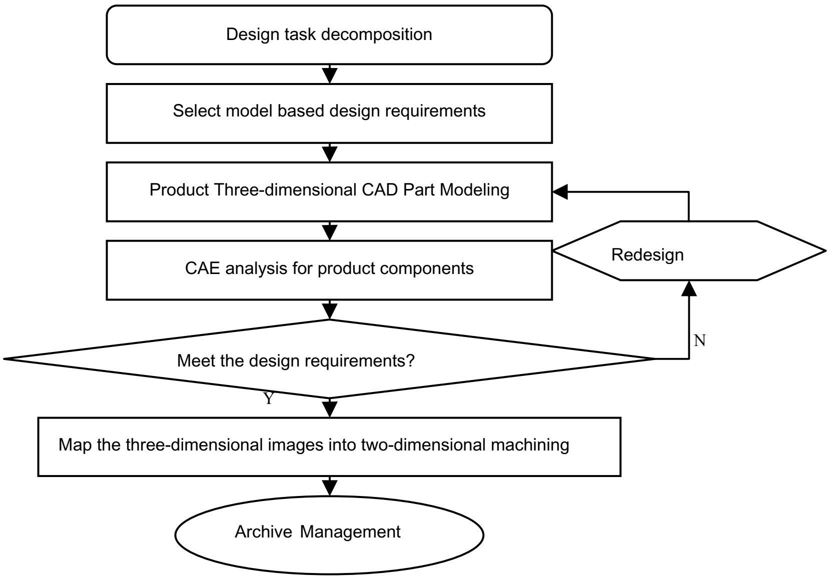

Figure 1: CAD / CAE integrated design software platform   Figure 2: Integrated design flow of CAD / CAE

CAD / CAE integrated design process is shown in Figure 2. Various performance, strength, reliability and durability of mechanical equipment can be calculated and analyzed as early as in product development stage. Possible problems can be discovered and solved in product research and development stage. This will shorten product design cycles, save development costs, improve product design quality and ensure product reliability.

**Cultivating Compound Talents.** Elements of simulation design activities are shown in Figure 3. CAD / CAE software are used by engineers and researchers finally. So the integrated design idea also needs to be implemented by them. Thus, the key factor of digital design is cultivating compound talents with plenty of relative knowledge and experience.

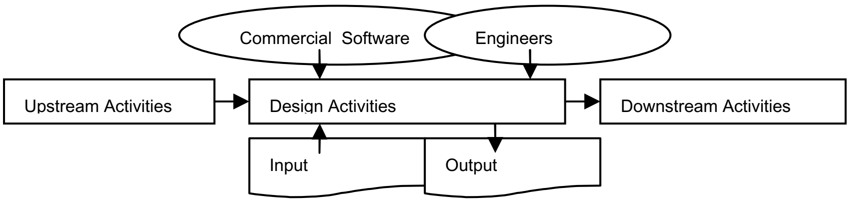

Figure 3: Elements of simulation design activities

Integrated design requests engineers to perfect knowledge systems and accumulate experience. Take the servo valve CAD/CAE integrate design with computational fluid dynamics method for example. The designers are required to be familiar with operating performance and internal flow of hydraulic valve in the hydraulic system.

**Experimental and Simulation Complement Each Other.** Known from figure 3, digital design cannot carry through without experimental support, which is determined by the problem itself completely. Because digital design is the process of accumulation of user's knowledge gradually, all-digital design is impractical and unnecessary. For example， input parameters of finite element model, such as damping coefficient, damping ratio must come from experimental or engineering experience.

Experiment and simulation are complementary relationship: simulation can replace some experiments to some extent. Simulation could provide the basis for design and improvement of experiment. This will reduce costs and shorten the cycle of research and development. On the other hand, experiment provides input parameters and validates the results for simulation. In the future, experiments are not independent behavior but vital factor that will promote the whole R&D process.

**Design Reuse.** In new product development process, design reuse technology should be used to make full use of existing business design resources and reduce duplication of development work. For example, the designers could establish standard parts warehouse and the user model base, standard material library and user material library to avoid design duplication, such as: the establishment of bolted parts library, experiment shaking table model base and fixture warehouse. Engineering design and processing graphs should be managed on file. And it is also necessary to establish the user knowledge base. These activities will provide documentation for use restraint and guide the engineering experience.

**Intelligence and Automation.** The aim of digital is to improve the design efficiency and release human from the heavy repeat work. Therefore, users should make full use of design approach supplied by intelligent, automatic and "fool-style" software. The design approaches include automatic optimization design, structure optimization, parameter optimization design, mesh generation optimization and dynamic stiffness optimization, and so on. With the assistance of these methods, the users will reduce the settings and operations and finally the possibility of making errors. Commercial software generally provides users with two different modes of common operations, as shown in Table 1. The common users firstly complete initial design through a GUI operation. Then experts execute professional optimization with the high-level commands.

Table 1: Two different operation modes supported by commercial software

| operation mode | GUI | advanced command stream |
|---|---|---|
| user features | weak professional knowledge, less engineering experience, not familiar with software | rich of professional knowledge and engineering experience， familiar with software |
| operation features | imagery, intuitive, easy to operate, fool-based GUI interface, little user settings and operation, user actions limited | command-line operation, powerful, multi-user settings and operation, user actions unlimited, error-prone |
| application scope | simple engineering problems, suitable for beginners | specific problems, professional design,, optimization |

**Workflow Customization and Application development.** Open Workflow Architecture of Commercial Software allows user to execute "individual customization" of process accordance with requirements. Enterprises can solidify engineering design, experimental results and parameter settings, and form a clear workflow.

According to characteristics and industrial application requirements, enterprise should make application development based on a full absorption of the introduced business software. It is known from table 2, as long as the choice and application of development method is proper, application development could not only absorb the latest achievements of engineering practice and scientific research, but can also inherit the advantages ,while avoiding the disadvantages of complete independent software development.

Table 2: Compared between application development and complete independent software development form

| development approach | implementation method | scope | advantage | disadvantage |
|---|---|---|---|---|
| application development | 1)using the application development interface, tool and language, built based on commercial software ;<br>2)according to user's needs, customizing new module, and achieving new algorithm | 1)software localize and customization；<br>2)applications extended, engineering practice experience formal;<br>3)implement and integrate new algorithms | 1)seamless integration with business software and exchange；<br>2)operation stable;<br>3)short development cycle, less technical and resource devotion | functionality and performance largely depend on capabilities and openness of the commercial platform |
| complete independent software development | beginning from zero, completely building all modules with high-level language | bringing the latest scientific research algorithms into application software | 1) suitable for highly complicated and exceptions<br>2) complete intellectual property rights；<br>3)professional, efficient;<br>4)customizable output, debugging | 1)difficult comprehensive investigation;；<br>2)difficult with commercial software, with weak market competitiveness；<br>3)difficult realization of programming,<br>4)poor stability |

## Conclusions

The problems in use of commercial CAD / CAE software are summarized in this paper generally. Digitalization is a long and complex process which needs experience accumulation and perpetual improvement. Only with hard exploration and the aforementioned way of unremitting improvement according to actual circumstances, can CAD / CAE software meet individual requirements of enterprise and maximize its efficiency.

Future research directions include a wider range of process integration and collaboration, development direction and technical difficulties of commercial CAD / CAE software.

## References

[1] Bor-Tsuen Lin and Chun-Chih Kuo. The International Journal of Advanced Manufacturing Technology. Volume 35, Numbers 9-10, 1000-1013, 2008.

[2] Xiao-xia LIN, Shu-you ZHANG, Jing CHEN, Zhen ZHAO. Computer Integrated Manufacturing Systems. 2296-2302,2009 -12(In Chinese).

[3]Terzic, I., Zoitl, A., Favre, B., Strasser, T.. A survey of distributed intelligence in automation in European industry, research and market. Emerging Technologies and Factory Automation, 2008. ETFA 2008. IEEE International Conference on.

[4] AJ Albrecht, JE Gaffney Jr.Software Function, Source Lines of Code, and Development Effort Prediction: A Software Science Validation Software Engineering, IEEE Transactions on 2006 - ieeexplore.ieee.org.

*Advanced Materials Research Vols. 201-203 (2011) pp 40-43*
*© (2011) Trans Tech Publications, Switzerland*
*doi:10.4028/www.scientific.net/AMR.201-203.40*

# A Method of Machining Region Planning for Tyre Tread Mold Machining

Jiansheng Liu[a], Haining Tu[b], Fangchen Xia[c], Junxing Xiong[d]

School of Mechanical and Electronic Engineering, Nanchang University, Nanchang
,Jiangxi,330031,China

[a]victorljs@163.com, [b]cthn@163.com, [c]cxfc@163.com, [d]jx811217@163.com

**Keywords:** Tyre Mold; Machining Region Planning; Inner and Outer Contour Recognization

**Abstract.** To satisfy the manufacturing requirement of tyre tread pattern mold, the problem of machining region planning in the computer aided manufacturing of tyre mold is introduced. And it is analyzed that the core technology is the definition of inner and outer contours for machining region planning and tool-path planning. According to the defect of traditional constructed way of machining region, an auto recognition method of inner and outer contour is studied based on the inclusive test method.The detail step of the method is illustrated.Thinking about the special condition of the method, corresponding strategy is given. This method is applied in the computer aided manufactuing of tyre tread mold, by which machining region planning can be solved effectively.

## Introduction

Automobile tyre enterprises progresses with each passing day, and new product emerges one after another. Tyre mold is one important process equipment for tyre manufacturing, which plays very role for product quality. The manufacturing tendency of tyre mold is NC manufacturing, so only by the CAD/CAM can tyre mold succeed in improving the quality and cycle-time reduction. Relative paper,for examples, Cavity surface construction of tyre tread pattern mold and its finish machining[1], Application of CAD/CAM Technology in Engraving Letter on Tire Mold Sidewall[2]. In the current CAM software, machining region planning is done by the way of selecting the contour boundary one by one. Efficiency is low for this method, and it is easy to do wrong.In this paper, taking the case of tyre tread mold, a method of machining region planning is provided for tool-path planning.

## Tyre Tread Types and Its Machining Method

Tyre tread types include letters, Chinese character, arabic number and company logo. There are two sorts of tread pattern in tyre mold, which include solid pattern and hollow pattern. According to the character of machining region, solid pattern can divided into single-line solid pattern and wide solid pattern. The same as solid pattern, hollow pattern can also divided into single-line hollow pattern and wide hollow pattern.The detail explain is as following.

**Single-line Solid Pattern.** It consists of arabic number and letter. The pattern whose line-width is less than 1mm can be defined as single-line solid pattern. In CAD model, patter geometry model contains contour line and center line. Center line is basis of machining-path, and that contour line is only to check.The left part in the fig.1 is CAD model of letter “A”, in which the black line is contour line, and the red line is center line.The right part in the fig.1 is machining result(following is the same as).

**Wide Solid Pattern.** The pattern whose line-width is more than 1mm belongs to wide solid pattern. Its geometry model includes inner contour and outer contour. In generally,tool-path planning of this pattern is by the way of inner contour offset and outer contour offset.Its CAD model and machining result are shown as fig.2.

**Single-line Hollow Pattern.** The width of machining region is less than 1mm in this pattern. And its machining method is to finish machining along with center line of pattern contour only once. Center line is basis of machining-path, and that contour line is only to check. Its CAD model and machining result are shown as fig 3.

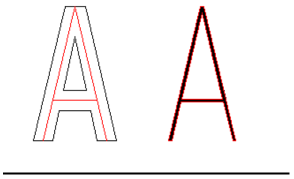

Fig.1 Single-line solid pattern

Fig.2 Wide solid Pattern

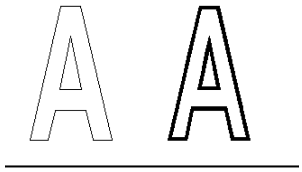

Fig.3 Single-line hollow pattern

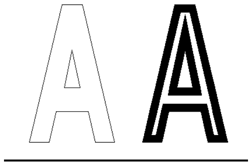

Fig.4 Wide hollow pattern

**Wwide Hollow Pattern.** Its geometry model consists of inner contour and outer contour. Inner contour and outer contour offset based on fix width. Inner contour offsets toward outer, and out contour offsets toward inner. Then new contour is got. Its CAD model and machining result are shown as fig 4.

## Description of Machining Region

The machining way can be divided into the surface machining and the single-line machining, in accordance with the different machining methods. For example, number pattern belongs to single-line machining, that is to finish machining along with the contour only once. Otherwise, most solid patterns and wide hollow patterns adapt to the surface machining.Tool path planning can be satisfied for the single-line machining as long as the structure of contour is known. And for the surface machining,we should get the cutter location points and its step at first,then the tool path of outer contour offset inward and inner contour offset outward step by step.Therefore the core problem for tyre pattern machining is tool-path planning by offset of inner and outer contour.

## Machining Region Recognization Algorithm

In the field of computer graphics, contour is defined as suface boundary, and surface is the region encolsed by contour. A specific region is mostly enclosed by inner contours and outer contours or a single outline. In the fact process of mechanical machining, it aims at the maching region. The inner contour is the internal boundary of the machining region, the outer contour is the external boundary.So that,the identification of inner and outer contours is the basis of derminating maching region.

A contour is an colsed loop, which consists of segments or curves connected one by one.Maybe it exists inclusion relationship or intersection relationship between contours, so it is not good to judge the location relationship among contours. In this paper , strategy is to select one point on one contour. Then,the mutual position relationship between contours is obtained by determining the inclusion relation of this point in another contour. There are many algorithm about point in polygon testing, such as point in polygon testing [3], Orientation and Point Inclusion Test for Planar Polygon[4], A New Method Deciding Whether a Point is in a Polygon or a Polyhedron[5]. Line cross-point method is presented in this paper to decide whether a point is in one contour. Steps of the algorithmare as follows:

*Step 1. Taking some points*

A contour is an colsed loop, which consists of lines or curves connected one byone. So, the first step is to take one point from some line of two contours.

*Step 2. Getting a line from two points*

Let one point as testing point getting from step 1. Then it is regard as starting point, and a line will get by connecting these two poine

*Step 3. Counting the number of intersection points*

After calculating the intersection points between the line and the contour in which another point is in. the number of intersection points can be gotten.

*Step 4. Determining the parity of the number;*

*Step 5.Determining whether the two related contours intersect or not;*

*Step 6. Judgement .*

If the number of intersection points is the even,then the contour with the line starting point and this contour doesn't contain each other;if the number of intersection points is the odd number and the two contours don't intersect each other,then the contour with the starting point is the inner contour,the other related contour is the outer contour; If the number of intersection points is the odd number and the two contours intersect each other,then we define that the contour with the starting point and this contour doesn't contain each other.

In this line cross-point method, there are two special conditions. One is the line go through the vertices of another contour, such as point D in the fig.5. Another hand is the line coincide with some edge of another contour, such as point C in the fig.5. It is hard to judge parity.

For these two special conditons, in order to ensure the intersection between rays and contours, and avoid lien through vertices or line coincide with some edge of contour polygon,points were selected the middle point of the No.1 line on each contours as test points,then auxiliary line for discrimination are made from one point as starting point to another one,the location relations are determined between every two contours. Another general strategy is to get another auxiliary line, connected by the middle points of No.2 line on each contour . Then the algorithm goes on from the step 3.

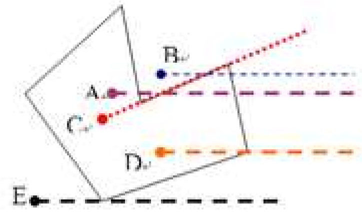

Fig.5 Sepcial conditons about point in polygon testing

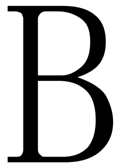

Fig.6 one machining region consisting of one outer contour and two inner contour

**Application Example**

Machining region of some numbers and logo patterns are composed by a outer contour and some inner contours.As shown in figure.6. Aiming at these conditons, it is to view all groups' outer contours after the information of machining groups is obtained. If a contour is many groups' outer contour, at the same time these groups' inner contours don't compose groups each other,then all of these related groups are defined as a machining region.Marking the machinning region and recording its information,the single outer contour is the machining region outer boundary and the related inner contours compose its inner boundary.

## Conclusions

It is tendency to apply CAD/CAM in the process of mold manufacturing.The description of machining region recognization is explained , and it points out that the basis is the definition algorithm of inner contour and outter contour. Based on point in polygon testing, a line cross-point method is give. For avoiding two special conditions in this method, some effective strategies are provided. The method is applied into fact mold manufacturing. The result shows that it do well in recongizing inclusion relationship between contours, and it can judge among any comflex contour.

## References

[1] WANG Qian-ting, LIU Qiong, LIANG Xi-kun.Journal of Zhejiang University (Engineering Science). Vol. 40(2006),p309.

[2] LI Shu, LI Ye. Contemporary Chemical Industry. Vol, 38(2009),p129.

[3] YAO Xue-ying and CAI Ying-ji. Computer-aided Design and Manufacturing. Higher Education Publishing House, 2002.

[4] LI Wei-Shi LI Jiang-Xiong KE Ying-Lin.Journal of Computer Aided Design and Computer Graphics, Vol 12( 2000),p405.

[5] WANG Wen-cheng1, WU En-hua1. Journal of Software, Vol, 11(2000),p114.

*Advanced Materials Research Vols. 201-203 (2011) pp 44-48*
*© (2011) Trans Tech Publications, Switzerland*
*doi:10.4028/www.scientific.net/AMR.201-203.44*

# Finite Element Analysis of Laminating Press Frame

Xinzhou Zhang[a], Shangbin Wang[b], Kai Wu[c], Yu Sun[d]
School of Mechanical Engineering, Nanjing University of Science & Technology,
Nanjing 210094, China
[a]zhangxinzhou1984@126.com, [b]wsbin@hotmail.com, [c]wukai@mail.njust.edu.cn,
[d]sunyu@mail.njust.edu.cn

**Keywords:** Laminating Press; FEM; Static Analysis.

**Abstract.** The structural characteristics of a laminating press were analyzed, and the corresponding finite element model was built with some essential simplification. By structural analysis, the distributions of stress and strain were obtained, based on which the rationality of the frame design can be verified. According to the complex structure and loading conditions of the laminating press, four analytical schemes with different models and boundary conditions were adopted, then the results of different analytical schemes were compared, and the causes resulting in the calculation differences were analyzed. The result shows that in analyzing different parts of the laminating press frame, different models and boundary conditions were required.

## Introduction

China is one of the countries with deficiency of forest resources. In recent years, as the architectural decoration and furniture industry grow fast, the domestic demand for lignum is increasing rapidly; as a result, the supply shortage of lignum becomes more and more serious. One of the effective ways to relieve such shortage is to depend on wood-based panel industry, which at the same time can save the lignum resources. With several years of rapid development, the domestic output of wood-based panel has been No.1 in the world for years.

Although China has become a country with great productive capacity of wood-based panel, there still exists some problems , such as structural irrationalities, lower technology, shortage of resources, low industrial centralization etc.. Especially in the innovations of product, technique, equipment and process technology, there are big gaps compared with some foreign countries [1].

The laminating press has a major application in secondary working for surface decoration (paper & veneer) of OSB & MDF/HDF, and the panels treated with the press can be used on furniture, interior finishes, laminate flooring and building. The press is the last actuator of the forming process of the wood-based panel and the rigidity and accuracy of the parts of the press affect directly the quality of the products. Therefore, the frame, one of the most important parts of the press, is the focus of the design in the entire assembly line.

## Structural analysis of laminating press frame

The laminating press which bears the major load consists mainly of a frame, cylinders, a moving beam and hot pressboards. It has two types of structures: the combined structure and the integral structure. The combined structure, including upper beam, lower beam and upright column in the middle, is connected by bolts to form a rigid frame, or called column frame. The integral structure is to use a block of steel plate, or to weld together some pieces of steel into an integral frame, or called frame structure [2].

The structure of laminating press frame is shown in Fig.1. The laminating press frame consists of six frame plates or three frame groups (each frame group is formed with two frame plates). The three frame groups, which are fixed to the base, are also joined together with some bolts, and this kind of installation brings the structure a higher lateral rigidity [3].

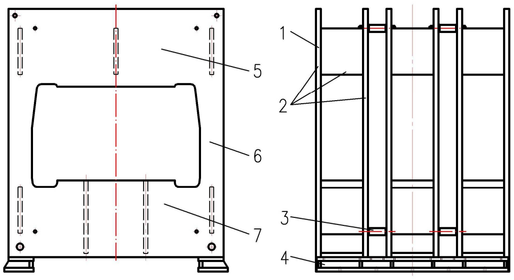

Fig. 1 Schematic diagram of the laminating press frame
1—Frame plate 2—A group of frame
3—Connecting bolt 4—The foundation
5—The upper beam of frame 6—Column of frame 7—The lower beam of frame

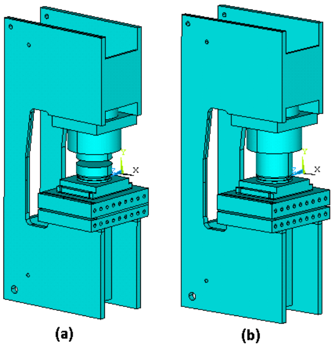

Fig. 2 The finite element model of the laminating press frame
(a) Model of analytical scheme 1 and 2
(b) Model of analytical scheme 3 and 4

Working parameter of laminating press frame is shown in Table 1. Some parts (such as hydraulic cylinder, hot pressing board, etc) are included to get good results corresponding to the actual solution smoothly in this paper.

Table 1 Parameters of the laminating press frame

| Parameter | Numerical Value |
|---|---|
| Total pressure of the press/KN | 14000 |
| Size of hot pressing board/mm | 1400×2600 |
| Size of panel/mm | 1220×2440 |
| Ram diameter of main hydraulic cylinder/mm | 360 |
| Closing speed of the press/mm/s | 120 |
| Opening speed of the press/mm/s | 100 |

## Finite element analysis of laminating press frame

**Finite element model of laminating press frame.** Due to the complicated structure and large size of the press, some simplifications are adopted in order to make the analysis more convenient [4-7]: firstly, ignore all screw holes, small holes and fillets, which will not affect the calculation results, and consider all welds in the actual model as an integral part; secondly, displacement constraints are imposed on some small areas of the frame bottom; thirdly, considering the performance of computer, the symmetries of structure, constraints and load, a half of the single group model is used for analysis, and symmetry constraints are imposed on the symmetry plane; fourthly, ignore the thermal radiation of the hot pressboard.

Four analytical schemes are taken in this paper and the comparisons of the analytical schemes are shown in Table 2. The differences of the different schemes depend on whether the contact analysis is taken and where the loads are imposed.

Table 2 Comparison of the analytical scheme

| Scheme | Scheme one | Scheme two | Scheme three | Scheme four |
|---|---|---|---|---|
| Contact analysis | Yes | No | Yes | No |
| Breaking cylinder | Yes | Yes | No | No |
| Panel included | Yes | Yes | No | No |
| Load applied/ MPa | 25 | 25 | 5.215 | 5.215 |

The finite element model of the laminating press frame is shown in Fig. 2. Fig. 2(a) shows the model of Scheme one and two.The model of Scheme three and four is shown in Fig. 2(b).

**Material property.** Material property of frame, cylinder, hot pressing board and so on: Young's modulus is 206GPa and Poisson's ratio is 0.3. Material property of cushion plate which is made of bakelite: Young's modulus is 2.5GPa and Poisson's ratio is 0.35.

**Element.** Solid95 element is adopted for the complex stress and strain condition. Solid95 is a higher order version of the 3-D 8-node solid element Solid45. It can tolerate irregular shapes without much loss of accuracy. Solid95 elements have compatible displacement shapes and are well suited to model curved boundaries [8].

**Boundary Conditions.** The horizontal displacement of the press is zero, symmetry constraints imposed by the symmetry plane. All displacements of the small area of the lower surface of the lower beam are zero.

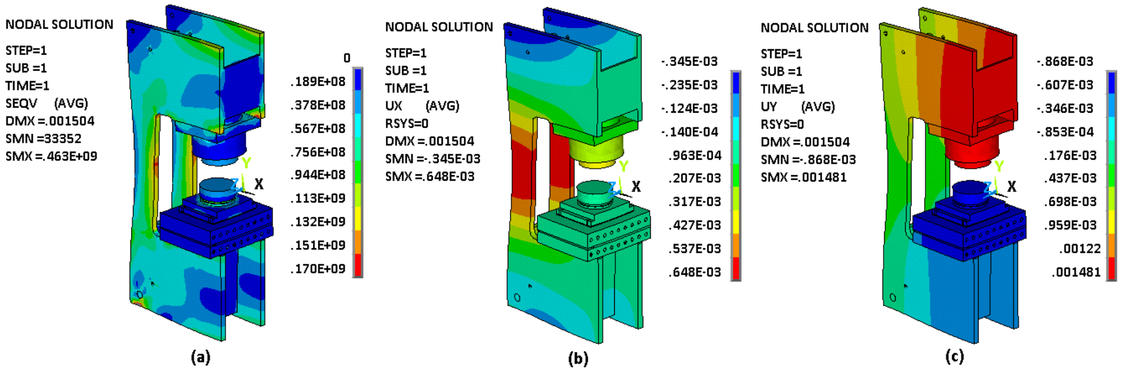

Fig. 3 Stress and displacement of analytical scheme 1
(a) Distribution of Stress (b) Distribution of X direction displacement
(c) Distribution of Y direction displacement

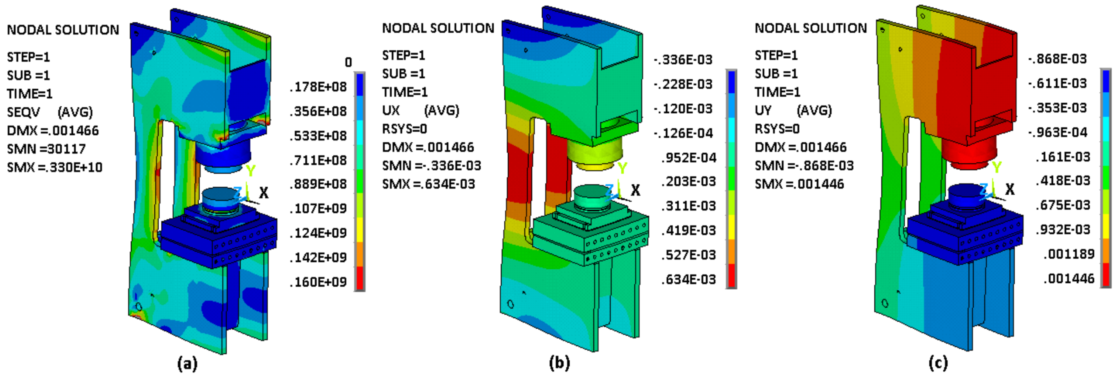

Fig. 4 Stress and displacement of analytical scheme 2
(a) Distribution of Stress (b) Distribution of X direction displacement
(c) Distribution of Y direction displacement

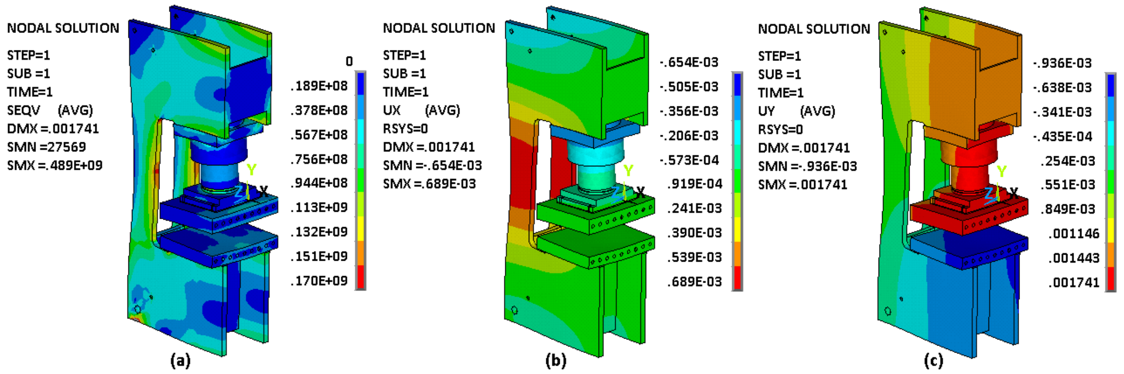

Fig. 5 Stress and displacement of analytical scheme 3
(a) Distribution of Stress (b) Distribution of X direction displacement
(c) Distribution of Y direction displacement

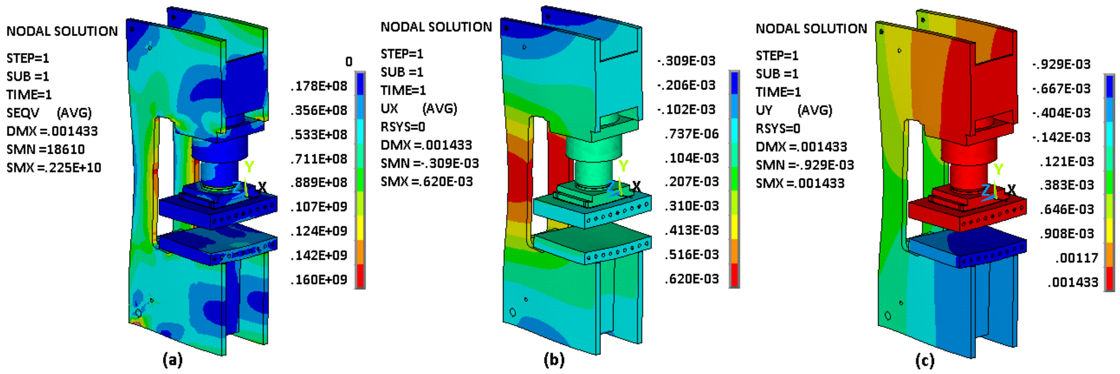

Fig. 6 Stress and displacement of analytical scheme 4
(a) Distribution of Stress (b) Distribution of X direction displacement
(c) Distribution of Y direction displacement

**Result of the calculation.** X direction lies along the width direction of the press, Y direction lies along the vertical direction and Z direction lies along the perpendicular direction of the press plane. The stress distributions and deformation of the press are shown in Fig. 3-6. From the figures one can see that each member has lower stresses regardless of local stress. As shown in Table 3, the maximum stress of the upper and lower hot pressboard is less than the counterparts of the frame, and the global analysis results are bigger than those in the contact analysis.

Table 3 Maximum stress of each member (MPa)

| Scheme | Scheme one | Scheme two | Scheme three | Scheme four |
|---|---|---|---|---|
| Frame | 178 | 183 | 170 | 203 |
| The upper hot pressing board | 25 | 26 | 44 | 30 |
| The lower hot pressing board | 31 | 31 | 42 | 43 |

The frame is made of A3 steel with yield stress 235MPa.The maximum stress of the frame, which is around filleted corner, is in a small area and the stress of the rest is lower. But in general, the frame can meet the requirements of use.

Table 4 Maximum displacement of frame (mm)

| Scheme | Scheme one | Scheme two | Scheme three | Scheme four |
|---|---|---|---|---|
| The upper beam of frame | 1.399 | 1.373 | 1.445 | 1.246 |
| The lower beam of frame | 0.534 | 0.533 | 0.525 | 0.518 |
| Column of frame | 0.641 | 0.627 | 0.687 | 0.612 |

Rigidity analysis of the frame includes two parts: the deflection of the upper and lower beam along vertical direction and the maximum displacement of column along X direction. As shown in Table.4, the maximum displacement of upper and lower beam and the column by contact analysis is bigger than that by global analysis; for the reason that the rigidity of the frame with contact analysis is smaller.

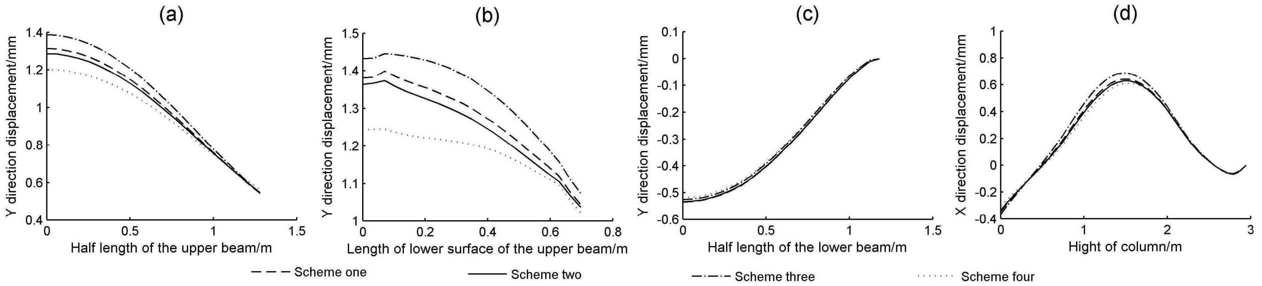

Fig. 7 The curve diagram of the frame deformation
(a) The upper surface of the upper beam (b) The lower surface of the upper beam
(c) The lower surface of the lower beam (d) The lateral surface of the frame column

In Fig.7 (a) and (c), the displacement curves of the top surface of upper beam and the bottom surface of lower beam are plot by half due to their symmetry respect to Y-axis, which represent their symmetry plane. The displacement at the edge between the interface and non-interface of the cylinder on its installation plane, the bottom surface of upper beam, does not change consecutively, as a result, a inflexion point can be found in each displacement curve, see in Fig.7(b). From Fig.7 (d), one can see that the maximum displacement of column is in the symmetry plane of the inner window.

The calculating results of lower beam and the column obtained in different schemes have no big difference, while the calculating differences of the top and bottom surfaces of upper beam in different schemes are obvious.

For the deformation analysis of upper beam, the rigidity results of the third scheme are closest to the actual situation, and it is regarded as the optimum scheme. For other analysis, the differences of the results in different schemes are negligible, so the second or the fourth scheme can be regarded as the optimum one in consideration of improving efficiency.

## Conclusions

The intensity and rigidity of the laminating press frame were analyzed based on four finite element analysis schemes. The following conclusions can be drawn:

(1) According to the intensity and rigidity analysis of the press frame based on ANSYS, some optimizations can be made for reducing costs.

(2) Though contact analysis was more accurate, the differences between contact analysis and global analysis were negligible. Therefore, in the perspective of efficiency enhancement and qualitative analysis, the global analysis was favored. The contact analysis will be used for better accuracy.

(3) Due to the complexities of the structure and working conditions of the press, detailed analysis is needed instead of a general one. The result shows that different models and boundary conditions were required to analyze different parts of the laminating press frame.

## References

[1] YU Wen-ji, GUAN Li-li, Wu Da-wei. China Wood-Based Panels, Vol. 1-5(2009), In Chinese.

[2] WU Xin-quan, LUO Yu-ming, QI Sheng-tian: Wood-based Panel Multiplaten Press (China Forestry Publishing House, China 1985), In Chinese.

[3] Wang Ye-ping, Wu Zhan-wei. Mechanical Research & Application, Vol. 86-87(2005), In Chinese.

[4] LI Yue-xian, Qi Xiu-mei. Mechanical Engineering & Automation, Vol. 70-71(2008), In Chinese.

[5] LV Lin, DENG Ming, LI Yan-xia, WANG Zheng-li. Forging & Stamping Technology, Vol. 102-105(2010), In Chinese.

[6] GAO Xiang, HU Miao. Journal of Machine Design, Vol. 62-64(2009), In Chinese.

[7] WANG Shang-bin, SUN Yu, ZHANG Qing-fei. Forging & Stamping Technology, Vol. 83-86(2009), In Chinese.

[8] Information on Release 10.0 Documentation for ANSYS.

*Advanced Materials Research Vols. 201-203 (2011) pp 49-53*
*© (2011) Trans Tech Publications, Switzerland*
*doi:10.4028/www.scientific.net/AMR.201-203.49*

# Lightweight Design of Electric Scooter Frame by Finite Element Optimization

Hongbo Dong [a], Wei Zhang [b]

School of Aeronautical Manufacturing Engineering, Nanchang Hangkong University, Nanchang, Jiangxi, 330063, China

[a]donghbo@gmail.com, [b]nihaowoshiwei@sina.com

**Keywords:** Electric Scooter Frame; Structure Optimization; Finite Element Analysis

**Abstract**. To reduce the weight of the electric scooter frame, magnesium alloy is used to replace the steel. At the same time, the frame structure and tube thickness are redesigned by using topology optimization and size optimization respectively. In addition, static analysis and mode analysis of the frame are carried out to realize the application capability and dynamic capability. Compared with the original steel frame, mass of the magnesium alloy frame after optimization has been reduced by 60%, and the natural frequency has been improved greatly. The results show that the strength and the rigidity of the new structure can meet the designed demand.

## Introduction

Recently, how to develop a structure with high strength and light weight has become one of the important duties of vehicle design. However, lightweight structure has a great impact on strength and rigidity of vehicles, so the structural strength and weight need to be coordinately handled. So far, optimization techniques have been applied in the initial stage of structural design. Compared with the method of trial and error, they have the advantages of high-efficiency and low cost. The traditional methods for optimum structural design include topology optimization, shape optimization and size optimization [1-4]. In addition, the high-strength light metal can be used to greatly reduce the structural weight. Magnesium alloy has been widely used in fields of aerospace, automobile, electronic communication due to its advantages of light weight and high specific strength[5,6]. In recent years, magnesium alloy components have been more and more widely used in electric scooter, with satisfactory results [7].

At present, large weight and short mileage are common problems in the electric scooter market. Lightweight design on a certain type of electric scooter can be carried out for developing high-end market. Although using magnesium alloy instead of the original steel frame that can reduce weight, redesigning the original structure to enhance the comprehensive performance of products is necessary. In this paper, the optimization module of finite element analysis software Hyperworks is used for carrying out topology optimization and size optimization to frame. At the same time, strength analysis and modal analysis are both achieved to get the structural sizes that could meet the designed demand.

## Analysis of the original frame structure

General drawing of the original frame of electric scooter is shown in Fig.1. The load bearing structure namely the main frame is welded by 1.5-mm-thick steel tube, and diameter of the riser is 40 mm and the others are 32 mm. Material is 45 steel, yield strength is 355 MPa, density is 7.85

g/cm$^3$, elastic modulus is 210 GPa, Poisson's ratio is 0.3. The main frame whose weight is 4.5 kg is in charge of loading the crew and the battery under the seat, the maximum designed load is 2000 N. Finite element model of the main frame of the electric scooter is shown in Fig.2. Static analysis shows that the maximum equivalent pressure in the joint between riser and the chassis U-tube is 274MPa(as shown in Fig.3), the maximum displacement of load position is 5.2 mm. Lanczos method is used to solve unconstrained model, which results show that the first-order natural frequency is 489 Hz , the first-order vibration mode is shown in Fig. 4.

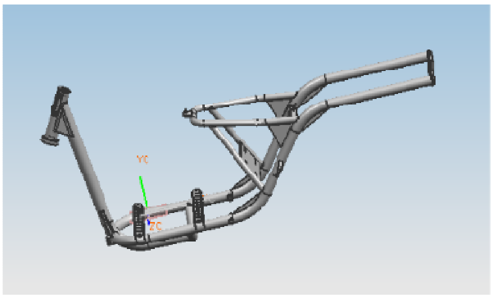

Fig.1 General drawing of the frame

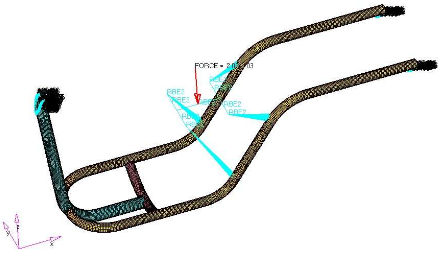

Fig.2 Finite element model of the main frame

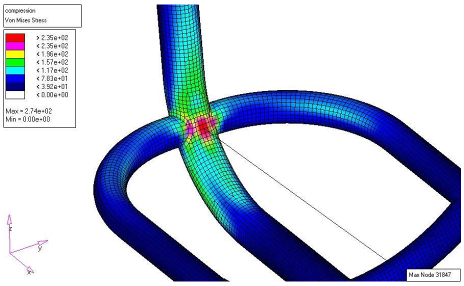

Fig.3 Equivalent stress in the joint area

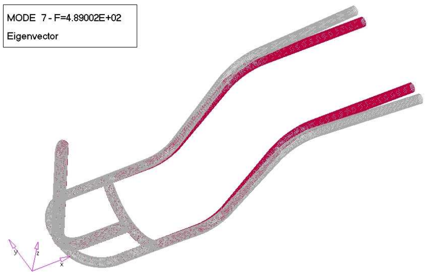

Fig.4 The first-order vibration mode of the frame

## Optimal design

**Topology optimization.** The strength analysis shows that stress in the joint between riser and the chassis U-tube cannot reach yield strength, much higher than other parts. The main frame structure should be redesigned by topology optimization to reduce the stress concentration. The part surrounded by the chassis tube is the optimal design domain, shell elements are used to construct the models and the load and boundary conditions are applied to the main frame (as shown in Fig.5). The maximum structural rigidity is the design objective; the volume that is smaller than 0.25 times of the original volume is constraint after the optimization. Optimization technique of continuum structures is applied based on density method, and the optimization objective function and constraint function are:

objective function min $C(x)$
constraint function s.t. $V(x)-V^U \leq 0$

Among the formula, objective function $C(x)$ is structural flexibility; constraint function $V(x)$ is structural volume, $V^U$ is upper limit of total volume that is 0.25 times of the original volume; and design variable $x$ is unit density which represents the presence or deletion of the unit in microstructure, where density value of each unit should be taken as 0 or 1, so the lower limit is 0 and upper limit is 1.0[8,9]. In this paper, using the density method, unit density is continuously changed between 0 and 1.

Optimization results are shown in Fig.6, where the optimal material distribution of the structure can be seen in setting conditions. According to the results of topology optimization and considering the processing conditions, the structure is shown in Fig.7 can be got. The frame is still welded by 1.5-mm-thick 45 steel tubes, and its mass is 4.4 kg which is slightly smaller than that of the original structure. The load and boundary conditions is the same as the original frame when the new designed frame is carried on with finite element analysis. The maximum equivalent stress is still in the joint between riser and the chassis U-tube, however, the position has transferred from the inside to the outside in the riser(as shown in Fig.8), the maximum equivalent stress value decreases to 212 MPa which is only 77.4% of that in the original structure and the maximum displacement of the position of the applied load is 5.4 mm. Compared with the original structure, the results show that the first-order natural frequency of the new structure is 1138 Hz which increases by 133%, the first-order vibration mode also changes from the original transverse swing into longitudinal buckle.

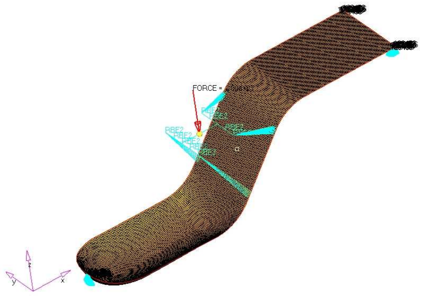

Fig.5 Design domain for topology optimization

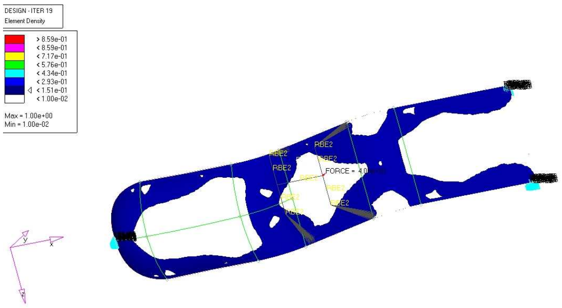

Fig.6 Distribution of material density

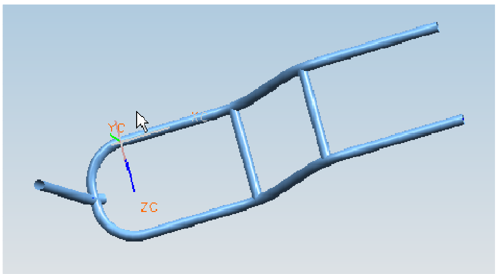

Fig.7 Main frame after topology optimization

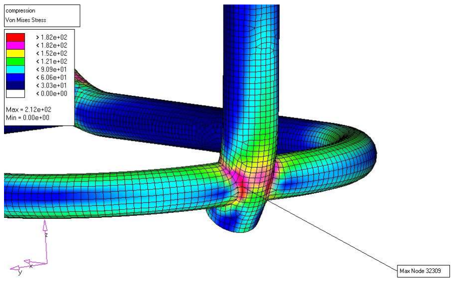

Fig.8 Equivalent stress in the joint area

**Size optimization.** Strength and natural frequency of frame have been greatly improved after the topology optimization. The steel materiel is replaced by magnesium alloy AZ91 to reduce the weight significantly. Its density is 1.80 g/cm$^3$, elastic modulus is 45 GPa, Poisson's ratio is 0.35, and yield strength is 180MPa. The weight of the main frame is 4.5 kg, and all the thickness of the tube is still 1.5 mm. Static analysis shows that the maximum equivalent stress is 209 MPa and the maximum displacement is 25.4 mm, which means that strength and rigidity of the frame are both worsened. Size optimization analysis is carried out to quickly identify various sizes of the appropriate thickness of various parts of tube. Design objective is the smallest volume; constraint is the maximum equivalent stress and the maximum displacement is less than the set value. Objective function and constraint function of size optimization are:

objective function min $V(x)$

constraint condition s.t. $g(x)-g^U \leq 0$

design variables $x^L \leq x_i \leq x^U$

Among the formula, objective function $V(x)$ is structural total volume, constraint function $g(x)$ is the response which is obtained from the structural analysis, where the constraint functions are defined as the equivalent stress and loading- point displacement, and $g^U$ is the maximum equivalent stress and the upper limit of maximum displacement, respectively. Design variable $x$ is the thickness of tube, and $x^L$ and $x^U$ are respectively the lower and upper limits.

For security reasons, the allowable stress of material is 144 MPa that is 80% of the yield stress of magnesium alloy, and the maximum displacement of position of the applied load is not more than 10 mm. Optimized objects are the riser, U-tube and two horizontal tubes respectively. The optimized tube thickness is 1.9mm for riser, 3.3 mm for U-tube and 1.0 mm for two horizontal tubes, respectively. The maximum equivalent stress is 131 MPa and the maximum displacement is 9.7mm.

Table.1 Results of finite element analysis

| Design scheme | Materials | Mass $m$ / kg | Maximum displacement $d$ / mm | Maximum equivalent stress $\sigma$ / MPa | The first-order frequency $f$ / Hz |
|---|---|---|---|---|---|
| Original structure | steel | 4.5 | 5.2 | 274 | 489 |
| Topology optimization | steel | 4.4 | 5.4 | 212 | 1 138 |
|  | magnesium | 1.0 | 25.4 | 209 | 1 103 |
| Size Optimization | magnesium | 1.8 | 9.7 | 131 | 1 302 |

The results of each analysis are summarized in Table 1. The weight of the main frame reduces from 4.5 kg to 1.8 kg, with losses of 60%.The maximum equivalent stress decreases to 131 MPa from 274 MPa, and natural frequency increases from 489 Hz to 1302 Hz. Although the weight has a significant decrease, the structural strength can still meet designed demand. The maximum displacement increases to 9.7 mm from 5.2 mm, which shows structural rigidity has a slight decrease.

Supporting structure based on main frame is designed, and weak areas are increased stiffener plate by welding in order to further enhance its rigidity and strength. Frame of trial production is compact structure and light-weight. Products after assembly are carried out driving test. Finally, test results show that strength, rigidity and reliability of drive are good performance which can prove that the finite element optimization technique is an effective method for vehicle structural design.

## Conclusion

Original steel materials are replaced by magnesium alloy, and the weight of main frame of electric scooter is only 1.8 kg and reduces by 60%, which achieves a substantial decrease. While replacing material, the main frame has been redesigned by using finite element analysis. Compared with the original steel structure, first-order natural frequency of the redesigned magnesium alloy main frame is increased by 166%, so structural strength and rigidity can meet the designed demand absolutely.

A more reasonable mechanical bearing structure is attained by topology optimization, which can enhance the structure strength. On the premise of meeting the design demand of rigidity and strength, size of the minimum thickness of each component can be quickly obtained by size optimization, which improves the design efficiency. The design method may be applied to mechanical structure and design of lightweight components.

## Acknowledgment

This work is financially supported by the National Natural Science Foundation of China (Grant No. 50964012).

## References

[1] Yunkai GAO, Dekan MENG and Xi JIANG: China Mechanical Engineering, Vol.17(2006), p.2522 (In Chinese)

[2] F.Navarrina, I.Muinos, I.Colominas and M.Casteleiro: Advances in Engineering Software, Vol. 36(2005), p.599

[3] S.L.Lee, D.C.Lee, J.I.Lee, C.S.Han and K.Hedrick: Finite Elements in Analysis and Design, Vol. 43(2007), p620

[4] B.Torstenfelt and A.Klarbring: Finite Elements in Analysis and Design, Vol. 43(2007), p.1050

[5] Qichi LE, Xinjian ZHANG and Jianzhong CUI: Materials Review, Vol. 16(2002), p.12 (In Chinese)

[6] A.Tharumarajah and P.Koltun: Journal of Cleaner Production, Vol. 15(2007), p.1007

[7] Shu WANG, Chunsheng SHI, Naiqin ZHAO and Zhongxia XIANG: Materials Review, Vol. 20(2006), p.87 (In Chinese)

[8] Yuanfang FU, Dafeng JIN and Weiwei QIAO: Journal of Mechanical Engineering, Vol. 45(2009), p.210 (In Chinese)

[9] Weihong ZHANG, Jungang YANG and Jihong ZHU: Acta Aeronautica Et Astronautica Sinica, Vol. 30(2009), p.2335 (In Chinese)

*Advanced Materials Research Vols. 201-203 (2011) pp 54-58*
*© (2011) Trans Tech Publications, Switzerland*
*doi:10.4028/www.scientific.net/AMR.201-203.54*

# A Feature-Based CAD-CAE Integrated Approach of Machine Tool and Its Implementation

Wentie Niu[a], Pengfei Wang[b], Yu Shen [c], Weiguo Gao[d] and Lina Wang [e]

[1]School of Mechanical Engineering, Tianjin University, Tianjin, China, 300072

[a]niuwentie@tju.edu.cn, [b]pfwang1987@126.com

**Keywords:** Machine Tool; Analysis Feature; CAD-CAE; APDL

**Abstract.** An analysis feature-based CAD-CAE integrated approach was proposed to solve the problems of rapidly CAE modeling for static and dynamic analysis process of machine tool. Firstly, analysis features were defined in CAD system and analysis feature library was constructed for machine tool and its structural components. Secondly, analysis feature model was constructed by attaching analysis feature to CAD model interactively. Finally, ANSYS parametric design language (APDL) file was generated automatically by mapping analysis features to APDL codes, which realized the integration of CAD system and ANSYS system. Based on application programming interface (API) of SolidWorks, a parametric CAD-CAE tool oriented to static and dynamic analysis of machine tool was developed, which realized parametric modeling and automatic analysis of machine tool and improved design efficiency and quality of machine tool.

## Introduction

The tight integration of CAD-CAE is widely adopted for modern product development. In the digital development process of product, CAD is applied to produce digital model, while CAE focuses on the analysis and simulation of product properties. For complex product design, the meaning of CAD-CAE integration includes: (1) product design model is reused in the process of CAE modeling, furthermore, the structure and function information of product included in CAD model will be reused, which realizes the integration of product information [1-3]; (2) the integration of analysis process, analysis knowledge and function is realized in the typical analysis process, which improves the efficiency and quality of CAD modeling and analysis [4, 5].

An analysis feature-based CAD-CAE integrated approach is proposed in this paper. The structure design of machine tool is completed in CAD system, then analysis feature model is established by defining analysis feature interactively. At last based on the type and specific parameters of analysis feature predefined, the APDL file will be generated automatically by mapping the analysis features to APDL codes, which finally implements the integration of CAD and CAE.

## Feature-based CAD-CAE integrated process of machine tool

The CAD-CAE integrated process based on analysis feature can be seen in Fig.1. The main processes are as follows: (1) CAD model of machine tool is rapidly constructed with the aids of modular and parametric design tools; (2) analysis features are added interactively to CAD model; (3) analysis features are extracted and the APDL file is generated automatically by mapping analysis features to APDL codes; (4) the CAD model is simplified and converted into CAE geometric model; (5) the CAE geometric model is imported into ANSYS and the APDL file is run, finally the CAD-CAE integration is implemented.

Compared with others, this approach has the following advantages: (1) analysis features are added interactively, which makes the CAE modeling has greater flexibility; (2) APDL codes are mapped directly from analysis features, which make the model simplification, element generation, boundary constraint and load addition knowledgeable and intelligent. In addition, the CAE analysis automation is also implemented.

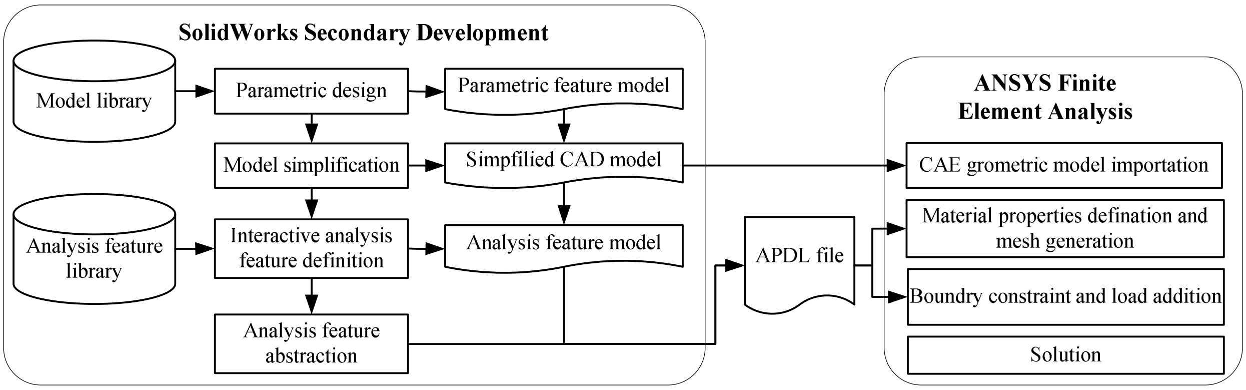

Fig.1 CAD-CAE integrated process

### Analysis feature modeling for static and dynamic property analysis of machine tool

As it is difficult to extract analysis parameter from the design feature directly, the analysis feature model is constructed interactively, which is used for static and dynamic analysis of machine tool. The key issue of this approach is to construct the analysis feature library and define analysis model interactively for typical analysis process.

**Analysis feature model.** The static and dynamic analysis of machine tool include: (1) strength and stiffness analysis of machine tool and its main structural components, which belongs to the static analysis; (2) modal analysis of machine tool and its main structural components, which belongs to the dynamic analysis. According to static and dynamic analysis requirements of machine tool, analysis feature is constructed with five such classes: *Overall Analysis Feature*, *Material Feature*, *Boundary Constraint Feature*, *Load Feature* and *Interface Feature*. The structure of analysis feature classifications can be seen in Fig.2.

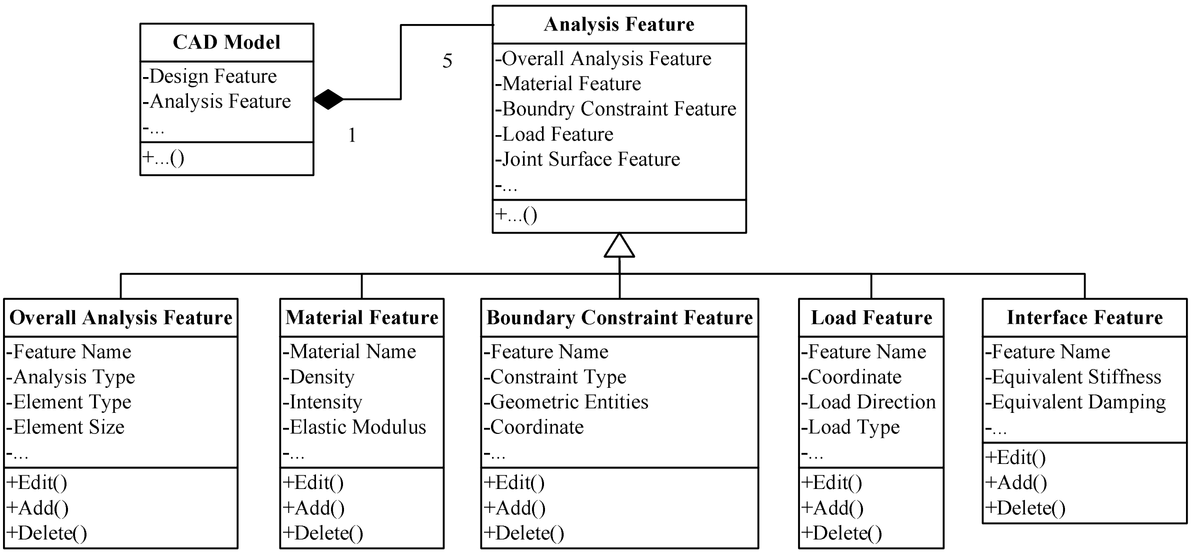

Fig.2 Structure of analysis feature class

With the aids of SolidWorks API, the parameters of analysis feature are attached to geometric entities (point, line, face and feature) and other geometric entity through SolidWorks attribute. Attribute is a container of user-defined variables. With the help of it, user-defined variable can be stored in CAD model. After adding attribute to design feature, the specific information of analysis feature can be obtained rapidly by traveling instances of attribute, which is associated with analysis feature. The essence of analysis feature addition is the attribute addition for the design feature of CAD model, which is the binding of analysis feature and design feature [5]. For static analysis of the bed, Table 1 shows the major analysis features.

Table 1 Analysis feature of the bed

| Graphic Sample | Feature Type | Location Of Analysis Feature | Feature Parameter |
|---|---|---|---|
| 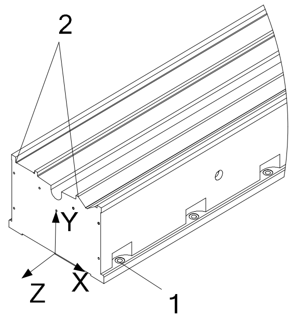 | Boundary Constraint Feature | 1. Cylinder of bolt hole | Coordinate: (0.45, 0.03, -0.2)<br>……. |
| | Load Feature | 2. Endpoints of guide ridge | Coordinate: (-0.42,0.53, 0)<br>Load Direction: -Y<br>Load Type: uniform<br>…... |
| | Material Feature | Attribute abstract of functional module | Material Name: HT200<br>Poisson Ratio: 0.25<br>...... |
| | Overall Analysis Feature | Attribute abstract of functional module | Analysis Type: static<br>Element Size: 0.3<br>…… |

**Interactive defining and modeling approach of analysis feature.** To construct analysis feature model, the definition of analysis feature is accomplished by the way of interactive defining. The main processes are as follows: (1) selecting the type of analysis feature to be added; (2) selecting the geometric entities (point, line, surface and feature) according to the type of analysis feature; (3) inputting parameters of analysis feature; (4) attaching analysis feature to geometric entities and files so that the information of analysis feature can be stored in CAD model.

In the interactive defining process, on the one hand, analysis feature can be added interactively; on the other hand, parameters of the analysis feature can be modified if it is necessary. For example, if the length of the bed needs to be increased when it can not meet the requirement after CAE analysis, after parameters of the CAD model is modified, the number of bolts is also changed, so it is necessary to attach analysis feature to those new added bolts.

## Mapping of analysis feature to APDL codes

**Document structure of APDL file.** APDL is a scripting language for parametric design by ANSYS, which can be interpreted line by line. Inputting APDL codes of the model in a parametric way, ANSYS can accomplish the Finite Element Analysis (FEA) process automatically. There are three stages in the FEA process, including pre-processing, solution and post-processing. Pre-processing includes geometric model importation, material properties definition, boundary constraints addition, load addition, solution type definition and other universal processing modules. After combining these universal processing modules together according to the process of FEA, APDL file is generated.

**Automatic generation of APDL file.** Based on the structure of APDL file, APDL codes can be generated automatically by establishing the mapping relationship between analysis features and APDL codes. For example, the mapping process of the boundary constraint features of the bed is shown in Fig.3.

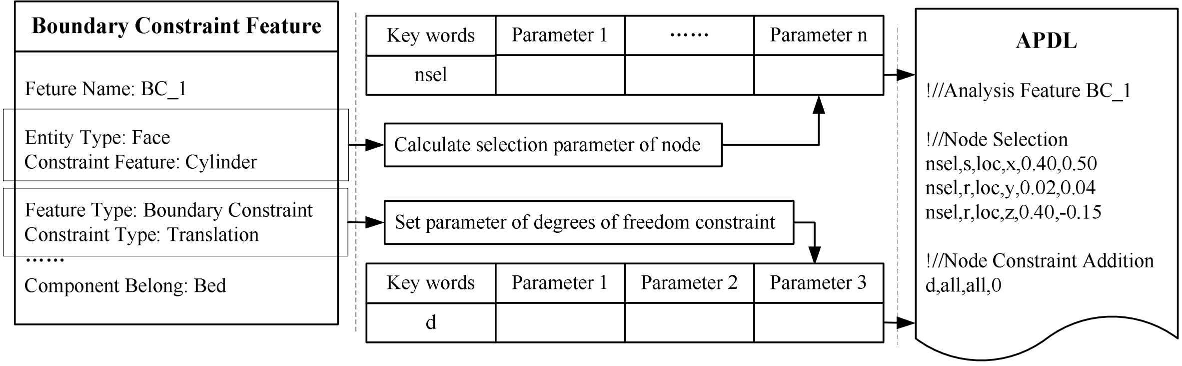

```
!//Analysis Feature BC_1

!//Node Selection
nsel,s,loc,x,0.40,0.50
nsel,r,loc,y,0.02,0.04
nsel,r,loc,z,0.40,-0.15

!//Node Constraint Addition
d,all,all,0
```

Fig.3 Mapping of boundary constraint features and APDL codes

The automatic generating process of APDL file is detailed in Fig.4. The main processes are as follows: (1) travelling the attribute information stored in CAD model and constructing the analysis feature model based on the type and specific parameters of analysis feature; (2) extracting parameters of analysis feature and determining key words and parameters of the APDL sentence related; (3) combining these APDL modules together according to the document structure of APDL file. Finally, the APDL file is generated.

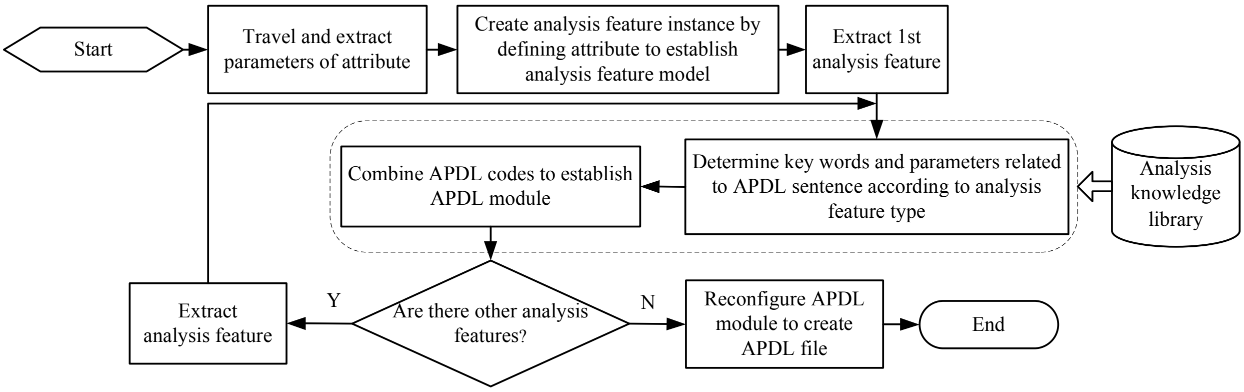

Fig.4 Generating process of APDL file

## Case Studies

A modular rapid design system of machine tool was developed, based on the methods above-mentioned, with SolidWorks and ANSYS as the development platform, by means of development tool of VB.NET. It includes parametric design module, static and dynamic analysis module for machine tool and its structural components and automatic engineering formulation of drawing module, which is embeded in SolidWorks as an add-in. For example, the processes of parametric design and FEA for one type of milling planner are as follows: (1) searching for a suitable machine tool according to the requirement of customers; (2) by means of parametric design, product model satisfied with the requirements is generated, which is shown in Fig.5(a); (3) adding analysis feature; (4) simplifying and converting the CAD model, the simplifying process is illustrated in Fig.5(b); (5) mapping analysis features to APDL codes so that APDL file can be generated; (6) running the APDL file to implement the static and dynamic analysis of the milling planner and its structural components. The results of general deformation and modal analysis of the milling planner and its bed components are shown in Fig.6. The maximum deformation of the milling planner is 78.5μm, the first order modal frequency of the milling planner is 38.4Hz; the maximum deformation of the bed is 1.55μm, the first order modal frequency of the bed is 336.7Hz.

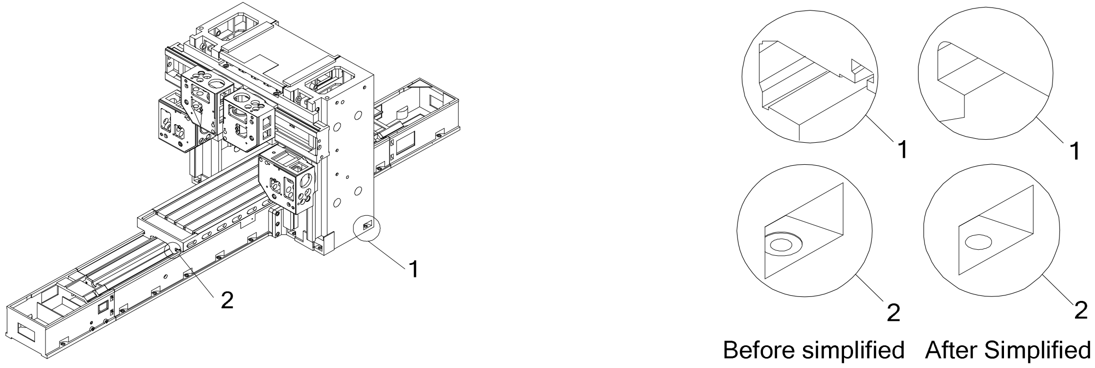

(a) (b)

Fig.5 CAD model of the milling planner and model simplification: (a) the model of milling planner (b) the process of model simplification

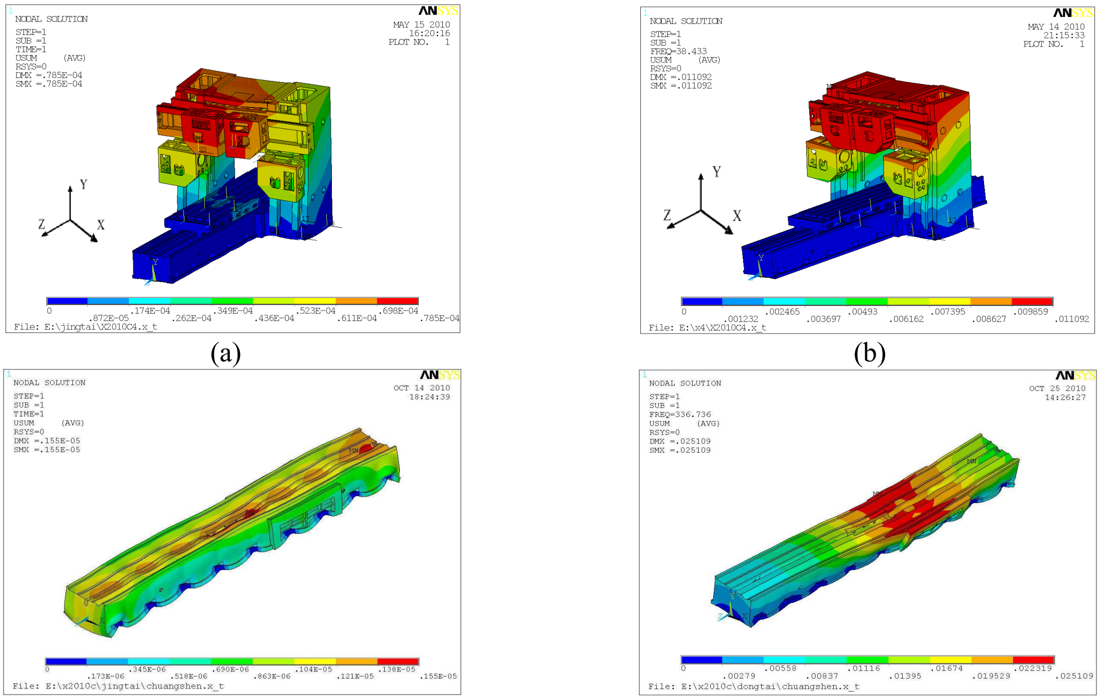

(a) (b)

(c) (d)

Fig.6 Analysis results of milling planner and its bed component: (a) general deformation of the milling planner (b) the first order modal analysis of the milling planner (c) general deformation of the bed (d) the first order modal analysis of the bed

## Conclusions

In this paper, a feature-based CAD-CAE integrated approach was proposed, which can realize rapid modeling and FEA analysis of machine tool. By adding analysis feature interactively, CAE modeling and analysis are more flexible. Furthermore, by the mapping of analysis features and APDL codes, static and dynamitic analysis of machine tool and its structural components is more knowledgeable and automatic, and the overlabored and time expended problem in the design and analysis process of machine tool is solved. Finally, the efficiency and quality of machine tool design is improved.

## Acknowledgements

The paper is supported by the state high-tech R&D programs of China -- 863 program. (No.: 2008AA042406) and the state S&T project for upmarket NC machine and fundamental manufacturing equipments of China (No.: 2009ZX04014-021, 2009ZX04001-043).

## References

[1] Libin Shen, Aimin Ji and Quansheng Huang: Machine Tool & Hydraulics Vol. 37 (2009), p. 202-205. (In Chinese).

[2] Sang Hun Lee: Computer-Aided Design Vol. 37 (2005), p.941-955.

[3] Lijuan Sun, Aihua Wang: Application Research of Computers Vol. 26 (2009), p.917-919. (In Chinese).

[4] Hong-Seok Park, Xuan-Phuong Dang: Computer-Aided Design Vol. 42 (2010), p.889-902.

[5] Xiaodong. Shao, Shen Li, Huangling Liu and Gaowen Huang: Computer Integrated Manufacturing Systems Vol. 13 (2007), p.1914-1920. (In Chinese).

*Advanced Materials Research Vols. 201-203 (2011) pp 59-62*
*© (2011) Trans Tech Publications, Switzerland*
*doi:10.4028/www.scientific.net/AMR.201-203.59*

# Using Software Engineering to Guide Commercial CAD Software Secondary Development

Cheng Wang [a], Baokun Yang[b] Xiongwei Yang[c] and Guirong Yan [d]

Key Laboratory for Strength and Vibration of Mechanical Structures, Xi'an Jiaotong University, Xi'an, China 710049

[a]wc071@163.com, [b] yang.bk@stu.xjtu.edu.cn,

[c] xiongwei@stu.xjtu.edu.cn, [d] yangr@mail.xjtu.edu.cn

**Keywords:** Commercial Software; CAD; Application Development; Software Engineer.

**Abstract.** Effective secondary development is the key process for CAD application. But as a cross-disciplinary problem and new software development mode, secondary development based on commercial CAD software has new features compared with complete independent software development. From angle of software engineering, this paper summarizes demand of software engineering, standards to observe, software development flow, configuration of development team in the process of commercial CAD software secondary development. Finally, this paper presents the case of secondary development of AutoCAD standard base parametric system to illustrate the specific application of software engineering in detail.

## Introduction

A complete CAD process includes: introduction of CAD hardware and software, secondary development of CAD software, application in product design, extension applied to CAM. Although well-known international commercial CAD software basically covers the entire manufacturing industry, they are not aimed at any specific and dedicated requirements that exist in practical and specific industry [1]. For an enterprise that needs to introduce CAD comprehensively and effetely, different levels of secondary development should be carried out according to its industry characteristics and application requirements after it digested and absorbed commercial CAD software completely.

However, main problems exist in current commercial CAD software secondary development, such as lack of unified organization and management in development process, no uniform standards or accepted norms to observe and guide, programs are often "written" according to software developers' experience.

Current research of commercial CAD software secondary development focuses on the realization technology of secondary development, such as COM [2], grid [3], object-oriented technology, database, interface [4] and parameter [5] technology. However, most of the formal researches are limited to technical details, and ignore that the entire secondary development of commercial CAD software is a new software development model and system engineering. Application the idea of software engineering to organize the process of secondary development is a new way to overcome the current problems in commercial CAD software secondary development[6].

## Application of Software Engineering

**Necessity of Application of Software Engineering into Secondary Development of Commercial CAD Software**. (1) The second development project of commercial CAD software need the staff form different divisions to collaborate and to go through several stages of development phases during the developing process. And there are close contact among various parts of software and interface problems always come about to solve with urgency. A rule is highly required to coordinate the complex relationships and problems. (2) At all stages of CAD software development process, the software being developed needs reviewing, inspecting and testing. The problems encountered in maintenance phase are also closely related to development work. And the management work of software is infiltrated into every stage of the survival cycle of the software.

Therefore, the second development project of commercial CAD software requires consistent and measurable criterion to coordinate the complex relationship. And the idea and methodology of software engineering with systemic logic will be helpful for resolving the problems resulting from different parts of software and various development phases.

**Secondary Development Process of Commercial CAD Software.** After setting purposes, development method, commercial CAD Software platform, programming language, tool, and mode of secondary development should be selected firstly. And a detailed development plan, including design objectives, design philosophy, and development process should be work out then. Detailed specific implementation technologies, such as front GUI research, back-end database and other enabling technologies should be assessed then. At last, secondary development process should follow the development process of demand research, demand analysis, system analyst and software architecture design, detailed design, programming implement, test (module test, unit test, system test) and modification according to the users' feedback. Second development process of commercial CAD software should adopt human-computer interaction and rapid prototyping law to improve the system through constant communication based on the users' feedback.

**Role Configuration of Development Team.** Secondary developers do not only understand the machinery industry expertise, but also have capabilities of software development. Therefore, the scientific development team in secondary development process of commercial CAD software should include both professional and technical personnel and software developers, shown in Table 1. However, if the secondary development project is very small, a person may play more than one roles at the same time.

Table 1: Role configuration of development team

| **Role configuration** | Job description | Professional skills required |
|---|---|---|
| Requirement analyst | With a mechanical fields of knowledge, understanding of commercial software platform | With a mechanical fields of knowledge, understanding of commercial software platform |
| System analyst and software architecture designer | Overall system design, system decomposition is determined based on the framework of the whole system to form a "system framework and module design specification" | Have knowledge not only in software but also development technology, have the capability of comprehensive analysis |
| Programmer | Turning the framework of the system and module specifications into software program with commercial CAD development tools | Familiar with the commercial CAD software secondary development tools and APIs, have experiences and skills of programming |
| Data processing editor | Mainly engaging in the data processing and data files input work | Patient |
| Software tester | Module testing, comprehensive integration testing, performance testing, stability testing, found the problem program | Extensive experience in software testing |
| Experiencing member of new system | Acceptance test, functional inspection, user simulation, experiencing feedback, consistency and integrity verification | Extensive experience in the use of commercial CAD software platform |

## Application Examples: Secondary Development of AutoCAD Standard library Parametric System

During the mechanical drawing with AutoCAD[7], part drawings and assembly drawings of assembly and standard parts with a lot of nuts, bolts, screws, gears, springs, bearings are often need to draw. These parts have the same shape in view and the only difference is the size. Therefore, establishing a scientific standard parts library system or providing development tools for standard parts development is an integral part of the CAD system.

**Design Objectives.** (1)System can output calculation results directly, generate scale drawings and output generated products map. (2)System can query design of standard accordance with the basic shape of the given parameters or models. (3)System can check design and finish calculation of non-standard bearing. (4)With database management function, system can maintain parameters of standard and all non-standard bearing.

**Design Philosophy** Only when the composition of products is built based on combination-based general components, may CAD system achieve the goal of improving the design quality of new products and shorten the design and development cycle. Based on the modular design idea, the standard library parametric system is divided into three modules: database module, main parameters design and calculation module, parametric drawing module (as shown in Fig 1).

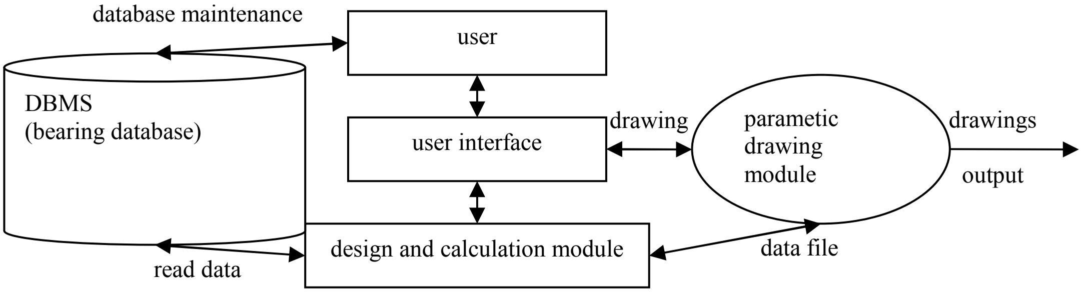

Fig. 1 Standard library parametric system module diagram

(1)Database module: These database tables store indicators related information about standard parts, types, models, geometry, performance and others in mechanical design handbook. And corresponding database maintenance is established to facilitate various operations on the database.

(2)Design calculation module: This module performs the optimization design and calculation based on parameters from the bearing database, and then selects the tolerances of corresponding size and shape, and other auxiliary parameters according to the new gained optimized parameters.

(3)Parametric drawing module: This module reads the main parameters of bearings from parameters optimization calculation module, and draws part drawings and assembly drawings using drawing development tools of AutoCAD ObjectARX.

**Process of Design.** According to basic standardization and process of rolling design, ball bearing CAD system is made up of two modules: module selection and module check, shown in Fig 2.

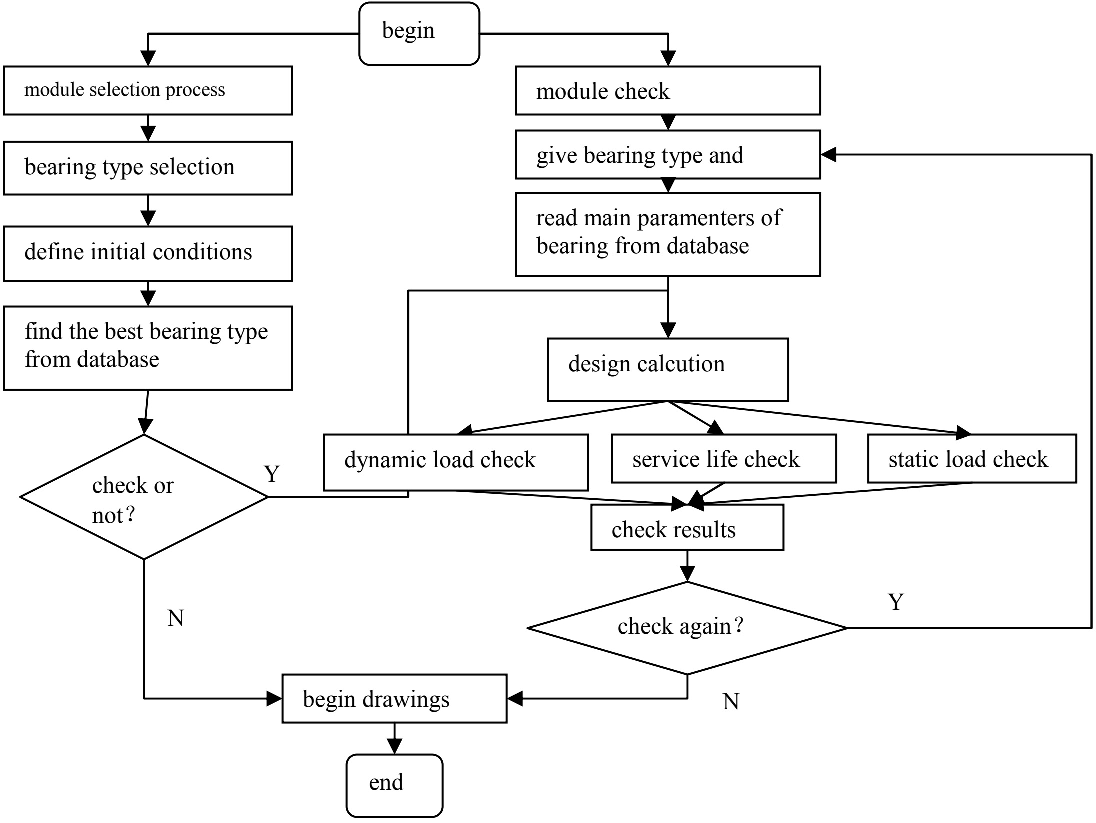

Fig.2 System architecture flow chart of ball bearing CAD system

Specific implementation technologies include: SML, GUI, database management, selection and check of rolling bearings, parametric and so on.

Using software engineering to guide secondary development process of AutoCAD standardized library parametric system will lead to targeted development, clear and reasonable staff division and standard development process. With the guide of software engineering, the planning of development processes is long-term, the role configuration of development team is clear; the collaboration is close, and the exchange is smooth. So application of software engineering into secondary development of commercial CAD software greatly improves the success rate of software development, and assures the software quality of secondary development system.

## Conclusions

Current research of secondary development of commercial CAD software focuses on realization technology of secondary development. This paper treats the entire secondary development process of commercial CAD software as a new software development model and system engineering. Secondary development based on commercial CAD software is a cross-disciplinary problem which covers the two fields of mechanical design and software development, and is of high technical complexity. Application of software engineering to commercial software secondary development can improve software quality and accelerate software development speed, reduce development costs and accelerate CAD technology application.

Moreover, the example of secondary development of AutoCAD standard library parametric system is presented to illustrate the process of secondary development with the guide of software engineering. This process can also be applied to parametric drawing and designing, information extraction off-line application form drawings, hydraulic machine design and other secondary development processes. However, as software engineering is a common and universal science, it can be used to guide secondary development processes of general commercial software platform.

## Acknowledgements

The author would like to thank his collaborators from MOE Key Laboratory for Strength and Vibration of Mechanical Structures, Xi'an Jiaotong University and the financial support of National Natural Science Foundation of China (10776026).

## References

[1] Shizhong Tong, Ping Li. Secondary development is key points of obtaining actual effect for CAD[J]. Electronic Machinery Engineering, 1999(4): 34~38 (in Chinese).

[2] Rongqiao Wang, Bo Li, Jiang Fan. Component-Oriented Distributed Part Optimization Design and Data Management System. Journal of Computer-Aided Design & Computer Graphics, 2005, 17(4):789-794 (In Chinese).

[3] Shengyou Shi, Rong Mo, Haicheng Yang, Chuanshun Zhang. Grid Service Oriented Integration of Standard Part Libraries. Journal of Computer-Aided Design & Computer Graphics, 2006, 18(4):551-555 (In Chinese).

[4] Weidong Zhao, Xianhui Liu, Gang Wei. Realization Technology of Application Development Toolkit for CAD Software. Journal of Computer-Aided Design & Computer Graphics, 2003, 15(4): 512-516 (In Chinese).

[5] Dunbing Tang, Dongbo Li, Shiqi Zhang .The Second Development for CAD Applied Software. Digital Manufacturing Industry. 1998,1(In Chinese).

[6] Aihua Cheng. Integrated Research of Scheme Design and Technical Design of Passenger Train[M]. DaLian JiaoTong University,2005, 05(In Chinese).

[7] Feng Zhang, Aiping Chen. Study of AutoCAD development envirounment. Machinery Design& Manufacture, 2005(9):125-127 (In Chinese).

*Advanced Materials Research Vols. 201-203 (2011) pp 63-68*
*© (2011) Trans Tech Publications, Switzerland*
*doi:10.4028/www.scientific.net/AMR.201-203.63*

# Research on 3D Non-destructive Measurement System Based on Homogeneous Entity

Yong Gan[1, a], Jingru Zhong[2,b], Dufen Gan[3,c]

[1,2,3]College of Mechanical & Electrical Engineering, Guilin University of Electronic Technology, Guilin 541004, China

[a]ganyong@guet.edu.cn , [b]yjw2zjr@yahoo.cn , [c]306280903@qq.com

**Keywords:** Homogeneous Entity; Digitized; 3D Non-Destructive Measurement; Profile.

**Abstract:** A new non-destructive measurement system of the homogeneous entity profiles was designed; it included the digitized minute entity cells and the delaminated measuring method for product profiles based on liquid. It is based on Archimedes' principle and lever principle and gravity moment, used optic system to collect images and calculated the verge profiles, combined the equations of the gravity moment and the equations of the center of gravity to reckon the 3D coordinate values of every minute entity cell in different layers by computer. By inputting the 3D coordinate values of the product into the related CAD software system, the 3D model could be obtained. The principles, hardware and software of the system were introduced in details about the measurement system of the homogeneous entity profiles.

## Introduction

The earliest method of reverse engineering technology was the probe measure with contact, its typical representative was called Coordinate Measuring Machine (CMM), which was mainly used in the digitization process of the entity's basic geometric shapes, suitable for measuring the external geometry of the entity. This method had high accuracy, but it was easy to fray the probe and mar the entity's surface, it needs manual intervention, and it had high cost, slow measurement speed, the use environment had exacting requirements. The 3D optical non-contact measurement method, such as raster, holography and 2D images, came forth after 1980s. The projection raster method was usually used to measure the external geometry form of the entity, its measurement range was wide, the measure precision was low, the measure velocity was fast and the cost was low, but it can not measure entity that its surface transformation is very steep. The laser trigonometry measurement method, its measure precision is high, the measure velocity was fast, but the cost was high and the surface of measured entity could not be too smooth[1]. The precision of 2D image method was low and its processing arithmetic of the measured data was very complex. The above methods had the same limitation that they could not measure the interior figure. The current existing methods in international that can measure the interior of the entity are magnetic resonance imaging and CT scanning. But both of the two methods have high cost, the size of the entity is limited, the measure precision is low, particularly the material of tested entity is limited ,they can not measure metal materials used in the engineering field. The other method of measuring the interior of the entity is Automatic CT scan technology, although the precision of the method is high, but it has slow measurement velocity, high cost and long measurement time, and the method may undermine the tested components, so the application of it has been limited[2].

With the deep development of reverse engineering technology, the research of 3D entity non-destructive measurement and reconstruction has more practical significance. The study not only for the general homogeneous entity but also some homogeneous entities with interior contour, can achieve non-destructive measurement and reconstruction. There are not successful measurement methods at home and abroad for the non-destructive measurement and reconstruction of the entities with interior contours. The paper studies the non-destructive measurement method for 3D entities with internal contour by using the Archimedes' principle, the lever principle and the gravity moment, through them they are worked out for the 3D coordinate values of the minute entity cells[3]. The method surpasses the traditional non-destructive measurement and reconstruction methods. This article describes the basic principle, hardware and software system of reverse engineering of homogeneous-entity product profiles.

## The basic measurement principle and the system constitution

**The basic principle of the measuring system.** The basic principle of the measuring system in this program is shown in fig.1. According to the Archimedes' principle, the object immersed in liquid objects upward by the buoyancy, which equals to the liquid weight discharged of. That is to say, The Buoyancy has something to do with the density and volume of the liquid discharged of by the measured entity, but not the shape of the measured entity. This measurement supposes that the measured entity is an equal density and made up of very small square cube-unit entity, the liquid-selected density is known, according to connectors principle, the measured entity will immerge into the liquid completely in initial state, small pipe of the connectors will be in downward movement driven by the precise motion platform, the liquid surface will decrease every isometric piece layer (usually adopts a small cube module entity length, that is, a small cube module entity length). The measured entity will expose the liquid level every piece layer isometric. Without considering the effect of the dampening and the surface tension and other factors, the volume of liquid discharged from each layer should be equal to the volume of the measured entity layer. The 3D entity can be dispersed into the small discrete cube assembly with the expression method of the 3D entity in the space unit. The square unit is fixed up alignment along the direction of the coordinate, if it is the real unit, its quality regards as 1 and 1 is expressed as that the square body unit is filled, the entity exists in the corresponding position of every piece layer of the measured entity, on the contrary, the empty unit expressed as 0[4]. The weight of every piece layer can be measured by the electronic scales and calculated the buoyancy changing value changed of the corresponding thin layers. Through surveying the three directions of X, Y, Z, combining parameters such as the liquid density, the torques of every thin layer, its quality and barycentre of the orderly every storey can be calculated. Changing the state of measuring, through data processing, utilize the algorithm of reconstructing to extrapolate the position of the small entity's unit in the three-dimensional coordinate system, obtain the three-dimensional information of the examined entity, and reconstruct its outline through CAD three-dimensional graphics processing software.

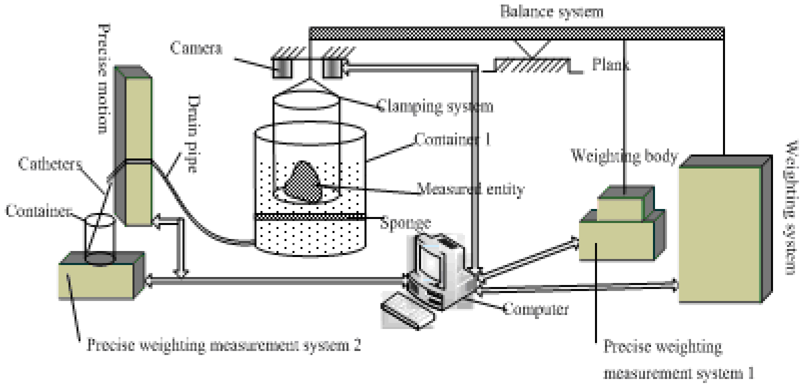

Fig.1 The sketch map of the basic principle of reverse engineering

**The composition of the measure control system and the working process.** The system constructed is a integration system that contains optical system, mechanical system, electrical system, hydraulic system, information system. It mainly includes the hardware composes of the balance system, the precise motion control system, the liquid level control system, the image acquisition system and the weight system and the software composes of the image acquisition control, the image processing and the data processing. Fig.2 shows the flow chart of the hardware system.

According to Archimedes' law, the object immersed in liquid objects upward by the buoyancy, which equals to the liquid weight discharged of, the formula as follows:

$$F_1 = G_1 = \rho_1 g V_1 \tag{1}$$

Where F1 is the buoyancy objected by the measured entity immersed in liquid, ρ1 is defined as the liquid density, V1 is the liquid volume discharged of by the measured entity immersed in liquid.

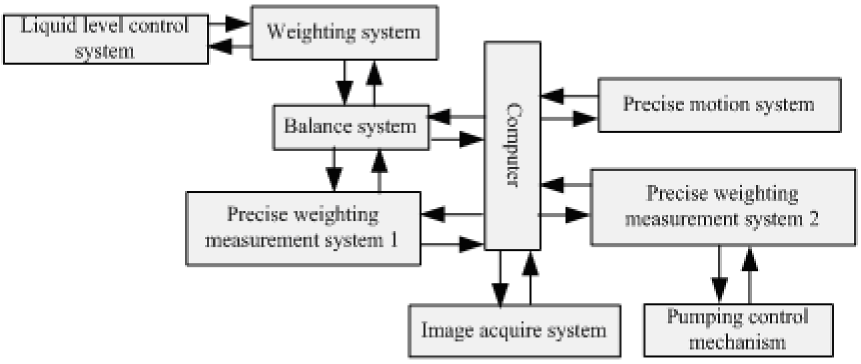

Fig.2 The flow chart of the hardware system

To achieve the measurement of the volume in each layer of the measured entity, use the precise measuring weight system 2(fig.1) directly to measure the weight of the liquid discharged of, and then calculate the volume of the liquid by Eq.1. In order to make compensation and correction for the effects of dampening and surface tension, the balance system is designed, then use the lever principle to measure the weight of the liquid discharged of and utilize the precise measuring weight system 1(fig.1) to measure the changes of buoyancy after each layer liquid discharged, and calculate the volume of the liquid discharged of, combine the precise measuring weight system 1 and 2, give the compensation and correction to the measured entity. Meanwhile, the gravity moment of each layer can be measured by building the space coordinate system and using the balance system, then the center of the gravity in each layer can be calculated. According to the volume of each layer, the quantity of the entities' unit cell can be calculated. Combine each layer's information about the gravity moment and the center of the gravity and the verge profile, the space coordinates of each unit cell can be calculated. When measuring, the measured entity will be immerged into the liquid completely, the mixed configuration liquid with color and small surface tension coefficient should be used, the balance of the balance system should be adjust through the weighting system. Meanwhile, make sure the measuring force of the measuring weight system 1 is small, the computer software will record the above results automatically. Precise motion control system guarantees the top liquid level of the drainage tube and container 1 at the same level in initial state, precise measurement weight system 2 records the initial values with the computer, the camera prepares for working. When the precise motion control system drives drainage tube down a small displacement (e.g.0.05 mm), the liquid level of container 1 descends the same distance, discharged liquid inflows to the container 2, precise measuring weight system 2 sends the weight value of the liquid discharged of to the computer, and then computer calculates the volume of this layer and records it. Meanwhile, the liquid level changes, in order to maintain the balance of the balance system, the force on the precise measuring weight system 1 will be changed, the computer records the value while balance. According to the relationship between the force and the distance on each fulcrum, we can calculate this layer's barcenter coordinate and volume. With the descend of the liquid level, when the precise measuring weight system is closing to its maximum measuring range, the system starts the injecting and pumping control mechanism respectively to balance weight, and record the various state values after balance, then repeat the measurement. In order to ensure the accuracy of measurement, the measured entity in three directions of X, Y, Z can be measured.

## The software System design

The software system includes the initialization processing system, the measurement control system, the image acquisition and processing and verge detection system, the measuring and calculating system and the three-dimensional model reconstruction system.

The initialization processing system mainly used to determine, adjust and calculate the various control parameters, then use these parameters to initialize the parameters of the software, the initialization processing system diagram shown in Fig.3. It mainly includes the drain pipe and tank level position and the balance system level adjustment, the run distance and the run times of the movement control system each time, calculate the drain interval, determine the time of image acquisition and the image acquisition parameters and sizes. The balance system level could be adjusted through the weighting system. According to the measured entity dimensions and measurement precision, each time the run distance and run times of the movement control system can be calculated. The drain interval and the time of the image acquisition can be estimated by the distance of the liquid level suck down, the size of the container 1 and the time of the liquid discharged from the drain pipe.

The times of the image acquisition equal to the times of the motion control system operates. When the distance between the camera and the measured entity increasing during the acquisition process, the images are also changing. By setting acquisition four signs to deal with the captured images, the images achieve the same size through the image scaling processing. Then it is easy to deal with the contour tracing later.

The measurement control system is mainly to ensure the system operate concordant, isometric and stability and control the image acquisition system acquire images synchronously (Fig.4). Meanwhile, to achieve the precise measurement instrument overload protection, when the system reaches set conditions, drive the weight system work, then record the values of the equipments before and after. The accuracy of the precise motion control system has great impact on the measurement results. This experiment uses the BAYSIDELM motion platform series made in America[5]. The repetitive positioning accuracy can reach $\pm 5\ \mu m$. Tilt the table a certain installation angle to achieve the precise positioning. The measurement instruments uses the Swiss Metter-Toledo AB203-S Electronic Analytical Balance 1, the maximum weighing value is 220g, the precision arrives at 0.1mg, it is directly connected to the computer through the parallel interface and used to measure the changing force in the system.

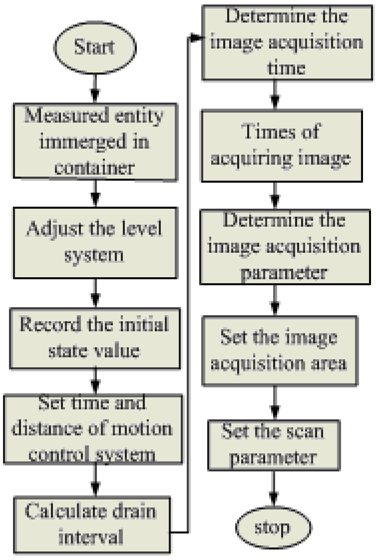

Fig.3 The flow chart of the initialization processing system

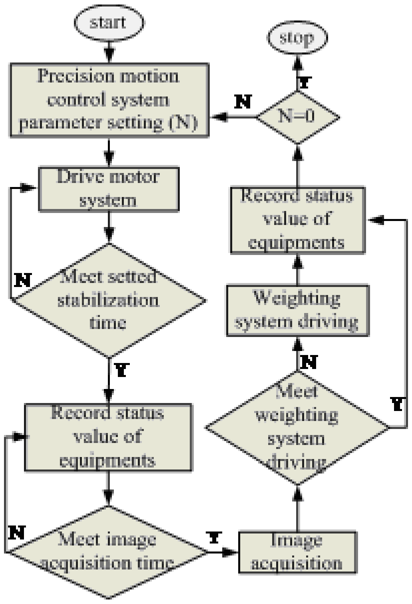

Fig.4 The flow chart of the measurement control system

The image acquisition system is mainly used to control the image real-time and accurate acquisition coordinates all aspects of the computer, shown in Fig.5. During the measurement processing, the camera is arranged with a certain angle, the liquid color is black. The acquisition images are calibrated through the image scaling, so as to facilitate the calculation of every unit cell. The acquisition image does not require higher precision.

The verge extraction processing and the measurement calculation system are used for the calculation of the position of the entities' cells in spatial coordinates, that is, calculating all the spatial coordinates of the tested entities. The verge extraction processing system is to simplify the measuring and calculating system, the part calculation of the unit cells can be estimated by the verge extraction processing. The measurement calculating system combines the equations and the center of gravity coordinates equation of the every layer, the associated nature of the measured entity between two layers, and all the minute entity cells only can be regarded as 0 or 1. Through intelligent calculation, we can get the coordinate values of the minute entity cells in space coordination.

Because the measurement system and the software system above have got all the coordinates of the points of the measured entities' cells and processed the corresponding error points, the point cloud figure of the measured entities have been completed. Three-dimensional model reconstruction system only should analyze the point cloud data and reconstruct models from point to line, from line to plane. The usual commercial CAD software can be used as the reconstruction software of the measurement system.

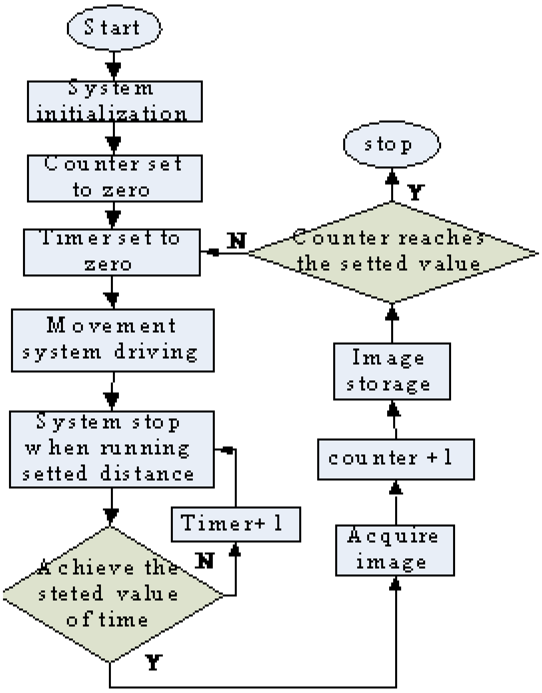

Fig.5 the flow chart of the image acquisition system

## Conclusions

To demonstrate the accuracy and the feasibility of the measurement method and the measurement system designed, take the thickness of 1mm measured entity as a example. The contour of the measured entity can be reconstructed and amended through the point cloud of the center coordinates of each entity cell and the images of very layer maps. During the measurement processing, in order to ensure the boundary accuracy of the subdivided cells and improve the reconstruction accuracy, when calculate the number of the entity's cells, if a cell's volume is smaller than a whole cell but larger than its 1/2, then recorded as a whole cell; if it is smaller than its 1/2, then give it up. Take the length of 1mm cell, the reconstruction accuracy of the measured entity is 0.5mm. Due to the effect of the mechanical friction, the fluid stability, the environmental temperature and other effect, the measurement time of the length of 50mm × 50mm × 50mm entity is about 3 hours. The experimental system costs less than ￥50,000. To further reduce the impact of the above factors, the sensors and the mechanical property can be further improved, through theoretical analysis and the preliminary measurements of the complicated entity, the reconstruction accuracy is expected to reach 0.1mm, and the three-dimensional entity with some through-hole internal contour can be measured.

## Acknowledgements

This work was financially supported by the National Natural Science Foundation (50965005) and Scientific Research Project of Guangxi Education office (200911MS81).

## References

[1] Jin Tao, Chen Jianliang, Tong Shuiguang, reverse engineering research[J]. China Mechanical Engineering, 2002, 13(16): 1430~1436. In china.

[2] Sang Xinzhu, LV Naiguang, Three-dimensional shape measurement method and its development trend[J]. Beijing Institute of Machinery Industry Journal, Vol16，No.2，2001.6:32～36. In china.

[3] Sun Ning, A 3D contour measurement of the equipment and methods[P]. China, applications for invention patents statements 03108989.5, 2003.9.16. In china.

[4] Gan Yong, Sun Ning, Kong Qinghua, Buoyancy-based non-destructive measurement of 3D entity experiment system research[J], Shanghai Mechanical and Electrical Integration, 2007.1:28~30. In china.

[5] BAYSIDE precision positioning platform[Z]. Beijing Yuan Mao control equipment technology companies with limited liability.

*Advanced Materials Research Vols. 201-203 (2011) pp 69-74*
*© (2011) Trans Tech Publications, Switzerland*
*doi:10.4028/www.scientific.net/AMR.201-203.69*

# Study on the Parallel Rendering Technology used in Virtual Prototype System

Mingqiang Yin [1,a], Shiqi Li [2,b]

[1,2]School of Mechanical Science & Engineering, Huazhong University of Science & Technology,
Wuhan 430074, China

[a]yeml@163.com, [b]sqli@mail.hust.edu.cn

**Keywords:** Virtual Prototype; Parallel Rendering; PC Cluster; Model Transformation; Huge Dataset.

**Abstract.** With continuous expansion of manufacturing scale, the scene data that virtual prototype system has to deal with is far beyond a single computer's processing power. To meet the requirements of large-scale simulation, this study designs a virtual prototype system based on PC cluster. The problems including software architecture of virtual prototype system, transformation of CAD model, scene graph management, real-time rendering of huge dataset, and so on are investigated in detail in this paper. Finally a prototype system has been implemented. The system is constructed by PC cluster and gigabit LAN. The aim of the system is to build a large-scale, high resolution, immersive virtual environment supporting users' virtual design and manufacture.

## Introduction

Virtual Prototype is a technology that uses computer models to do some experiments instead of real physical prototype. It is a computer-aided engineering, which developed rapidly with the development of computer technology in 1980s [1]. The purpose of virtual prototype is to verify designing, to assist product selection, to test manufacturing and to display products ahead of time in digital method [2]. Finally, it may replace the role of physical prototypes. Virtual prototype can significantly shorten the product design and manufacturing cycles, reduce the costs of product development and improve product design quality.

With the further promotion and application of the virtual prototype technology, simulation scene has extended from the small and simple object to the large-scale and complex product [3]. Due to increasing 3D scene data, the data need to be dealt with is far beyond the power of a single computer. Image generation speed becomes a bottleneck of real-time simulating. Apparently, advanced hardware is helpful to solve the problem of large scene rendering. It should be noted that there are conflicts between infinite data and limited processing power that current hardware has. So it requires the virtual prototype system to use a variety of new technologies to solve this problem.

In this paper, we describe a virtual prototype system based on parallel computing, and then give the architecture of this virtual prototype system. At last we show some techniques used in the system, such as CAD model transformation, mesh model segmentation, parallel rendering based on PC-cluster. With high performance 3D graphics card and high-speed gigabit Ethernet, we developed a prototype system based on parallel computing.

## Related work

It's relatively simple to realize the single-PC-based virtual prototype system, which has been extensively studied at home and abroad. With the quality of 3D scene data increasing, if not decrease the graph quality and complexity of 3D scene, parallel computing under cluster can be the only way to solve the problems in virtual prototype system.

Parallel computing in large-scene rendering has been extensively studied at home and abroad. Some general concepts applicable to cluster parallel rendering have been presented in[4-5] (sort-first architecture). Some generic APIs parallel rendering systems exist which include VR Juggler[6](and its derivatives), Chromium[7], OpenGL Multi-pipe SDK[8] and Equalizer[9]. VR

Juggler is a graphics framework for virtual reality applications which shield the application developer from the underlying hardware architecture, devices and operating system. Chromium provides a powerful and transparent abstraction of the OpenGL API, which allows a flexible configuration of display resources. OpenGL Multi-pipe SDK (MPK) implements an effective parallel rendering API for a shared memory multi-CPU/GPU system. The Equalizer parallel rendering framework differs in that it supports a fully distributed parallel rendering paradigm and features an extremely flexible task decomposition approach.

However, the targets for these approaches above are different for ours. Instead of parallel rendering only, we should like to devise a more scalable and affordable approach to support large-size scene simulation in virtual prototype system.

## Architecture of virtual prototype system

The main features of the system are as follows:

Parallel and distributed computing: This virtual prototype system using the C/S architecture, all modules can be run on the remote server. It provides high-performance parallel numerical libraries, parallel program debugging, trace, and performance analysis tools. All the compute-intensive modules are implemented in parallel computing. MPI (message passing interface) is used as a basic interface for parallel communication.

Scalability: The system only implements the core modules and data management, and all other specific modules can interact with the core modules through TCP/IP dynamically. Problems could be solved collaboratively. All modules can be executed stand-along. In the system four communication methods are supported, including shared memory, pipes, socket and documents. According to the location of module running, the amount of data to be exchanged and the feature of the problem, the system can choose different methods to communicate between different modules.

Wealth of computing technology support: According to current needs, our system has implemented some function modules such as geometric modelings, geometry repairing, mesh model generation, mesh model segmentation, scientific data visualization and remote job submission, task submission, resource management and so on.

Visualized manipulation: The virtual prototype system provides a friendly graphic interface, all the modules provide graphic interface. Users can control the whole process of calculation interactively. The calculation or manipulation result can be rendered by parallel rendering and displayed in 3D display-wall.

Cross-platform: The core and main modules of the system can run on the most common operating system such as Linux (IA32/IA64), Windows, Unix family platforms (SGI Irix, IBM AIX, etc.); It should support all major hardware platforms, such as shared memory architecture SMP and distributed memory architecture MPP, cluster and so on. Figure 1 shows the architecture of virtual prototype system.

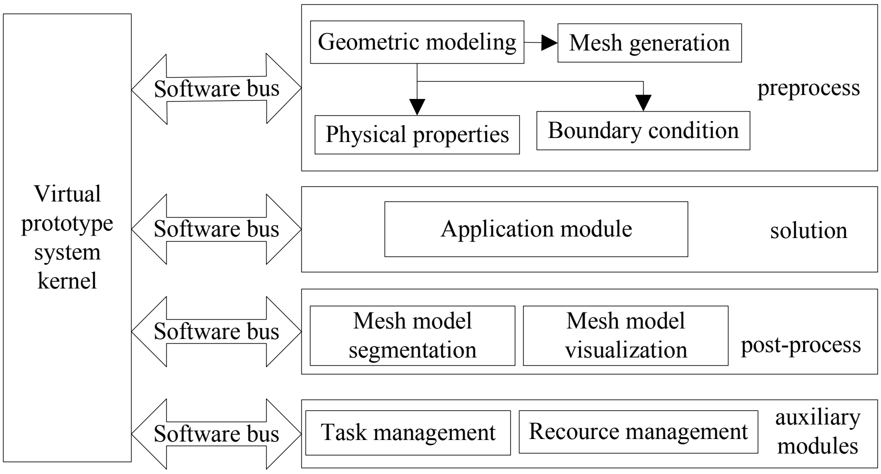

Fig. 1 Software architecture of high virtual prototype system

## Important technologies in the system

### 4.1CAD model transformation

Virtual prototype system uses triangle or polygon to represent product, whereas CAD systems use accuracy math method such as B-Rep and CSG to represent product. Therefore it is necessary to transform data information from CAD model to mesh model. Because most of CAD systems could save the product information as STEP (Standard for the Exchange of Product model data) format. Therefore, we could realize the data transformation from STEP format. A method based on STEP neutral file is proposed in this paper.

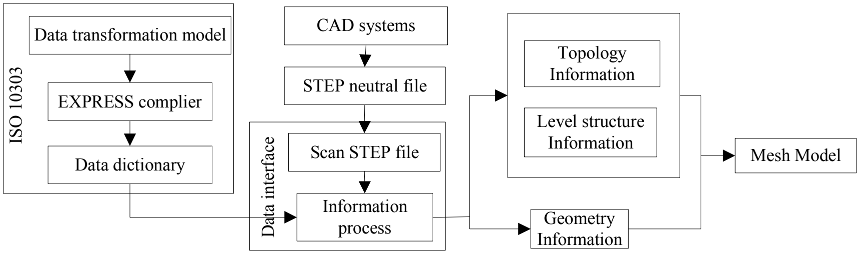

Fig. 2 CAD model transformation flowchart

The transformation flowchart is shown in Figure 2. First, we build the product model in any CAD systems, and export it with STEP format. Then we analyze the file with data interface which includes file scanning and information translation two parts. The data interface is constructed based on the ISO 10303. And the data dictionary is produced based on the analysis of the definition of entities which are defined with EXPRESS language. At last we get the geometry information, hierarchical structure information, and useful information which are necessary in simulation environment.

### 4.2 Mesh Model Segmentation

In parallel rendering module, if the size of the geometric model is so large, that it will cross several screen areas. The model will be rendered repeatedly in differently rendering nodes. Therefore, these large models will cause serious loss of efficiency. In order to solve this problem, we need to pre-segment the model and divide the whole model containing large facets into several sub-models which contains smaller facets. With the help of frustum cutting, only the sub-model within corresponding screen could be rendered. Thus the number of facets been rendered repeatedly could be reduced. The detail algorithm flow is shown in figure 3.

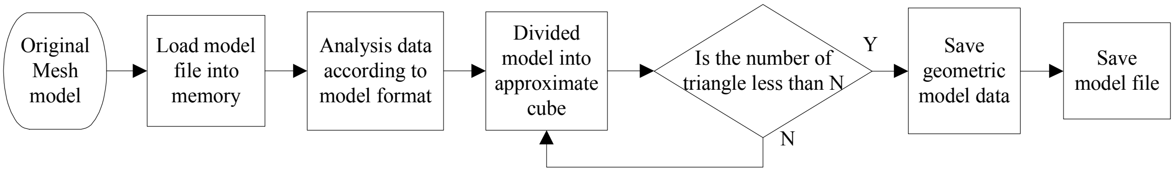

Fig. 3 Flow of mesh model segmentation

### 4.3 Scene graph management

This virtual prototype system runs in retained model. User node and compute nodes within the system store the entire 3D mesh model. These mesh models can be organized as a scene tree. The scene tree is also stored in distributing compute nodes. In logic, these scene trees can be looked as global scene tree. Any change in the global scene tree should be broadcast to all nodes in the system real-time to ensure the consistency of the rendering result. Global scene tree management focused on model loading, distributing information of the models, updating of the scene tree properties and deleting nodes of scene tree, etc.. In this system, all the model loading function is executed in every parallel computing node in the system, and it saves filename and pointer of the model in the global model library, and then takes a global identification for the mesh model. According to the identification, the address of model in the memory could be found out.

After system initializing, user node will broadcast information of models being loaded to all rendering nodes, then a copy of global model library will be generated according to the information received in every rendering node. With the global model library, mesh model can be loaded dynamically. During process of simulating, user nodes collect information of scene tree in every frame, and send the information to other nodes, so as to keep content consistency of the scene tree property. Adding or deleting a mesh model in any parallel computing node will be broadcast to the other nodes, and the structure of global scene tree will be updated.

## 4.4 Parallel rendering

### 4.4.1 Architecture of parallel rendering

Figure 4 illustrates the principle of parallel rendering. The parallel rendering architecture is based on a master-slave model. It has an event loop which redraws the scene; update data based on received events, and eventually redraw a new frame. The master is responsible for managing the visualization system. It controls and launches the application's rendering clients. The render client implements the rendering part of an application. Its execution is passive. It has no main loop and is completely driven by the master. It executes the tasks received from the server by calling the appropriate task methods in the correct thread and context. The application either implements with application-specific code.

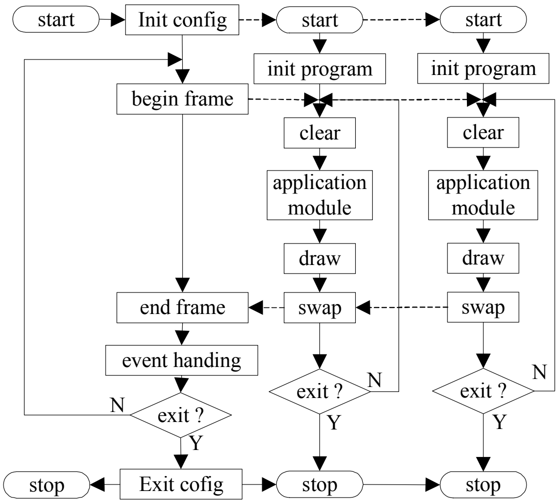

Fig. 4 Architecture of parallel rendeing

### 4.4.2 Load balance

Load balancing is important for parallel rendering. In generally, the smaller the task is divided, the easier the system is to obtain load balancing. However, too smaller task dividing will bring huge information communicating. Therefore, for a parallel computing system, we must make a choice between task dividing and amount of communication data.

With respect to the principle of load balance, there are two methods in frustum division. The first one is to divide frustum statically. It means that when the program starts, dividing strategies and methods have been determined, and no longer changed during program execution. This algorithm is simple, and can reach a certain balance effect. In our system, we divide frustum dynamically. Our algorithm compares the number of triangular in each rendering node, and then take load balancing algorithm for the task dividing, to make sure that the task of each rendering node is relatively equal ,and the performance of the system is better. Thus, the system could avoid the problem that a large number of geometric data be processed on a certain rendering node.

### 4.4.3 Off-screen rendering

Our virtual prototype system is based on parallel rendering. If we adopt the traditional CPU rendering pipeline without modification, there will be some problems. Firstly, each rendering node must render online, which means rendered image must be displayed, and can not be covered. Due to the reason of the operating system, the covered part may not be updated. Secondly, MPI process in slave can not be started in standard windows service mode. So in this MPI environment, the started windows programs will not appear on the screen. We use the latest OpenGL extension technology. It provides off-screen rendering function. In 2005, the OpenGL added a new expansion GL_EXT_framebuffer_object. Using this extension, you can create a Frame Buffer Object (FBO) and Render Buffer Object (RBO). This technical performance is greatly improved compared with the original PBuffer. Through this extension, we achieve off-screen rendering. If we simply use

FBO objects for off-screen rendering, the rendering process will not support anti-aliasing function, and the serrated phenomenon on the edge of rendering image will be serious. In order to achieve high-quality rendering of FBO, in 2007, OpenGL added two new extensions, GL_EXT_framebuffer_multisample and GL_EXT_framebuffer_blit. By using these two extensions, we can achieve smooth edges.

## Experiment result and analysis

We have tested the virtual prototype system on a cluster composed of 5 computers. All computers are connected by gigabit LAN, and each computer is equipped with one core2 CPU, 2G DDR1 system memory and one graphic card of NVIDIA GeForce 7900 GS.

### 5.1 Communication Proficiency Test

This test is carried out between two nodes to test the transmission speed. We send the amount of data ranging from 100 Byte~5×106 Byte in one time. Result shows that the maximum transmission capacity is about 900Mb/s. Consider that we use resolution 1024×768, then each frame size will be 1024 × 768×3=2 359 296Byte. Suppose that the efficiency of network transmission is 83%, and the transmission capacity will be about 740MB/s , and it will take 26ms to transmit on frame data.

### 5.2 Analysis of parallel rendering

In this test, we use one computer as user node and other 4 computers as render nodes. Each render node works as a projection channel and outputs frame images separately. All the system works as a sort-first rendering cluster. Projection channels setup their view frustum as their corresponding display portals and perform frustum clipping. Figure 5 shows the displayed image on the screen, and figure 6 shows the performances of the cluster comparing with single workstation. Figure 6 indicates that with lower triangle number, time consumed by rendering nodes swap-sync can’t be neglected so that clusters run at a speed lower than single workstation; but as triangle number increased, swap-sync latency become negligible and the clusters become more efficient than single workstation. The speedup doesn’t increase linearly, which is due to the subsistent latencies and the load imbalance of sort-first rendering structure.

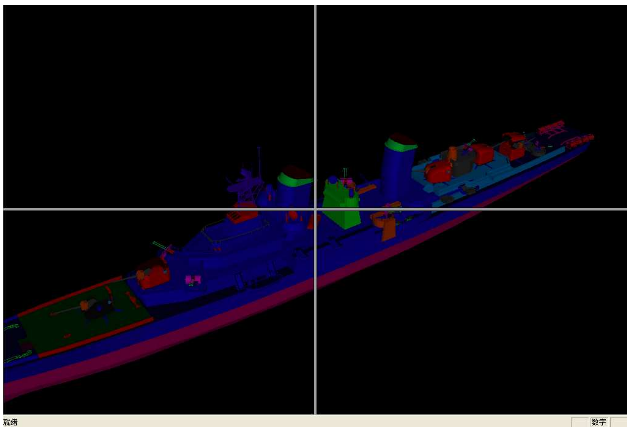

Fig.5 Sample image of virtual prototype system

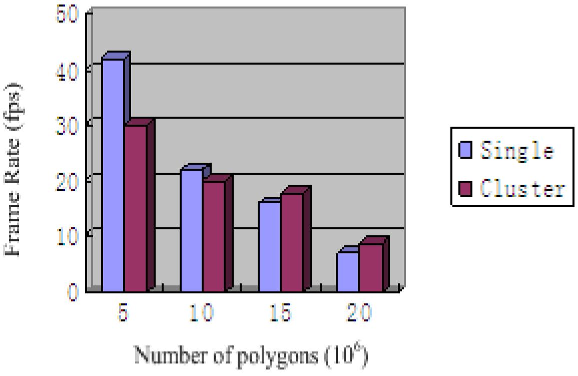

Fig.6 Rendering performance diagram

## Conclusions

Virtual prototype is a comprehensive technology. It has been used to achieve optimal design and manufacturing. With the expansion of manufacturing, the object is simulated from simple scene to massive complex one. This paper presented a parallel computing method for interactive rendering of massive complex scene on PCs cluster. The proposed method include: CAD model transformation, mesh model segmentation, management of mesh model, and parallel rendering. CAD model transformation implements conversion method from CAD system to integrated virtual simulation environment. Mesh model segmentation cut the mesh model into smaller one to avoid rendering repeat. Scene graph management ensures the consistency of the scene tree in every calculating node of the system. Parallel rendering performs the drawing of the whole scene. Experimental results have shown that our prototype system can achieve good performance for rendering massive complex scenes.

## Acknowledgements

This research work has been partially supported by National High-tech Research & Development Program of China under Grant NO.2005AA804022.

## References

[1] Yan, X. and Gu, P. (1996). A review of rapid prototyping technologies and systems, Computer Aided Design, 28(4), 307318

[2] Alik, S.M., Lin, J., and Goldenberg, A.A., "Virtual prototyping for conceptual design of a tracked mobile robot", Canadian Conference on Electrical and Computer Engineering, Ottawa, Ontario, Canada, May 2006.

[3] Malik, S.M., "Virtual prototyping for conceptual design of tracked mobile robots," M.S. thesis, Dept. Mech. and Indust. Eng., Univ. of Toronto, Ontario, Canada, 2006.

[4] MUELLER, C. 1995. The sort-frst rendering architecture for highperformance graphics. In Proceedings Symposium on Interactive 3D Graphics, 75–84.

[5] MUELLER, C. 1997. Hierarchical graphics databases in sort-first. In Proceedings IEEE Symposium on Parallel Rendering, Computer Society Press, 49–60.

[6] BIERBAUM, A., JUST, C., HARTLING, P., MEINERT, K., BAKER, A., AND CRUZ-NEIRA, C. 2001. VR Juggler: A virtual platform for virtual reality application development. In Proceedings IEEE Virtual Reality, 89–96.

[7] HUMPHREYS, G., HOUSTON, M., NG, R., FRANK, R., AHERN, S., KIRCHNER, P. D., AND KLOSOWSKI, J. T. 2002. Chromium: A stream-processing framework for interactive rendering on clusters. ACM Transactions on Graphics 21, 3, 693–702.

[8] HUMPHREYS, G., ELDRIDGE, M., BUCK, I., STOLL, G., EVERETT, M., AND HANRAHAN, P. 2001. WireGL: A scalable graphics system for clusters. In Proceedings ACM SIGGRAPH, ACM Press, 129–140.

[9] EILEMANN, S., MAKHINYA, M., AND PAJAROLA, R. 2008. Equalizer: A scalable parallel rendering framework. IEEE Transactions on Visualization and Computer Graphics, VOL. 15, NO. 3, MAY/JUNE 2009.

*Advanced Materials Research Vols. 201-203 (2011) pp 75-79*
*© (2011) Trans Tech Publications, Switzerland*
*doi:10.4028/www.scientific.net/AMR.201-203.75*

# Models and Simulations of the UV lithography Process Based on Thick Photoresists

Zaifa Zhou [a], Qing'an Huang [b] and Weihua Li [c]

Key Laboratory of MEMS of the Ministry of Education, Southeast University, Nanjing 210096, China

[a] zfzhou@seu.edu.cn, [b] hqa@seu.edu.cn, [c] liwh@seu.edu.cn

**Keywords:** Thick Photoresist; Lithography Simulation; Diffraction; Light Distribution; MEMS

**Abstract:** This paper presents the models for the ultraviolet (UV) lithography of thick photoresists such as thick SU-8. Simulations for various lithography conditions have been conducted using these models based on the improved dynamical cellular automata method. Some experiments on SU-8 2075 layers under UV source with 365nm wavelength have been implemented to verify the simulation results. The results confirm the validity of the proposed models.

## Introduction

Ultraviolet (UV) lithography of thick photoresists such as SU-8 photoresists is increasingly adopted to manufacture novel and complex high aspect-ratio Micro-Electro-Mechanical Systems (MEMS) elements [1-3], since relatively simple and inexpensive lithography equipments are utilized compared to X-ray or laser systems. The UV lithography process of the SU-8 consists of several steps. The SU-8 is firstly spin coated onto a substrate and soft baked to evaporate the solvent. Then the SU-8 is exposed to the UV light, the photoacid generator (PAG) decomposes and generates photoacid within the SU-8. During the subsequent post-exposure bake (PEB) process, the photoacid catalyzes the reaction between the resin and the cross-linking agent to afford a highly cross-linked polymer network which is significantly less soluble than the polymer resin without cross-linking reaction. At last, the unexposed SU-8 is dissolved by an organic solvent, leaving only the cross-linked SU-8 microstructures on the substrate. Many factors affect the final development profiles of the SU-8. It is not practical to determine the best fabrication parameters for the UV lithography process of thick SU-8 using the traditional repeated experiment method. Simulation is acknowledged to be efficient for predicting and optimizing the lithography process.

In this paper, the models for the UV lithography of thick photoresists such as thick SU-8 are presented. A series of simulations for various lithography conditions have been conducted using these models, based on the improved dynamical cellular automata method [4]. Some experiments on SU-8 2075 layers under UV source with 365nm wavelength have been implemented to verify the simulation results. The results confirm the validity of the proposed models.

## Simulation models

Ideal contact exposure without any gap between the mask and the SU-8 is not practical for inevitable errors such as surface flatness, surface roughness, etc.. Air gaps from 10μm to over 100μm are very common for UV lithography process of thick SU-8. The thicker the SU-8 layer is, the larger the gap may be. Because of the high viscosity of the SU-8, it is difficult to obtain uniform spin-coat. For thick SU-8 layer, the UV light diffraction effect of the mask pattern will lead to severe profile distortions. To reduce the diffraction effects, different index matching materials such as water and glycerol have been adopted as index matching materials to fill the air gap [3, 5].

To simulate the light intensity distributions for the UV lithography of thick SU-8 with index matching materials, we define some parameters associated with the calculations of the UV light intensity distribution. $n_1$, $n_2$, $n_3$ and $n_4$ are defined as the refractive indices of air, index matching materials, SU-8 photoresists and wafer, respectively. $\lambda_1$, $\lambda_2$, $\lambda_3$ and $\lambda_4$ stand for the UV light wavelength in air, index matching materials, SU-8 photoresists and wafer, respectively. $R_1, R_2$ and $R_3$ are the reflection coefficients at air/index matching materials, index matching materials/SU-8 and SU-8/substrate interfaces, defined by $R_1 = ((n_2 - n_1)/(n_2 + n_1))^2$ , $R_2 = ((n_3 - n_2)/(n_3 + n_2))^2$ and $R_3 = ((n_4 - n_3)/(n_4 + n_3))^2$, respectively.

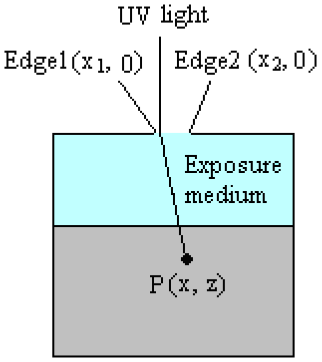

Fig. 1 Schematic of the UV light transmission in a single long slit

For the UV light from S reaching P through a hole, as shown in Fig.1, the Fresnel-Kirchhoff diffraction integral formula has the following form utilizing paraxial approximation technique [5]

$$U_P = -\frac{iA}{2(r+s)} e^{ik(r+s)} \{[c(u_2) - c(u_1)] + i[s(u_2) - s(u_1)]\} \cdot (1+i) \tag{1}$$

where A is the incident light wave amplitude. r and s stand for the distances of a point on the aperture relative to the observation point and the source, respectively. $k = 2\pi/\lambda$ is the incident wave number, where $\lambda$ is the wavelength of incident UV light in the exposure medium. $c(u) = \int_0^u \cos(\pi y^2/2)dy$ and $s(u) = \int_0^u \sin(\pi y^2/2)dy$ are the Fresnel integrals, where $u$ ($u_1$ and $u_2$) is the Fresnel number written as

$$u_i^2 = \frac{2}{\lambda z}(x_i - x)^2, \quad i = 1, 2 \tag{2}$$

where $z$ is the vertical distance from the mask plane to the calculation point in the SU-8, $x_1$ and $x_2$ represent the horizontal coordinates of the left and right edges of the mask, respectively.

Thus the light intensity distribution equation considering the reflection at the air/index matching materials and index matching materials/SU-8 interfaces can be expressed as

$$I_p = U_P^* \times U_P = |U_P|^2 = \frac{(1-R_1)(1-R_2)I_{lamp}}{2}\{[c(u_2) - c(u_1)]^2 + [s(u_2) - s(u_1)]^2\} \tag{3}$$

where $I_{lamp}$ is the original intensity of the UV light from the UV source .

During the propagation of the incident UV light, the UV light will be refracted on the index matching materials/SU-8 interface. When the UV light transmits into the SU-8 from the index matching materials, the wavelength, phase, and other relevant information will be changed. The effect of light refraction effect on the final development profiles can not be neglected for soft contact lithography because of the gap between the mask and the SU-8, as shown in Fig.2. However, it is difficult to deal with this refraction in Fresnel integral equation, so the refraction effect has not been considered in current SU-8 UV lithography simulation. This paper presents a method to incorporate the refraction effect into the Fresnel diffraction integral for the UV lithography processes of the SU-8 in two steps.

Fig.2 shows the UV refraction modeling at the index matching materials/SU-8 interface. Firstly, $p_1$ represents the gap thickness between the mask and the SU-8. Secondly, the mask plane is vertically shifted in such a way that the same field distribution results at the interface between the index matching materials and the SU-8. The gap between the mask and the SU-8 is assumed to be homogeneously filled with SU-8, and the propagation of the field inside the original SU-8 is now treated as if there were no step in the refraction index behind the mask. In this way, diffraction and refraction effects can be handled simultaneously. $p_2$ represents the gap thickness after shifting the mask.

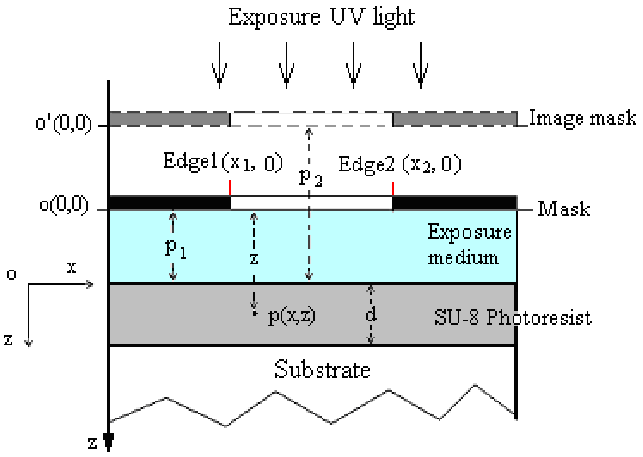

Fig. 2 The aerial image modeling for the UV lithography of the SU-8

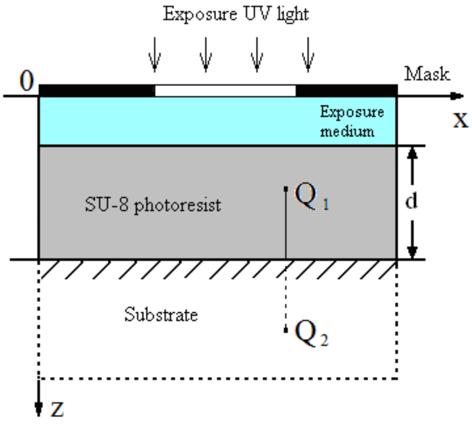

Fig. 3 Schematic of the UV reflection at the SU-8/substrate interface

Before shifting the mask, for the observation point P(x, z) at the index matching materials/SU-8 interface, the scalar field is

$$U_P(x,z) = B'\{[c(u_2') - c(u_1')] + i[s(u_2') - s(u_1')]\} \cdot (1+i) \tag{4}$$

where $B' = -\frac{iA}{2(r+s)} e^{ik_1(r+s)}$, and the Fresnel number $u_i' = \sqrt{\frac{2}{\lambda_2 p_1}}(x_i - x), i = 1,2$. $k_1$ stands for the wave number in the index matching materials.

After shifting the mask, for the same observation point, the scalar field is

$$U_P(x,z) = B''\{[c(u_2'') - c(u_1'')] + i[s(u_2'') - s(u_1'')]\} \cdot (1+i) \tag{5}$$

where $B'' = -\frac{iA}{2(r+s)} e^{ik_2(r+s)}$, and the Fresnel number $u_i'' = \sqrt{\frac{2}{\lambda_3(z - p_1 + p_2)}}(x_i - x), i = 1,2$. $k_2$ stands for the wave number in the SU-8.

For $r << s$ during the UV lithography process of SU-8, the modulus of $B'$ is approximate to $B''$. When computing the intensity of the UV light, we only need the modulus of $B'$ and $B''$. In order to insure that the field distribution at the index matching materials/SU-8 interface after shifting the mask is the same as the original one, $u_i'$ should be equate to $u_i''$. So we can obtain $p_2 = p_1 \cdot n_3 / n_2$. Therefore, the propagation of the light field inside original SU-8 can be treated as if there were no step in the refraction index behind the mask

$$I'_p = \frac{(1-R_1)(1-R_2)I_{lamp}}{2}\{[c(u'_2) - c(u'_1)]^2 + [s(u'_2) - s(u'_1)]^2\} \tag{6}$$

$$u'^2_i = \frac{2(n_3/n_2)}{\lambda_3(z - p_1 + p_2)}(x_i - x)^2, \quad i = 1,2 \tag{7}$$

Generally, the incident UV light will be reflected by the SU-8/substrate interface, and the reflected UV light will pass through the SU-8. Thus besides the diffraction and refraction effects, it is important to incorporate the effects from the reflected UV light on the light intensity distribution into the SU-8. To understand the reflection effect, we mirror the SU-8 at the SU-8/substrate interface. As shown in Fig.3, the reflected intensity at point $Q_1$ can be calculated out by the Fresnel reflectance at the SU-8/substrate interface and the incident intensity at point $Q_2$ (the symmetric point of $Q_1$).

Based on above analysis, the final equation with diffraction, refraction and reflection effects for the intensity distribution pattern calculation at point p, can be finally expressed as

$$I''_P = \frac{(1-R_1)(1-R_2)I_{lamp}}{2}\{\{[c(u'_2)-c(u'_1)]^2+[s(u'_2)-s(u'_1)]^2\}+R_3\{[c(u'_4)-c(u'_3)]^2+[s(u'_4)-s(u'_3)]^2\}\} \quad (8)$$

$$u'^2_i = \frac{2(n_3/n_2)}{\lambda_3(z-p_1+p_2)}(x_i-x)^2, \qquad i=1,2 \quad (9)$$

$$u'^2_i = \frac{2(n_3/n_2)}{\lambda_3(2d+p_1-z+p_2)}(x_i-x)^2, \qquad i=3,4 \quad (10)$$

where $d$ represents the thickness of the SU-8 layer.

After the light intensity distribution into the SU-8 is obtained using aerial image simulation, the exposure simulation model is used to express the exposure kinetics in the SU-8. Now the problem is that the *Dill* model [6] originally developed for thin photoresist lithography is insufficient to describe the nonlinear effects in the thick SU-8 layers. Unlike the thin photoresists, the nonlinear effects in the thick photoresists, such as the concentration distribution of photoresist components, will significantly affect the exposure processes. To solve the problem, an improved *Dill* model [4] is developed to describe the exposure kinetics in thick SU-8 exposure processes.

During the PEB process, the photoacid induces chemical reactions in the SU-8, resulting in cross-linking of epoxy resin. Since the photoacid concentration is not uniform in the SU-8, there is a photoacid diffusion process while the catalytic conversion is undergoing. The chemical reactions and diffusion of species happen simultaneously and couple with each other. The coupled reaction-diffusion kinetics [7] can be employed to describe the PEB process for the SU-8.

For the development process simulation, the *Notch* model [8] is employed to describe the relationship between the etching rate and cross-linked site concentration. Furthermore, the photoresist etching rate will be significantly increased, because agitation methods are usually adopted for high aspect ratio and/or thick film microstructures during the development processes. Since the etching processes of the SU-8 are depth dependent, and the swelling effect will significantly affect the development profiles of the SU-8. The above *Notch* model, however, should be modified to incorporate the depth-dependent dissolution rate effect, and the swelling model should be adopted to obtain the final development profiles [4].

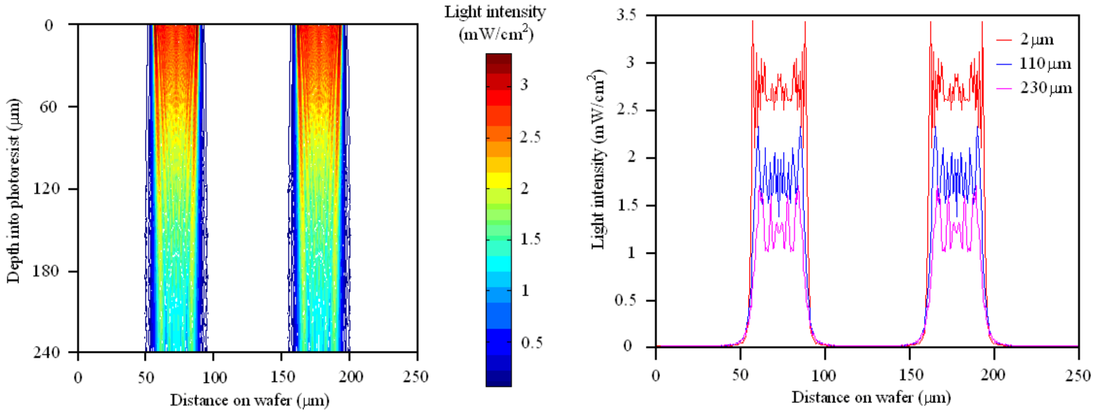

(a) (b)

Fig. 4 Simulated light intensity distribution into the SU-8 at the beginning of the exposure process under 280s exposure for 35μm/70μm line/space: (a) the light intensity distribution at the beginning, (b) Fresnel diffraction pattern for different depth in the SU-8 at the beginning

## Simulations and Discussions

Combining the above models and the surface movement algorithms for etching simulation, the UV lithography process simulations of the SU-8 can be implemented. Based on the improved 2D dynamic cellular automata method [4], developed from the original 2D dynamic cellular automata method [9], above mentioned aerial image simulation model, exposure simulation model, PEB simulation model and development simulation model can be used for the simulation of the UV lithography of thick

SU-8. To verify the simulation results, some experiments have been performed using SU-8 2075 under UV source with 365nm (2.6mW/cm$^2$) radiation.

Fig.4 shows the simulated light intensity distribution into the SU-8 at the beginning of the exposure process for 35μm/70μm line/space microstructure. Here the thickness of the SU-8 layer is 240 μm and the SU-8 is exposed for 280s using the contact exposure method (assuming the air gap between the mask and the SU-8 is about 15μm). Fig.5 shows the simulation and experimental profiles of the UV lithography of thick SU-8 for 13min development. The line width at different depth of the SU-8 microstructure was measured, and the variation from the top to the bottom is less than 2.01μm, and the largest line width variation between the simulation result and experimental result is less than 1.49μm.

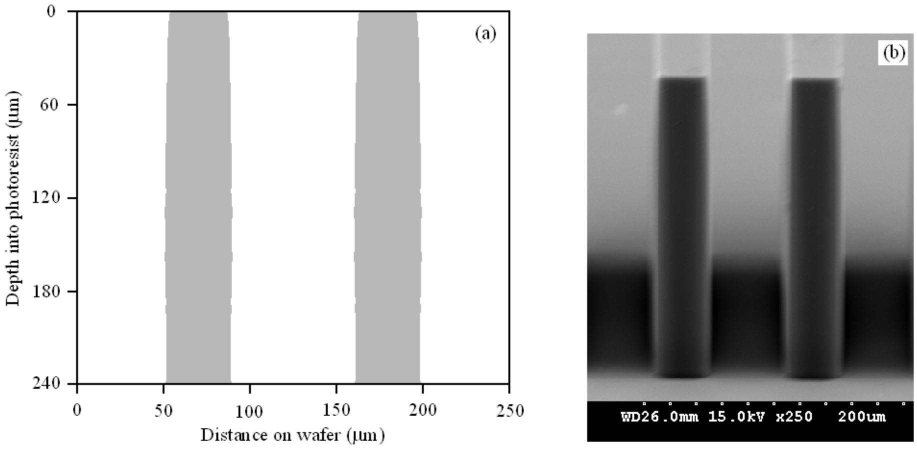

Fig. 5 Simulation result (a) and experimental result (b) for the UV lithography of the SU-8: exposure time=280s, development time=13min, line/space=35/70μm.

## Conclusions

The models for the UV lithography of thick photoresists have been presented. Combining the models and the improved dynamical cellular automata method, the UV lithography process simulations of the SU-8 have been implemented. The simulations have been verified by the experiments on SU-8 2075 layers under UV source with 365nm wavelength. The results confirm the validity of the proposed models.

## Acknowledgements

The authors thank Prof. Chen Di, Zhu Jun, and Ni Zhi-Ping from Shanghai Jiao Tong University, China for some experiments. The project is supported by the Foundation of Southeast University of China under Contract KJ2010409 and 3206000501.

## References

[1] A. Campo and C. Greiner: J. Micromech. Microeng. Vol. 17 (2007), p. R81

[2] A. Llobera, V. Seidemann, J. A. Plaza, V. J. Cadarso and S. Buttgenbach: J. Microelectromech. Syst. Vol. 16 (2007), p. 111

[3] R. Yang and W. J. Wang: Sens. Actuators Vol. B110 (2005), p. 279

[4] Z. F. Zhou, Q. A. Huang, W. H. Li, M. Feng, W. Lu and Z. Zhu: J. Micromech. Microeng. Vol. 17 (2007), p. 2538

[5] Y. J. Chuang, F. G. Tseng and W. K. Lin: Microsyst.. Technol. Vol. 8 (2002), p. 308

[6] F. H. Dill, A. R. Neureuther and J. A. Tuttle: IEEE Trans. Electron Devices Vol. ED-22 (1975), p. 456

[7] M. Zuniga, G. Wallraff and E. Tomacruz: J .Vac. Sci. Technol. Vol. B11 (1993), p. 2862

[8] A. Mack and G. Arthur: Electrochem. Solid-State Lett. Vol. 1 (1998), p. 86

[9] Z. F. Zhou, Q. A. Huang, W. H. Li and W. Lu: J. Micromech. Microeng. Vol. 15 (2005), p. 652

*Advanced Materials Research Vols. 201-203 (2011) pp 80-84*

*doi:10.4028/www.scientific.net/AMR.201-203.80*

# Research on Computer-Aided Conceptual Design of Palletizing Robot

Zhongming Li[a], Wei Liu[b]

[1]School of Automation, Beijing University of Posts and Telecommunications, 100876, China

[a]buptlzm@163.com, [b]twhlw@163.com

**Keywords:** Conceptual Design; Palletizing Robot; Computer-Aided Design

**Abstract.** The method of computer-aided design oriented to requirement configuration is present for the palletizing robot. Index of design requirement is quantified hierarchically. The whole function of palletizing robot is decomposed according to the working plane. The various kinds of attributes of function carriers are digitized and the consistency is kept with the index of design requirement. Optimal design scheme can be gotten by the computation of evaluation function constructed in this paper. The software of computer-aided conceptual design for palletizing robot is developed.

## Introduction

Conceptual design is very important stage in the whole design process of product and innovation, fuzziness and diversity are its features. Computer aided technology of conceptual design is a important research field at present. For mechatronic product, for example, the palletizing robot, the market requirements are diversified and there is an intense competition. The design scheme should be provided agilely according to the individual requirements. Such theories as Theory of the Solution of Inventive Problems (TRIZ) and Quality Function Deployment (QFD) support the process of conceptual design effectively and many papers about these research fields can be found [1]. Some researchers also do lots of works on the automatic generation of design scheme. For example, genetic algorithm, evolution strategy and ant algorithm are applied to the solution of conceptual design scheme [2] [3]. The solution of design scheme should be connected with design requirements from the market with individual requirements.

To meet the costumer requirements as much as possible, computer technology should be used to support fully the process of conceptual design and efficiency will be improved. For the studying object of palletizing robot's conceptual design, a method of digitized design is present in this paper. The requirements index and the attributes of function carriers are quantified, and evaluation method is constructed to select the optimal design scheme of palletizing robot meeting the customer requirement.

## Analysis of conceptual design of palletizing robot

**The general model of conceptual design.** The process of conceptual design of mechatronic products includes several steps as requirement analysis, function decomposition, scheming solving and evaluation [4]. The process model of conceptual design is shown in Fig.1. Firstly the design requirements of product are analyzed and the whole function is defined. Then the whole function can be decomposed into several sub functions. Feasible structure will be found out to realize every subfunction. Finally all function carriers are synthesized and evaluated and the optimal design scheme is obtained. Conceptual design of palletizing robot is based on the model shown in Fig.1 and computer-aided design process is realized in this paper.

**Function decomposition of palletizing robot.** The task of palletizing robot is transportation of goods from some position to another position and generation of regular stack in accordance with a certain pattern, and goods has no rotation around horizontal axis in process of motion. The whole function can be decomposed by working plane, as shown in Fig.2, after analyzing various kinds of structures and working characteristics of palletizing robot. Palletizing robot implements the elevation and lowering motion in YZ-plane and movement to the position of stack in XY-plane. Solving of scheme are done separately in these two motion plane. Function carriers meeting the requirement of movement in single working plane is very much, and structure form are various, so computer-aided technology is needed to assistant the rapid searching of optimal solution.

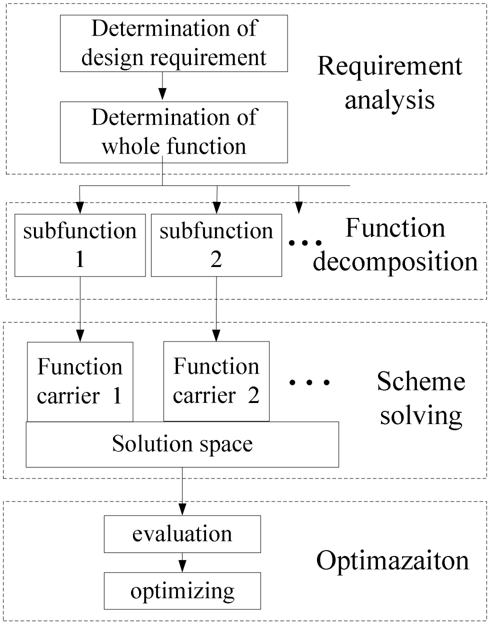

Fig.1. Process model of conceptual design

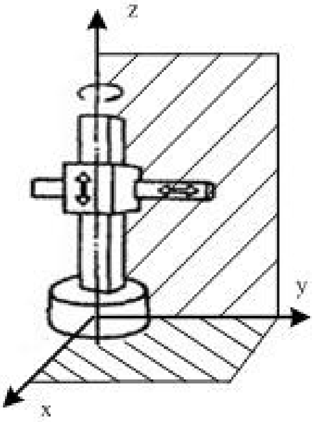

Fig.2. Function decomposition by working plane

### Application of computer- aided technology oriented requirement

To support the computer-aided conceptual design, digitization of design process is need to be realized which includes the digitization of design requirement, field knowledge and so on.

**Index of customer requirement.** Because of different environment and working object, there is a great difference in performance requirements of palletizing robot. For example, the palletizing object may be box with 5 kg medicine, or bucket with 100 kg liquid, but the demand for size and efficiency of palletizing robot are very different. So the optimal design scheme must be based on the analysis of individual customer requirement. Five main indexes of requirement are considered on the basis of analysis of working environment for many kinds of palletizing robot. The indexes are cost, size, load, efficiency and mass and they constitute the synthetic requirement index vector R

$$R = \{R_1, R_2, R_3, R_4, R_5\} \qquad (1)$$

where, $R_1$ is index of cost， $R_2$ is index of load， $R_3$ is index of efficiency， $R_4$ is index of size， $R_5$ is index of mass.

Consideration degree of these five requirement indexes are varied in different working environment, and the weight of requirement index is digitalized necessarily to support the application of computer-aided design. The numerical value on interval [0, 1] is used to define the consideration degree of every requirement index. If the value is 0, it indicates that there is no consideration on this requirement index. The value is bigger, this index is more important and the value 1 indicates that this index is the most important one compared with other indexes. Requirement weight vector W is composed of all weights of requirement index.

$$W = \{W_1, W_2, W_3, W_4, W_5\} \tag{2}$$

where, $W_i$ ( $0 \le W_i \le 1$， i=1,2,3,4,5） is the weight of corresponding $R_i$ .

**Digitalization of function carrier attributes.** To fully realize the computer-aided conceptual design for palletizing robot, the related field knowledge also needs to be digitalized. The whole function of palletizing robot is decomposed into subfunctions in XY-plane and YZ-plane, and function solutions in two planes are combined into the whole design scheme of palletizing robot. Solutions in every plane have various kinds of principles and structures and these function carriers constitute solution space.

To support the application of computer aided technology, attribute vector is constructed in which elements corresponding to requirement index are included. The attribute vector P is defined as follow.

$$P = \{P_1, P_2, P_3, P_4, P_5, P_6, P_7, P_8\} \tag{3}$$

where, the meaning of every element is shown in Tab.1.

The value of attribute is quantified as five grades so that difference in attribute of individual function carriers can be specified. The value of five grades is defined as 1, 2,3,4,5 and the meanings of quantified value for elements in attribute vector are shown in Tab.1.

Table.1. Meaning of function carrier attributes

| symbol | element | meaning of attribute value |
|---|---|---|
| $P_1$ | cost | 1-very high, 2-higher, 3-general, 4-lower, 5-very low |
| $P_2$ | load capacity | 1-very strong, 2-stronger, 3-genera, 4-weaker, 5-very weak |
| $P_3$ | efficiency | 1-very high, 2-higher, 3-general, 4-lower, 5-very low |
| $P_4$ | size | 1-very big, 2-bigger, 3-general, 4-smaller, 5-very small |
| $P_5$ | mass | 1-very heavy, 2-heavier, 3-general, 4-lighter, 5-very light |
| $P_6$ | input power | 1-electric, 2-mechanical, 3-hydraulic, 4-phneumatic, 5-other |
| $P_7$ | output power | 1-electric, 2-mechanical, 3-hydraulic, 4-pneumatic, 5-other |
| $P_8$ | movement type | 1-rotation, 2-translation, 3-other |

Attributes from $P_1$ to $P_5$ are consistent with elements in requirement index vector. Attributes $P_6$ and $P_7$ indicate power type of input and output port. They ensure the matching of upstream or downstream function carrier's port so that the combined function solution is feasible. The power types include electric, mechanical, hydraulic, pneumatic power and so on. $P_8$ indicates type of output motion which includes rotation and translation.

### Scheme generation based on evaluation function

**Definition of evaluation function.** Function carrier library is composed of lots of carriers and their attribute vector. It is the solution space for subfunctions of palletizing robot. For a specific design requirement, many feasible solutions can be found. The evaluation function is needed to determine every design scheme good or bad. Comprehensive evaluation is suitable for conceptual design.

Combined with requirement index stated in previous part, the evaluation function is defined as follow.

$$E = \sum_{i=1}^{n} \left( \sum_{j=1}^{5} W_j \cdot \left| R_j - P_{ij} \right| \right) \qquad (4)$$

where, n is total number of function carriers in whole design scheme.

$R_j$ is element of requirement index vector in Eq. 1, where $R_j$ should be the quantified value corresponding to requirement index. It indicates the different demand for individual index, and its value is1,2,3,4or5, where its meaning is consistent with the value in Tab.1. $W_j$ is element of weight in equation (2). $P_{ij}$ is element of attribute vector and it indicates the jth attribute value of ith function carrier. This evaluation measures the consistency between design requirements and attribute vectors of all carriers in whole design scheme. The value of E is smaller, the design scheme is more consistent with design requirement.

**Searching of optimal scheme.** The generation process of design scheme is shown in Fig.3. The computer-aided conceptual design is a process of man-computer interaction, and design procedures are based on function decomposition of palletizing robot. In XY-plane or YZ-plane, basic motion is further divided into rotation and translation and so on according to movement type. These parameters can be configured in man-computer interaction module. Every motion type can be mapped into many kinds of specific function carriers. For example, translation motion can be mapped into rack-and-pinion, lead screw and hydraulic cylinder and so on. According as parameters set in man-computer interaction module, computer searches the solution in function carrier library for single plane motion. Then the function solutions are combined and port matching of upstream and downstream carriers is ensured. All feasible combined solutions are found out and evaluated by evaluation function respectively. The design scheme whose value of evaluation function is the smallest is the optimal solution.

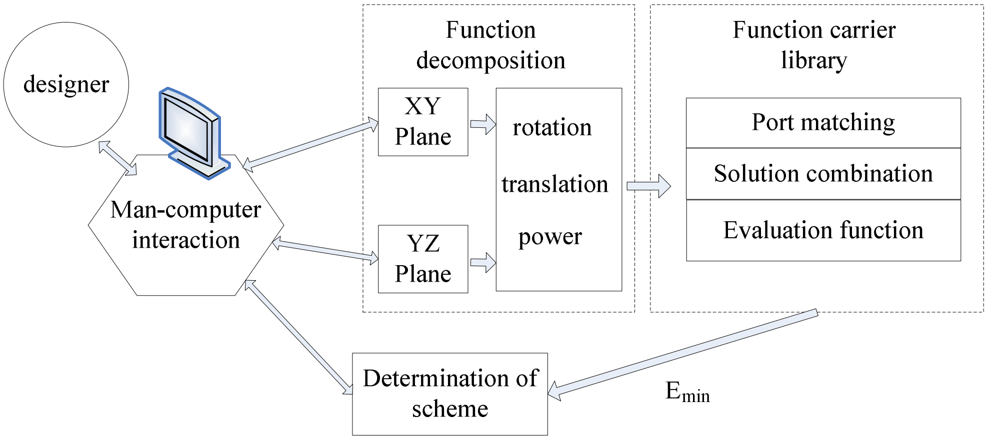

Fig.3. Process of scheme generation

## Software prototype

Software system of computer-aided conceptual design for palletizing robot - PRCAD is developed. Java program language and database management system MYSQL are used as development tools. Several modules are included in PRCAD, such as requirement design module, database management module, scheme solving module, result display module and so on.

Up to now tens of carriers is collected into the function carrier library. The library keep to be open and carriers can be added, edited or deleted. Optimal solution set can be provided by PRCAD according to the parameters in requirement design module. The solution set is composed of several optimal solutions whose value of E is minimum or second minimum.

## Conclusions

Palletizing robot is complex mechatronic product and scheme of conceptual design has the feature of multiplicity of solutions. Technology of computer-aided conceptual design can be applied to find out optimal scheme quickly. The method of computer-aided conceptual design for palletizing robot is present in this paper and is oriented to requirement configuration. Requirement index and attribute of function carrier are digitalized, and the optimal solution can be found out in lots of feasible solutions by evaluation function. Software system of is developed based on this method proposed in this paper. The software is used for conceptual design of palletizing robot and the method is reasonable and feasible.

## Acknowledgements

This work is supported by the Fundamental Research Funds for the Central Universities.

## References

[1] CUI Yong, SUN Feng: Computer Integrated Manufacturing Systems Vol.12 No.2 220-224 (2006). (In Chinese)

[2] QIU SL, KORK SC, CHEN CH: The international Journal of Advanced Manufacturing Technology, 20 (9) 683-691 (2002).

[3] Bo Ruifeng, Huang Hongzhong, Wu Weidong: Journal of XI'AN JIAOTONG University Vol.39 No.11 1236-1240 (2005). (In Chinese)

[4] ZHAO Hong, HUANG Hongzhong: Chinese Journal of Mechanical Engineering Vol.42 No.10 190-196 (2006). (In Chinese)

*Advanced Materials Research Vols. 201-203 (2011) pp 85-88*
*© (2011) Trans Tech Publications, Switzerland*
*doi:10.4028/www.scientific.net/AMR.201-203.85*

# Study on the Computer Numerical Control Process of Variable Pitch, Groove Depth and Groove Width Screw

Min Han[1a*], Shan Li[2b] ， Lutao Deng[3c]

[1] Department of Mechanical Engineering, Xiamen University of Technology, Xiamen, 361024,

[2] Department of Mechanical and Electric Engineering, Xiamen University, Xiamen, 361005, China

[3] Huaxia College, Xiamen, 361024，China

[1]hanw20032004@163.com, [2,3]mhan@xmut.edu.cn

**Keywords:** Variable Pitch; Groove Depth; Groove Width Screw; Mathematical Analysis; CNC Machining.

**Abstract:** The article introduces three design techniques of variable pitch & groove depth & groove width screw. We found parameterized mathematical model of the type of heterotypic screw by analyzing and computing. Then it can realize to CNC machining of variable pitch & groove depth & groove width screw on lathe.

## Introduction

Molding screw is the essential part in the nylon zipper molding machine. In the waterproof of nylon zipper molding machine, the temperature is changing constantly and leading to change nylon diameter and elongation constantly during molding process of sprocket. So the type of heterotypic screw should have groove with variable pitch & groove depth & groove width. Besides, this type of heterotypic screw is providing device of various extruding machine. It was widely used for the processing of raw material and delivery process in petroleum, chemical industry, steel rolling, oak plastic, light industry, and machine industry and so on [1]. Therefore, we have found the corresponding mathematic model by researching on the relationship between basic theory and parameters of the heterotypic screw. It can offer theoretical basis for optimized design and CNC machining of the heterotypic pitch screw. Then we developed special CNC machining program of variable pitch & groove depth & groove width screw.

## Design of heterotypic screw

A whole heterotypic screw is composed by export segment, middle segment and import segment. Then export segment and import segment usually are isometric spiral line. However, middle segment is variable spiral line which can be used variety of ways, such as steady accelerated spiral curve, sine or cosine accelerated spiral curve, polynomial accelerated spiral curve and so on. The distance from arbitrary point on spiral curve to initial point on screw is supposed as L. In the export segment, initial pitch is $R_0$, groove depth is $H_0$ and groove width is $d_0$. In the middle segment, variable pitch length is $L_m$, pitch variation is $\triangle R$, groove width variation is $\triangle d$, groove depth variation is $\triangle H$ and circle number of screw thread is i. If total circle number of variable pitch in middle segment is $i_m$, then in the import segment, pitch should be $R_m$, groove depth should be $H_m$ and groove width should be $d_m$. If rotational speed of screw is n, axial velocity of spiral curve can be expressed as $V=R*n$. After derivation calculus to velocity V, we can get acceleration equation as $a=V'$. Therefore, we can deduce mathematic equations of steady accelerated spiral curve, sine accelerated spiral curve and polynomial accelerated spiral curve respectively, as shown in Eq.1, Eq.2 and Eq.3[2].

$$\begin{cases} L = i * R_0 + i^2 * \Delta R \\ R = R_0 + (2i-1) * \Delta R \\ H = H_0 + \dfrac{i}{i_m} \Delta H \\ d = d_0 + \dfrac{i}{i_m} \Delta d \end{cases} \tag{1}$$

$$\begin{cases} L = \dfrac{R_m + R_0}{2} i - \dfrac{i_m}{\pi} * \dfrac{R_m - R_0}{2} \sin(\dfrac{i}{i_m} \pi) \\ R = \dfrac{R_m + R_0}{2} - \dfrac{R_m - R_0}{2} \cos(\dfrac{i}{i_m} \pi) \\ H = H_0 + \dfrac{i}{i_m} \Delta H \\ d = d_0 + \dfrac{i}{i_m} \Delta d \end{cases} \tag{2}$$

$$\begin{cases} L = R_0 i + (4L_m - R_m i_m - 3R_0 i_m) i^3 / i_m^3 + (\dfrac{1}{2} R_m i_m + \dfrac{3}{2} R_0 i_m - 2L_m) i^4 / i_m^4 \\ R = R_0 + (12L_m - 3R_m i_m - 9R_0 i_m) i^2 / i_m^3 + (2R_m i_m + 6R_0 i_m - 8L_m) i^3 / i_m^4 \\ H = H_0 + \dfrac{i}{i_m} \Delta H \\ d = d_0 + \dfrac{i}{i_m} \Delta d \end{cases} \tag{3}$$

We take blank for example, which is roughing column with diameter Φ10mm. Then the total length of screw thread is 151mm, variable pitch length is 18mm. In the export segment, the length is 60.5mm, initial pitch $R_0$ is 1.70mm, initial root diameter $D_0$ is Φ8.84mm and initial groove width $d_0$ is 0.75mm. And then from export segment to import segment, screw thread pitch gradually increases to $R_m$. In the import segment, the pitch $R_m$ is 1.88mm, root diameter $D_m$ is Φ8.30mm and groove width $d_m$ is 0.83mm. The above-mentioned screw parameters were respectively substituted into Eq.1, Eq.2 and Eq.3. We have found that the minimum theoretical error was Eq.1 of steady accelerated spiral curve model. The absolute error of screw pitch was -0.00007mm and relative error was 0.03889%.

### Mathematic analysis of variable pitch & groove depth & groove width screw

1) For Eq.1 of steady accelerated spiral curve model, axial velocity of spiral curve can be expressed as $V=R*n=R_0*n+\triangle R*n(2i-1)$. After derivation calculus to velocity V, we can get acceleration equation as $a=V'=2\triangle R*n$. So axial displacement of arbitrary point on spiral curve is uniformly accelerated rectilinear motion. The velocity is increasing along with a sloping line. However, acceleration is constant, which has a finite value mutation only at starting and ending point. It will come into being flexible impact. In the product line of high speed, flexible impact will lead to material running over by shaking. But if the device speed is not high, flexible impact will not affect the transmission stationarity. So this method is more applicable in low or middle speed motion control[3]. While using steady accelerated spiral curve model in the CNC machining control of variable pitch & groove depth & groove width screw, the transition of variable screw pitch is rather smooth and the cumulative error is minimal.

2) For Eq.2 of sine accelerated spiral curve model, acceleration equation can be expressed as $a=\frac{\pi n}{i_m}\frac{R_m-R_0}{2}\sin(\frac{i}{i_m}\pi)$. The acceleration line is a smooth and continuous sine curve in the accelerated segment, which is zero at starting and ending point. By using motion law of sine accelerated spiral curve, acceleration changes continuously during the whole process of screw transmission and it won’t bring any impact even in high speed. It can satisfy the request of stationarity in high speed screw. So this method is suitable for high speed motion[4]. However, it requires a higher processing. Besides, the displacement changes slowly in the starting and ending segment, so the cumulative error is relatively large.

3) For Eq.3 of polynomial accelerated spiral curve model, acceleration equation can be expressed as $a=V'=(\frac{(24L_m-6R_m i_m-18R_0 i_m)i}{i_m^3}+\frac{(6R_m i_m+18R_0 i_m-24L_m)i^2}{i_m^4})*n$. The acceleration changes continuously in the accelerated segment, which is zero at starting and ending point. This method can design different spiral curves according to different boundary conditions. And it can fulfill the requirement of displacement, velocity and acceleration to make material transmission steadily and accurately. However, there is some reasonless that it may occur interference when speed is too high or too low.

Therefore, we adopt steady accelerated spiral curve model to control screw machining.

## CNC program development of variable pitch & groove depth & groove width screw

In CNC lathe, we take single stroke thread cutting instructions G32 to machining variable pitch & groove depth & groove width screw. The instruction format is G32 X (U)___Z (W)___F___, in which X (U) and Z (W) is screw thread terminal point coordinate, F is pitch of screw thread[5]. We use Visual Basic6.0 to develop CNC program. In Visual Basic6.0, we add program codes about mathematic equations of variable pitch & groove depth & groove width screw, and then run program VB to acquire CNC machining codes of heterotypic screw[6]. By CutViewer Turn V3.0 of CNC lathe simulation software, we input NC codes and simulated. Then we measured the simulated machining screw. The result shows that in the export segment, initial pitch $R_0$ is 1.70mm, initial root diameter $D_0$ is Φ8.846mm and initial groove width $d_0$ is 0.752mm; in the import segment, the pitch $R_m$ is 1.88mm, root diameter $D_m$ is Φ8.34mm and groove width $d_m$ is 0.828mm; and then in the middle segment, the changes of pitch, groove depth and groove width were according with Eq.1. The simulation result indicates that the CNC machining program of variable pitch & groove depth & groove width screw is reasonable and feasible.

## Conclusions

This article has deduced and analyzed three parameterized mathematic model of variable pitch & groove depth & groove width screw. It can provide theoretical basis for machining control system about this type of heterotypic screw. And it will also offer a feasibility method to design or machining variable pitch screw. However, it still needs further research about practicing on CNC lathe to machining variable pitch & groove depth & groove width screw which tallies with size precision. What's more, as pledging machining precision, it also need perfect machining parameters by different machine to achieve more high efficiency machining. And that it can carry out to machining various heterotypic screws with complex structure and high precision.

## Acknowledgements

Fujian Provincial Natural Science Foundation (2008J04020) funded

## References

[1] Ren Xuejun, Lin Xiaojun, Shi Yaoyao. "The Research of Mathematics Model and NC Processing technique of Profiled Screw", *Machine Tool & Hydraulics,* 2004, 1:56-58

[2] Li Shan, Han Min, Deng Lutao. "Mathematics Model Analysis of Variable Pitch Screw", *Mechanical & Electrical Engineering Technology*, 1009-9492 (2009) 05-0029- 02

[3] Wu Guiquan. "Design and Manufacture of Simple Screw Curve with Variable Pitch", *Packaging and Food Machinery*, 1005-1295(2004) 02-0053- 02

[4] Lin Shuang．"A General Program for Pitch-varying Spiral Design Using UG", *Packaging and Food Machinery*. 1998，4（16）：8-15

[5] Liu Xiongwei. "CNC Machining Theory and Program Technology", Beijing: *Machine Industry Press*, 2000.01

[6] Chen Wenjie, Zhang Hui, Zhao Zhishui. "Mathematical Modeling Heterotypic Screw NC Programming", *Machine Design & Research*, 1006-2343（2008）03-110-03

*Advanced Materials Research Vols. 201-203 (2011) pp 89-92*
*© (2011) Trans Tech Publications, Switzerland*
*doi:10.4028/www.scientific.net/AMR.201-203.89*

# Numerical Simulation on Aerodynamics of Ramjet Projectiles

Jiaxian Zhang[a], Yanna Wang, Ruimin Liu

Beijing Institute of Aerospace Testing Technology, Beijing 100074, China

[a]callingxh@gmail.com

**Keywords:** Projectile; Ramjet; Aerodynamics; CFD; TVD

**Abstract:** Three-dimensional Reynolds-averaged Navier-Stokes simulations have been performed to explore the aerodynamic characteristics of ramjet projectiles. The turbulence model used is the RNG k-ε model. The numerical algorithms termed total variational diminishing (TVD) was adopted. The complex wave structures of ramjet projectiles with different architecture at different inflow Mach number were achieved by numerical simulation. The influence of inflow Mach number on aerodynamic characteristics and pressure center of ramjet projectiles were analyzed. Results show that lift coefficient and pressure center increase with the argument of inflow Mach number. Ramjet projectiles with different architecture have different drag coefficient trend.

## Introduction

Due to predominant performance of simpler structure, lower cost, higher assisted range efficiency, and smaller decreasing of warhead mass, various ramjet projectiles have been developed all around the world, including USA, South Africa and et al. One typical product is American TGTR for the 105-mm M68 tank cannon. Nowadays, by using ramjet to assisted range, the effective range of projectiles can be doubled.

Lots of researches have been done on ramjet projectiles. Chen Xiong has done investigations of ramjet inlet [1]. Ronald revealed the working on solid fuel ramjet propulsion for gun launched projectiles in the Netherlands Organization [2]. Guo Jian has studied flight performance of solid fuel ramjet [3]. Xiao Yinli et al. has done investigations of scramjet isolator [4]. Wang Yufeng has researched the inner flow of ramjet engine [5]. The TNO Defence, Security and Safety and DRDC-Valcartier have worked on the improvement of modeling and simulation tools for the functioning of supersonic air intake for realistic ramjet engines of tactical missiles [6].

As a key segment of research on ramjet projectiles, numerical simulation on aerodynamic characteristics are very important. The second-order implicit TVD scheme was adopted in this paper. And the RNG k-ε model was used to represent turbulence. Finally, the influences of Mach number on aerodynamic characteristics of ramjet projectiles were revealed.

## Computational Approach

With decades of development, present CFD approaches can predict the aerodynamic characteristics of vehicles accurately. Still, it is very hard to build a mathematical model which contains all kinds of factors. In this paper, gas-solid two-phase, multi-component and chemical reactions were neglected.

**Governing Equations.** Governing equations used here are the compressible, Reynolds-averaged Navier-Stokes equations in generalized coordinates. These equations are written in the following conservative form:

$$\frac{\partial U}{\partial t}+\frac{\partial F_1(U)}{\partial x}+\frac{\partial F_2(U)}{\partial y}+\frac{\partial F_3(U)}{\partial z}=\frac{\partial G_1}{\partial x}+\frac{\partial G_2}{\partial y}+\frac{\partial G_3}{\partial z} \tag{1}$$

Detailed formulation form could be found in [1].

**Turbulence Model.** According to the former experience, computational results verify with changes of turbulence model. An appropriate turbulence model helps to improve computing accuracy. The standard $k-\varepsilon$ model was very popular in the past. The RNG $k-\varepsilon$ model is brought forward by modifying the standard $k-\varepsilon$ model. The model comes from the strict statistic method. It is very similar with standard $k-\varepsilon$ model, but it has been ameliorated. These characters make the RNG $k-\varepsilon$ model more accurate and reliable than the standard $k-\varepsilon$ model in more complex flow.

The RNG $k-\varepsilon$ model is adopted as turbulence model in this paper. Neglecting influence of buoyancy, dissipation rating and turbulence energy are described as follow:

$$\rho\frac{Dk}{Dt}=\frac{\partial}{\partial x_i}\left[\left(\alpha_k\mu_{eff}\right)\frac{\partial k}{\partial x_i}\right]+G_k-\rho\varepsilon-Y_M \tag{2}$$

$$\rho\frac{D\varepsilon}{Dt}=\frac{\partial}{\partial x_i}\left[\left(\alpha_z\mu_{eff}\right)\frac{\partial \varepsilon}{\partial x_i}\right]+C_{1z}\frac{\varepsilon}{k}G_k-C_{2z}\rho\frac{\varepsilon^2}{k}-R \tag{3}$$

where, $G_k$ stands for turbulence energy caused by mean velocity gradient. $Y_M$ is the influence on total dissipation rating by pulse expansion of compressible turbulence. $\alpha_k$ is reciprocal of valid turbulent Prandtl number of turbulence energy $k$. $\alpha_\varepsilon$ is reciprocal of valid turbulent Prandtl number of dissipation rating $\varepsilon$. For high Reynolds number, $\mu_t=\rho C_\mu k^2/\varepsilon$ and $C_\mu=0.0845$ are suitable for the above equations.

**Numerical Algorithm.** By using implicit second-order TVD scheme, the discrete form of governing Eq. 1 could be transferred as follow:

$$V_{i,j,k}\frac{dU_{i,j,k}}{dt}=\begin{pmatrix}\widetilde{R}_{v,i+\frac{1}{2}}-\widetilde{R}_{v,i-\frac{1}{2}}+\widetilde{R}_{v,j+\frac{1}{2}}-\\ \widetilde{R}_{v,j-\frac{1}{2}}+\widetilde{R}_{v,k+\frac{1}{2}}-\widetilde{R}_{v,k-\frac{1}{2}}\end{pmatrix}-\begin{pmatrix}\widetilde{R}_{i+\frac{1}{2}}-\widetilde{R}_{i-\frac{1}{2}}+\widetilde{R}_{j+\frac{1}{2}}-\\ \widetilde{R}_{j-\frac{1}{2}}+\widetilde{R}_{k+\frac{1}{2}}-\widetilde{R}_{k-\frac{1}{2}}\end{pmatrix} \tag{4}$$

where, $V_{i,j,k}$ is cell volume, $\widetilde{R}_{i+1/2}$ is the convective fluxes of $\widetilde{R}_{i+1/2,j,k}$, $\widetilde{R}_{v,i+1/2}$ is the viscous fluxes of $\widetilde{R}_{v,i+1/2,j,k}$, and so on. Considered face $i$+1/2, by updating the convective fluxes, the second-order TVD scheme is achieved as follow:

$$\begin{cases}\widetilde{R}_{i+1/2}=\widetilde{H}_i^{+}+\widetilde{H}_{i+1}^{+}+\frac{1}{2}R_{i+1/2}\left(\phi_{i+1/2}^{+}+\phi_{i+1/2}^{-}\right)\\ \phi_{i+1/2}^{+}=\min\bmod\left(\Lambda_{i+1/2}^{+}R_{i+1/2}^{-1}\Delta_{i-1/2}U,\Lambda_{i+1/2}^{+}R_{i+1/2}^{-1}\Delta_{i+1/2}U\right)\\ \phi_{i+1/2}^{-}=\min\bmod\left(\Lambda_{i+1/2}^{-}R_{i+1/2}^{-1}\Delta_{i+1/2}U,\Lambda_{i+1/2}^{-}R_{i+1/2}^{-1}\Delta_{i+3/2}U\right)\\ \min\bmod(x,y)=\operatorname{sgn}(x)\max\left\{0,\min\left[|x|,y\operatorname{sgn}(x)\right]\right\}\end{cases} \tag{5}$$

After linearization and splitting by ADI method, the final numerical scheme is shown as Eq. 6.

$$\begin{cases}-\Delta\tau\overline{C}_{i-1/2}^{+,n}\cdot\delta U_{i-1,j,k}^{**}+\left[I+\Delta\tau\left(\overline{C}_{i-1/2}^{+,n}-\overline{C}_{i+1/2}^{+,n}\right)\right]\cdot\delta U_{i,j,k}^{**}+\Delta\tau\overline{C}_{i+1/2}^{-,n}\cdot\delta U_{i+1,j,k}^{**}=-\Delta\tau RHS\\ -\Delta\tau\overline{C}_{j-1/2}^{+,n}\cdot\delta U_{i,j-1,k}^{**}+\left[I+\Delta\tau\left(\overline{C}_{j-1/2}^{+,n}-\overline{C}_{j+1/2}^{+,n}\right)\right]\cdot\delta U_{i,j,k}^{**}+\Delta\tau\overline{C}_{j+1/2}^{-,n}\cdot\delta U_{i,j+1,k}^{**}=\delta U_{i,j,k}^{**}\\ -\Delta\tau\overline{C}_{k-1/2}^{+,n}\cdot\delta U_{i,j,k-1}^{**}+\left[I+\Delta\tau\left(\overline{C}_{k-1/2}^{+,n}-\overline{C}_{k+1/2}^{+,n}\right)\right]\cdot\delta U_{i,j,k}^{**}+\Delta\tau\overline{C}_{k+1/2}^{-,n}\cdot\delta U_{i,j,k+1}^{**}=\delta U_{i,j,k}^{*}\\ U_{i,j,k}^{n+1}=U_{i,j,k}^{n}+\delta U_{i,j,k}\\ RHS=\widetilde{R}_{i,j,k}^{n}-\widetilde{R}_{v,i,j,k}^{n}-\widetilde{R}_{s,i,j,k}^{n}\\ \Delta\tau=\Delta t/V_{i,j,k}\end{cases} \tag{6}$$

## Modeling and Boundary Conditions

Four kinds of ramjet projectiles analyzed in this paper are shown in Fig. 1. I type and III type of ramjet projectile each have a centre wimble. II type and IV type of ramjet projectile get ride of the centre wimble based on I type and III type, respectively. There are a few differences between I type and III type, such as structure of inlet and exterior structure of projectile. For the I type projectile, cylindrical part is connected with arc part by tangent, so its head is fat in some sort. For the III type projectile, cylindrical part is connected with arc part by secant, so its head is a little thin. In addition, some small holes are dig on stern parts of I type and II type.

(a) I type (b) II type

(c) III type (d) IV type

Fig. 1 Structures of each kind of ramjet projectile

Three-dimensional models were built for the aerodynamics analysis, with 6° angle of attack for lift coefficient analysis and no angle of attack for drag coefficient analysis. Inlet boundary and far field boundary use the conditions of far field of pressure. The temperature and static pressure of far field of pressure boundary is 288K and 101325Pa. Mach numbers of inflow are respectively 2.13, 2, 1.6, 1.4, 1.1 and 0.9.

## Results and Discussion

The typical character of flow field of ramjet projectile is the wave structure at base. Owing to the structure similarity, external flow structures of I type and III type of ramjet projectile are similar with II type and IV type of ramjet projectile, respectively. Wave structures of these four kinds of ramjet projectile at M=2.13 without angle of attack are shown in Fig. 2.

(a) I type (b) II type

(c) III type (d) IV type

Fig. 2 Wave structures of ramjet projectiles at M=2.13 without angle of attack

At M=2.13, due to the center pipe of ramjet projectile, jet flow structure appears at the base of I type, Arch bridge type of shock waves form at the exit of nozzle, intersect shock waves appear at the base of II type. Two titled shock waves will emerge in the combustion chambers of these two types of ramjet projectile. Comparing to the I type, due to the thin head, titled shock wave at outboard of inlet of III type became weaken obviously. Internal flow field of III type and IV type is obviously different. The reason is their different inlet structures.

Influences of Mach number on these kinds of ramjet projectile are shown in Fig. 3. For the lift coefficient, all kinds of ramjet projectile show the same trend that the coefficient rises with the increasing of Mach number. As shown in Fig. 3, lift coefficients of ramjet projectiles without centre wimble are bigger than those with centre wimble. For the drag coefficient, the trends are conversely different with lift coefficient. And drag coefficients of ramjet projectiles without centre wimble are smaller than those with centre wimble. As increasing of Mach number, these gaps become obscure, especially between Ⅲ type and Ⅳ type of ramjet projectile.

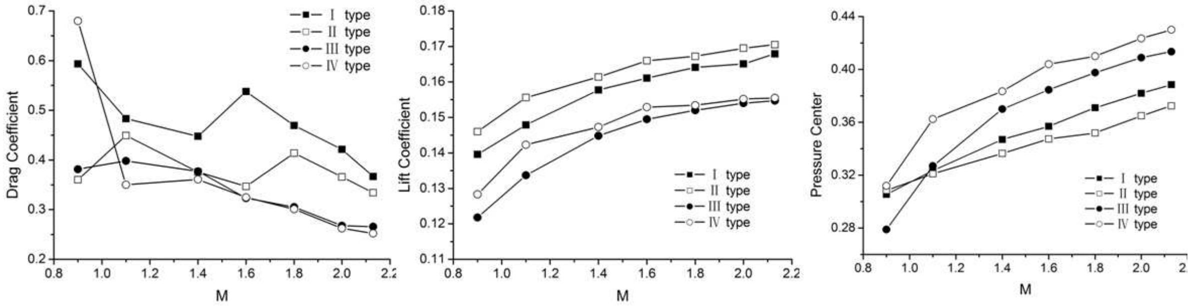

(a) Drag coefficient (b) lift coefficient (c) pressure center

Fig. 3 Influences of Mach number on aerodynamics

In this paper, definition of pressure center is relative to the head of projectile. As shown in Fig.3, the faster inflow is, the bigger pressure center is. Pressure centers of ramjet projectiles without holes at the stern part are bigger than those with holes. That means base wave structures have great influence on the pressure center.

## Conclusions

Aerodynamic characteristics of ramjet projectiles were numerically analyzed. Drag coefficient characteristics were achieved with no angle of attack. Lift coefficient and pressure center characteristics were achieved with angle of attack equaling to 6 degree. Results show that lift coefficient and pressure center increase with the argument of Mach number. In fact, lift coefficients of ramjet projectiles without centre wimble are bigger than those with centre wimble. Owing to the great influence of wave structures at base, pressure centers of ramjet projectiles without holes at the stern part are bigger than those with holes. Meanwhile, drag coefficients decrease with the argument of Mach number.

## References

[1] CHEN XIONG, ZHENG YA, ZHOU CHANGSHENG, JU YUTAO. Numerical simulation on ramjet inlet with different cowl leading edge, AIAA 2005-5288.

[2] Ronald G. Veraar and Alfons E. H. J. Mayer. The Role of the TNO Free Jet Test Facility in Solid Fuel Ramjet Projectile Development. AIAA 2005-3828.

[3] Jian GUO, Weihua ZHANG, Zhixun XIA. Flight performance analysis of the solid fuel ramjet. Journal of national university of defence technology. 2007, Vol.29, No.2: 10-14. (in Chinese)

[4] Yinli XIAO, Liang CHEN, Wenyan SONG. Study on flow characteristics of scramjet isolator. ACTA AERODYNAMICA SINICA. 2007, Vol.25, No.1: 75-79.

[5] Yufeng WANG, Xiaolong DUAN. Numerical study of the ramjet engine inner flow before ignition. Journal of rocket propulsion. 2006, Vol.32, No.6: 20-22.

[6] J. -L. Moerel, R. G. Veraar, and et al. Internal flow characteristics of a rectangular ramjet air intake. AIAA 2009-5076.

[7] Chakravarthy, S. R., Szema, K. Y., and et al. Application of a New Class of High Accuracy TVD Schemes to the Navier-Stokes Equations. AIAA paper 85-0165, Jan. 1985.

*Advanced Materials Research Vols. 201-203 (2011) pp 93-98*
*© (2011) Trans Tech Publications, Switzerland*
*doi:10.4028/www.scientific.net/AMR.201-203.93*

# A Parametric Die-Base in SolidWorks

Xinqun Zhang

64 South Fengle Road, Chuzhou, Anhui, China

winston4380@yahoo.com.cn

**Keywords:** Solidworks; Re-Development; Die-Base; Parametric Design; Mold Handle

**Abstract:** The study of parametric die-base developed on SolidWorks is presented in this paper. Here Visual Basic 6.0 is selected as the development tool, and the handle of a die is taken as an example to describe the design process with dimension driving. Users may create a series of standard-parts automatically by inputting different parameters through the application interface developed with VB.

## Introduction

Currently, a great variety of CAD software is used in the three-dimensional design in our country's mold enterprises. SolidWorks is quite widely used.

The standard-parts of ramming molds include guide pillars, guide sleeves, mold bases, mold handles, throwout levers, roof bars, educing material pins, blocking material pins, discharging bolts, bolts, positioning pins, compression springs and so on, which are transferred repeatedly in the mold design process. Since there is no standard-parts base meeting China's GB codes in SolidWorks, some designers have to consult GB codes frequently and revise some specific sizes repeatedly when they transfer standard parts of different specifications in order to renew the entire accessory model. This revision process is extremely tedious and requires massive duplication work, resulting in a long design cycle and low efficiency. Therefore, in order to enhance the application effect of SolidWorks in China's mold enterprises, we must localize and specialize our re-development of SolidWorks to establish a new ramming mold standard-part base.

## SolidWorks re-development methods

The model created by SolidWorks is an entirely parametric three-dimensional model, and the re-development of SolidWorks is based on the parametric design to the accessory model.

**The concept of parametric design.** The parametric design is a highly effective design method which realizes the shape control of the accessory through geometric constraints.

The parametric design process first carries on the parameterization modeling, namely establishing the initial geometry model of the accessory, defines the size of the controlled model shape structure as the variable parameter, and then actuates the parametric model by assigning different values to the variable parameter using the data in the parameter base to restructure the model. This size of the controlled accessory model shape structure is called the characteristic size.

The parametric design process of die-base is as shown in Fig. 1.

**SolidWorks re-development methods.** At present, SolidWorks re-development methods used by enterprises include programming method and size actuation method.

**a.**Programming method

The programming method means transcribing the entire modeling process while modeling the initial accessory, revising the transcribed macrocode, changing the constants to variables, and finally playing the modeling process back.

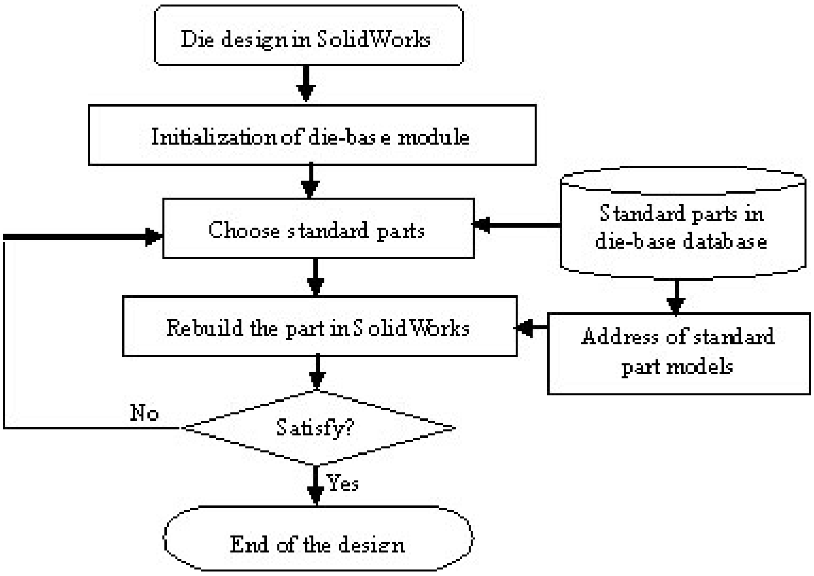

**Fig. 1**. **The parametric design process of die-base**

Although the programming method principle is relatively simple, and the macro-tool can be very conveniently transferred, it requests designers to be familiar with C + +, VB, VC and other high-level programming languages, and also grasp a great deal of SolidWorks API functions. Because some functions may be left out when transcribing accessory models with macro-tools, the developer has to intentionally compile procedure codes using SolidWorks API function to make it up, thus result in additional difficulty in its realization.

Moreover, the model creation process needs to be executed from beginning to end when the accessory model is renewed, resulting in the long design time and low efficiency.

**b.** Dimension driving method

The dimension driving method maintains the accessory model structure unchanged, assigns different values to the characteristic size parameters by compiling procedure codes, and then renews the entire model according to the new size values.

The model recreating process in the programming method can be omitted by using the dimension driving method. It only needs to control the changes of the characteristic size based on the original accessory model and renew it.

Therefore the compiled program codes customizable and their total quantity is limited, with a high speed of graph renewal and high efficiency. It is more advantageous that designers can be freed from numerous massive SolidWorks API functions and may even complete the re-development without knowledge of SolidWorks API. Dimension driving method may be the application direction in die-base development, and a very high potentional application value in mold and die industry.

## Developing the die-base with dimension driving method

This paper introduces the development process of die-base with Visual Basic 6.0 as the development tool and the rimmed mold handle accessory as an example.

**Establishing the initial accessory model of the rimmed mold handle.** Taking A30×75 JB27646.3-1994 rimmed mold handle Type A as an example, we'll establish an accessory model on SolidWorks interface, as shown in Fig.2, preserved as "rimmed mold handle Type A. sldprt". There are five characteristic size controlling this accessory model, namely the mold handle diameter$\varphi$30, the rimmed diameter φ75, the rimmed height 16, the hitting pole aperture 11, the total height 64 (note: the size unit is mm). The mold handle accessory structure will change along with their different values.

**Editing size names.** When the model of rimmed mold handle Type A is established, SolidWorks system can assign a default size name for the labeled sizes: D1, D2, D3, D4, D5, D6, as shown in Fig.2. But this kind of size naming is extremely irregular without explicit significance, and may be shared by many characteristic sizes. In the parametric design, there is no special request for size naming, but in order to avoid confusion in transferring variable parameter values when the program is compiled, the labeled sizes should be renamed according to its need.

For example, double-click “sketch 1” in the characteristic manager and then click the right key on the size φ30 (size name is “D1”), choose “attribute” from the pop-up shortcut menu. When the “size attribute” dialog box appears, change the size name to “d”, and then confirm. Likewise, change the other specification size names to D2, h, HH, and DD respectively, as shown in Fig.3.

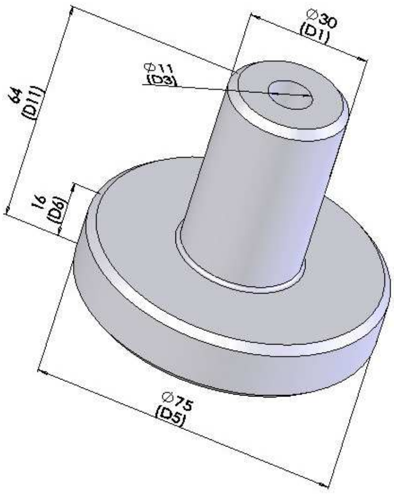

**Fig.2. Accessory model of rimmed mold handle Type A**

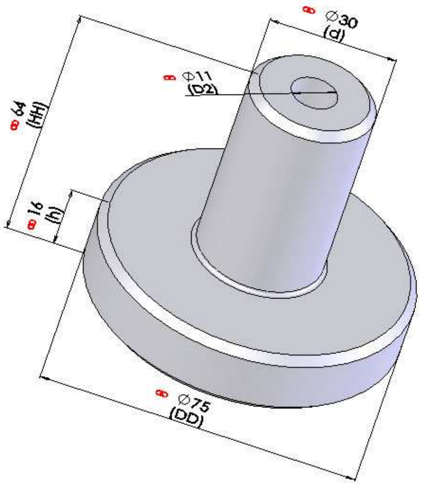

**Fig.3. Size names of rimmed mold handle Type A**

**Designing the window interface for VB documents.** Establish a VB project document, then open the menu item “project”→ “part”, and then append an outside control: Microsoft FlexGrid Control 6.0.

Append an image control on the VB window, a Data control, an MSFlexGrid1 control, and two Command controls. The VB window's interface design is as shown in Fig.4.

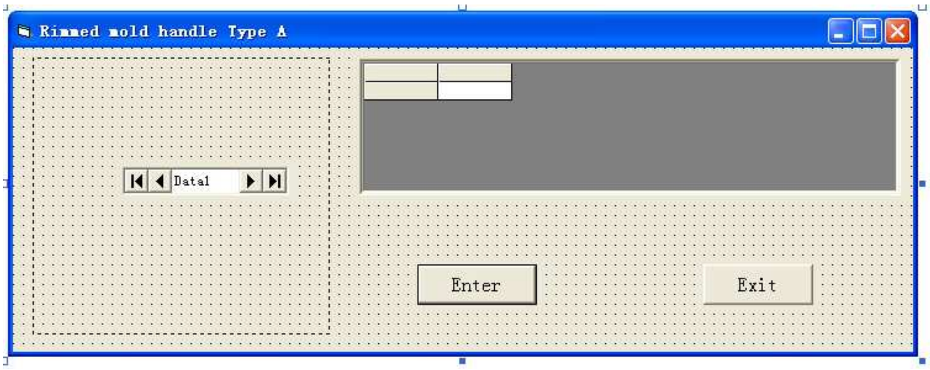

**Fig.4. The VB program window interface design of rimmed mold handle Type A**

**Establishing the database file of variable parameters for the accessory model.** Because rimmed mold handle Type A is a standard-part, its characteristic sizes are bundled with some serial of the mold standards. Here the database technology might be used, storing the characteristic size values in the database according to certain data structure forms to be managed by the database system in unification.

This paper adopts Microsoft Access 2003 as the database management system, taking the mold handle diameter d, the rimmed diameter DD, the rimmed height h, the hitting pole aperture D2, the total height HH as the variables, and establishes the data sheet as shown in Fig.5.

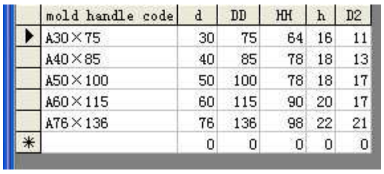

|  | mold handle code | d | DD | HH | h | D2 |
|---|---|---|---|---|---|---|
| ▶ | A30×75 | 30 | 75 | 64 | 16 | 11 |
|  | A40×85 | 40 | 85 | 78 | 18 | 13 |
|  | A50×100 | 50 | 100 | 78 | 18 | 17 |
|  | A60×115 | 60 | 115 | 90 | 20 | 17 |
|  | A76×136 | 76 | 136 | 98 | 22 | 21 |
| * |  | 0 | 0 | 0 | 0 | 0 |

Fig.5. Datasheet of A rimmed mold handle

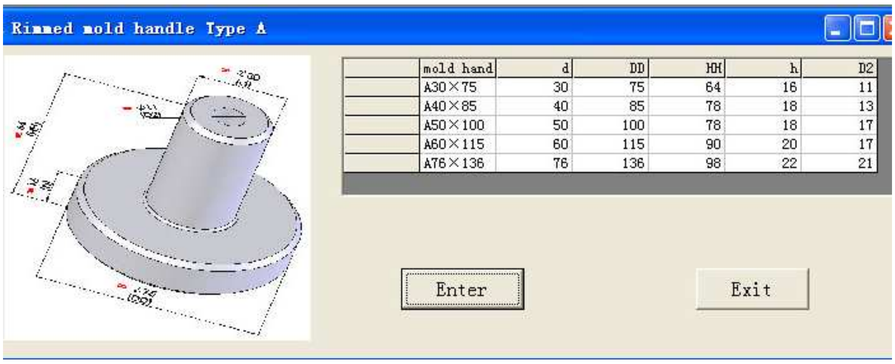

|  | mold hand | d | DD | HH | h | D2 |
|---|---|---|---|---|---|---|
|  | A30×75 | 30 | 75 | 64 | 16 | 11 |
|  | A40×85 | 40 | 85 | 78 | 18 | 13 |
|  | A50×100 | 50 | 100 | 78 | 18 | 17 |
|  | A60×115 | 60 | 115 | 90 | 20 | 17 |
|  | A76×136 | 76 | 136 | 98 | 22 | 21 |

Fig.6. File "rimmed mold handle Type A. exe"

**Compiling VB program codes.** The main VB program segments are as follows:

```
Private Sub Command1_Click()
    Set swApp = GetObject(, "SldWorks.Application")
    Set swPart = swApp.OpenDoc(App.Path & "\ A rimmed mold handle. sldprt", 1)
    swPart.Parameter("d@ sketch 1").SystemValue = d / 1000
    swPart.Parameter("DD@ sketch 1").SystemValue = DD / 1000
    swPart.Parameter("HH@ sketch 1").SystemValue = HH / 1000
    swPart.Parameter("h@ sketch 1").SystemValue = h / 1000
    swPart.Parameter("D2@ sketch 2").SystemValue = D2 / 1000
    swPart.EditRebuild
    swPart.ViewZoomtofit2
End Sub
Private Sub Form_Load()
    Image1.Picture = LoadPicture(App.Path & "\ rimmed mold handle Type A. jpg ")
    Data1.DatabaseName = App.Path & "\ rimmed mold handle Type A.mdb"
    Data1.RecordSource = " table1"
End Sub
Private Sub MSFlexGrid1_SelChange()
    MSFlexGrid1.Col = 2: d = CDbl(MSFlexGrid1.Text)
    MSFlexGrid1.Col = 3: DD = CDbl(MSFlexGrid1.Text)
    MSFlexGrid1.Col = 4: HH = CDbl(MSFlexGrid1.Text)
    MSFlexGrid1.Col = 5: h = CDbl(MSFlexGrid1.Text)
    MSFlexGrid1.Col = 6: D2 = CDbl(MSFlexGrid1.Text)
End Sub
```

**Creating file "rimmed mold handle Type A.exe".** File "rimmed mold handle Type A**.exe**" is as shown in Fig.6.

The EXE file in fact provides a man-machine conversation window which may be conveniently run right in Windows.

When the EXE file is executed, the different specification standard code numbers and the characteristic size values of rimmed mold handle Type A set by JB27646.3 can be shown in the window, and users may choose different standard-part code numbers directly and specifically to obtain the corresponding model of rimmed mold handle Type A.

**Expanding standard-part base of the rimmed mold handle.** The rimmed mold handle falls into three types in JB27646.3, Type A, B, and C, types B and C with 3~4 countersunk head screw holes on the rimmed end face bare based on Type A. When accessories are modeled, the screw hole needs to be driven by five characteristic sizes. Therefore, more size variables are needed to control rimmed mold handles Type B and Type C, as shown in Fig.7.

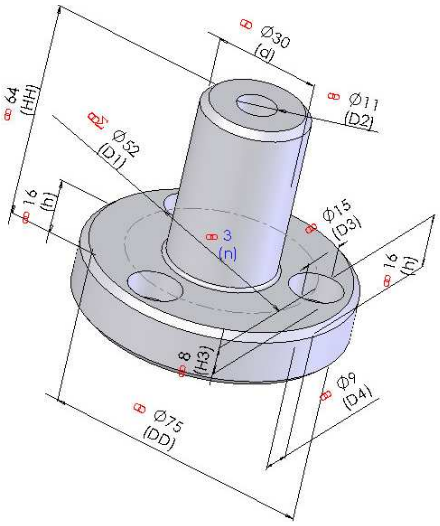

**Fig.7. Size names of B rimmed mold handle**

Firstly increase a screw hole based on the model of rimmed mold handle Type A, and distribute equally it to three. Then standard-part bases for rimmed mold handles Type B or C may be developed with the same method as A, only increasing some sentences in the original procedures.

The main VB program segments developing rimmed mold handle standard-part base are as follows:

```
Private Sub Command1_Click()
    ……
        swPart.Parameter("hole diameter @ sketch 6").SystemValue = D4 / 1000
        swPart.Parameter("pillar countersunk head hole diameter @ sketch6").SystemValue = D3 / 1000
        swPart.Parameter("D1@ sketch3").SystemValue = D1 / 1000
        swPart.Parameter("pillar countersunk head hole depth@ sketch6").SystemValue = H1 / 1000
        swPart.Parameter("n@ array (circle)1").SystemValue = Text1.Text
……
Private Sub MSFlexGrid1_SelChange()
……
        MSFlexGrid1.Col = 7: D4 = CDbl(MSFlexGrid1.Text)
        MSFlexGrid1.Col = 8: D3 = CDbl(MSFlexGrid1.Text)
        MSFlexGrid1.Col = 9: D1 = CDbl(MSFlexGrid1.Text)
        MSFlexGrid1.Col = 10: H1 = CDbl(MSFlexGrid1.Text)
End Sub
```

Problems may appear in this program development. The unit controlling characteristic sizes of this accessory model is length unit, and therefore the parameter values corresponding to GB can be directly put into database files, while the parameter n showing the number of the screw holes is not measured by the length unit, so it should be distinguished from the other characteristic size parameter set.

This paper adopts an extremely simple method. It does not list the parameter n showing the number of the screw hole into the database, but sets another sentence for users to choose the number of the screw freely.

**swPart.Parameter("n@ array (circle)1").SystemValue = Text1.Text**

Meanwhile a Label control and a Text control are appended on the VB window. Users may choose the number of screw flexibly according to their needs when running the program, breaking through the 3 or 4 number limit in GB code.

The created file “rimmed mold handle .exe” is as shown in Fig.8. When executing the customized module, first choose the code number of the rimmed mold handle to be found in the data sheet, then manually input the screw hole number, and then click the “modeling” button; the corresponding rimmed mold handle accessory model can be obtained.

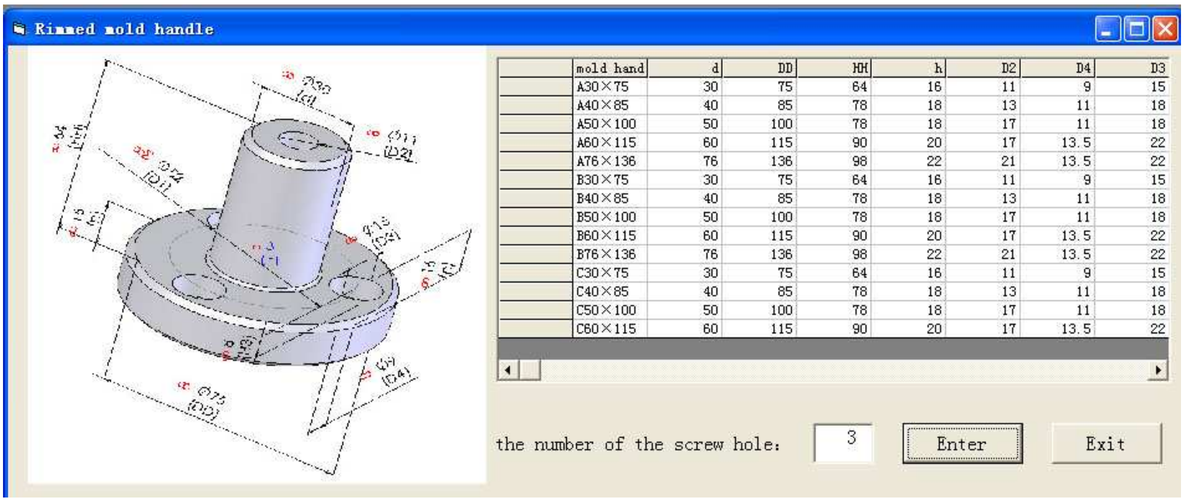

| | mold hand | d | DD | HH | h | D2 | D4 | D3 |
|---|---|---|---|---|---|---|---|---|
| | A30×75 | 30 | 75 | 64 | 16 | 11 | 9 | 15 |
| | A40×85 | 40 | 85 | 78 | 18 | 13 | 11 | 18 |
| | A50×100 | 50 | 100 | 78 | 18 | 17 | 11 | 18 |
| | A60×115 | 60 | 115 | 90 | 20 | 17 | 13.5 | 22 |
| | A76×136 | 76 | 136 | 98 | 22 | 21 | 13.5 | 22 |
| | B30×75 | 30 | 75 | 64 | 16 | 11 | 9 | 15 |
| | B40×85 | 40 | 85 | 78 | 18 | 13 | 11 | 18 |
| | B50×100 | 50 | 100 | 78 | 18 | 17 | 11 | 18 |
| | B60×115 | 60 | 115 | 90 | 20 | 17 | 13.5 | 22 |
| | B76×136 | 76 | 136 | 98 | 22 | 21 | 13.5 | 22 |
| | C30×75 | 30 | 75 | 64 | 16 | 11 | 9 | 15 |
| | C40×85 | 40 | 85 | 78 | 18 | 13 | 11 | 18 |
| | C50×100 | 50 | 100 | 78 | 18 | 17 | 11 | 18 |
| | C60×115 | 60 | 115 | 90 | 20 | 17 | 13.5 | 22 |

the number of the screw hole: 3

**Fig.8. File “Rimmed mold handle. exe”**

## Conclusions

The application of re-development on SolidWorks to creat die-base can thoroughly save users time in manually revising the size value repeatedly in the SolidWorks interface, effectively reduc redundant work in the mold and die design, and enhanc the design automation.

Meanwhile, the created die-base conforms to China’s project charting standard and three-dimensional modeling provides a friendly man-machine communication interface, which can meet the needs of mold designers, and therefore is especially valuable in middle and small mold enterprisees.

## References

[1] Zhong Ji, Xiaoli Wang, and Ren Liu: *Die Mold Design Automation - SolidWorks Application* (Chemical Industry Publications, China 2007). (In Chinese)

[2] Xinqun Zhang: submitted to Mold industry (2009).(In Chinese)

[3] Zheng Wei, Lin Mou: *SolidWorks2004.Cold-punched.Die.Design.Training.Tutorial* (Electronics Industry Publications, 2005). (In Chinese)

*Advanced Materials Research Vols. 201-203 (2011) pp 99-102*
*© (2011) Trans Tech Publications, Switzerland*
*doi:10.4028/www.scientific.net/AMR.201-203.99*

# A Study on the Digital Simulation for Sheet Metal CNC Incremental Forming Based on Z-Map

Hu Zhu[1,a], Zhijun Liu[1,b] and Jaegwan Kang[2,c]

College of Mechanical and Electrical Engineering, Shenyang Aerospace University, Shenyang, Liaoning 110136,

ChinaSchool of Mechanical Engineering, Kyungnam University, Masan 631701, South Korea

[a]zhuhu100@yahoo.com.cn, [b]dongfangshenglong1@163.com, [c]jkkang@kyungnam.ac.kr

**Keywords:** Incremental Forming; Digital Simulation; Z-Map; CAD/CAM

**Abstract:** A method of the digital simulation for the sheet metal CNC incremental forming was proposed based on the Z-map model. The tool extrusion movements were divided into two types according to the principle of sheet metal CNC incremental forming, i.e. vertical movement and horizontal movement. The vertical and horizontal swept volumes of the tool were built to intersect with the Z-map model of sheet metal respectively and the simulation models were generated. The thickness of deformed sheet metal was predicted and the thickness distribution chart was generated. The case studies show that the method can be applied to NC code verification, forming parameters optimization and formability prediction, moreover the system runs stably and reliably in the whole simulation process.

## Introduction

Sheet metal CNC incremental forming is an innovative flexible forming technology developed recently[1]. In this technology, the forming is realized by the extruding of tool along the outline of the part[2], so the toolpath and forming parameters that are used for controlling the tool movements have enormous effects on the forming accuracy and time[3]. The simulation technology is a powerful tool for the optimization of forming parameters and reasonable toolpath planning for CNC incremental forming. However, the researches on the simulation for CNC incremental forming are not fully done. There has not been special simulation software developed for CNC incremental forming by now. Most of researches adopts the commercial FEM(finite element method) software such as ANSYS, ABAQUS etc[4,5,6,7]. Since the FEM software cannot directly describe 3D curve, they cannot be suitable for the simulation of the tool movements whose path is complicated 3D curves[8].

CNC incremental forming technology is mainly to face the forming of sheet metal parts with complicated surfaces whose forming paths are complicated curves. Due to its complexity, there must be some errors in the NC code and forming parameters. Therefore, it is necessary to check the NC code, optimize the forming parameters and predict the forming results through simulation before the actual forming process. Thus, the research on the method of simulation for CNC incremental forming is very imperative.

## Digital Simulation of CNC Incremental Forming

The sheet metal CNC incremental forming adopts the layered manufacturing technology of the rapid prototyping. The sheet metal is fixed on the backing plate which can slide up and down freely along the guide, and a support is put under the sheet metal to hold up the sheet metal. The sheet metal and tool have a longitudinal feed under the control of the computer, and then the tool extrudes the sheet metal along the contour path. After that, the tool has a longitudinal feed and extrudes the sheet metal along the next contour repeatedly.

In the developed simulation system, support, sheet metal and tool are represented by using STL, Z-map and spherical equation respectively so as to calculate the deformation of the sheet metal expediently. Z-map is a lattice vector model that represents surface with the height values at grid points on the XY plane. The Z-map model can be represented as $\vec{Z}_i(x_i, y_i)$, where $(x_i, y_i)$ represent the positions of grid points on the XY plane. $\vec{Z}_i$ are the vectors along $z$ axis at grid points. $|\vec{Z}_i|$ are the height values along $z$ axis at the grid points, i.e. Z-map values, where $i = 0, 1, 2, \cdots n$. The simulation for the forming process is divided into two parts: one is the simulation for the downward moving process of sheet metal under the control of clamping plate and backing plate; the other is the simulation for the forming process of the sheet metal by the extruding of the tool.

**Simulation on the Downward Moving Process of Sheet Metal.** In the process of sheet metal CNC incremental forming, the sheet metal moves down a longitudinal feed depth under the drag of clamping plate, which coincides with the downwards movement of the tool. Simulation of the process is realized by the intersection between the Z-map model of sheet metal and the STL model of support. The upper surface of the sheet metal is used in the intersection calculation. The detailed process is as follows: ① Extracting the upper surface of the support. The extracting algorithm is first to find the signs of the $z$ coordinate of the normal vectors of the triangular facets, then extract the facets whose $z$ coordinate of the normal vectors are not negative. ②Building the model of sheet moved down. The model of sheet moved down can be built by modifying the values $|\vec{Z}_i|$ at grid points of the Z-map model of sheet metal. ③ Intersecting between sheet metal and support. In order to construct the model of the upper surface of the sheet metal after moving down, the intersection between sheet metal and the upper surface of support should be done. Then the Z-map values of sheet metal are updated to the sum of $z$ values of intersection points and the thickness of sheet metal.

**Simulation on the Extruding Process of Tool.** This paper adopted the concept of tool swept volume which is used in the CNC milling simulation. The real-time simulation for the incremental forming process is carried out by updating the deformed shape through calculating the intersection between the tool swept volume and Z-map model of sheet metal. The structure of tool swept volume is related to the tool type and the toolpath. As mentioned above, the movements of the tool have two types: longitudinal feed along the vertical direction and lateral feed along the contours. Therefore, the tool swept volume referred in this paper can be divided into longitudinal feed swept volume and lateral feed swept volume according to the styles of toolpath, as shown in Fig. 1(a), where $v_0 v_1$ indicates the toolpath. According to the feed styles of tool, there are two cases about the intersection between the Z-map model of sheet metal and the tool swept volume: ①When the tool extrudes the sheet metal along the contour on a layer, if the grid points $Z_i$ are in the XY plane projection area of the tool swept volume, they must be the points extruded by tool. Computing the intersection between $Z_i$ and the tool swept volume, and comparing the $z$ values of intersection points with the $z$ values of grid points. If the $z$ values of intersection points are less than that of grid points, this means the sheet metal is extruded by the tool, and then *z* values of $\overline{Z_i}(x_i, y_i)$ are updated to the *z* values of intersection points. As shown in Fig. 1(b), the projection area of the tool swept volume on XY plane is divided into *A*, *B* and *C* three portions. Where, $v_0(x_0, y_0, z_0)$ and $v_1(x_1, y_1, z_0)$ are two adjacent points of the contour on a layer, *r* is the radius of the ball-end tool, $p_i'(x_i', y_i', z_0)$ is the projection of $Z_i$ on the line $v_0v_1$, *d* is the distance from $Z_i$ to the line $v_0v_1$. If $|Z_iv_0| \le r$ and $p_i'$ isn't on the line segment $v_0v_1$, then $Z_i$ is in the area *A*, and the intersection between the vectors $\overline{Z_i}$ and the tool swept volume can be calculated by using Eq. 1. ② When the tool moves down from one layer to the next layer, as shown in Fig. 1(a), the effective tool swept volume is its ball-end. Ascertaining whether $Z_i$ is in the projection area of the effective tool swept volume by judging if they satisfy the condition $|Z_iv_1| \le r$. For the grid points in the projection area, Eq. 2 is used for computing the intersecting points and the *z* values of $Z_i$ are updated using the method mentioned above.

$$\begin{cases} (x-x_0)^2 + (y-y_0)^2 + (z-z_0)^2 = r^2 \\ z \le z_0 \end{cases} \tag{1}$$

$$\begin{cases} (x-x_1)^2 + (y-y_1)^2 + (z-z_1)^2 = r^2 \\ z \le z_1 \end{cases} \tag{2}$$

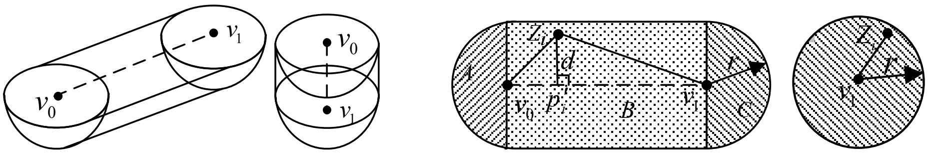

(a) (b)

Fig. 1 (a) Tool swept volume (b) The projection of tool swept volume

**Deformed Sheet Metal Thickness Prediction and Its Distribution Chart Visualization.** The deformed sheet metal thickness is predicted according to the sine's law of thickness change in CNC incremental forming[9]. The sine's law can be described as $t = t_0 \sin\theta$, where *t* is the deformed sheet metal thickness, $t_0$ is the initial sheet metal thickness, $\theta$ indicates the angle between the forming plate and vertical direction. In order to observe the change of sheet metal thickness, thickness change of sheet metal is needed to be represented by using different colors. Therefore, the Z-map model was converted into STL model and was visualized by OpenGL.

## Case Studies

The simulation platform was established using VC++ and OpenGL graphics library on the Windows XP. The user interface of the simulation software, the sheet metal, support, tool and the inputted NC code are shown in Fig. 2, in which the initial thickness of sheet metal is 2 mm, the radius of ball-end tool is 5 mm, the longitudinal feed depth is 0.4 mm. The simulation of the sheet metal CNC incremental forming process is shown in Fig. 3(a). The distribution of sheet metal thickness and the value of sheet metal thickness acquired from simulation are shown in Fig. 3(b).

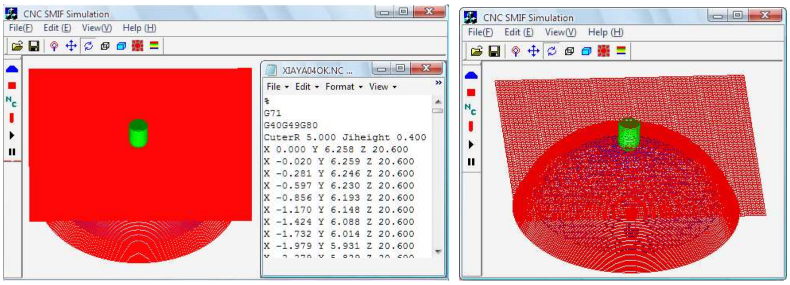

```
%
G71
G40G49G80
CuterR 5.000 Jiheight 0.400
X 0.000 Y 6.258 Z 20.600
X -0.020 Y 6.259 Z 20.600
X -0.281 Y 6.246 Z 20.600
X -0.597 Y 6.230 Z 20.600
X -0.856 Y 6.193 Z 20.600
X -1.170 Y 6.148 Z 20.600
X -1.424 Y 6.088 Z 20.600
X -1.732 Y 6.014 Z 20.600
X -1.979 Y 5.931 Z 20.600
```

Fig. 2 Simulation software system

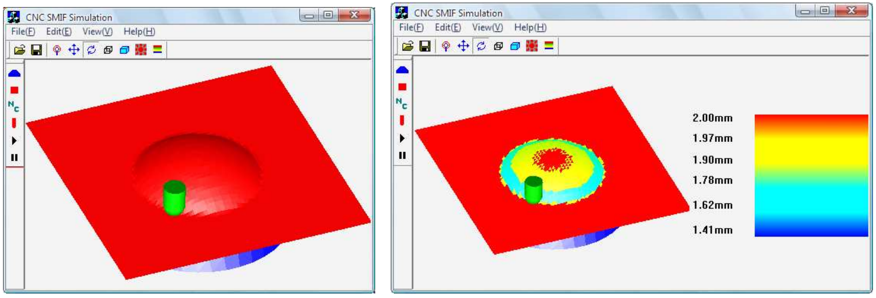

Fig. 3 (a)Simulation process (b)Sheet metal thickness chart

## Conclusions

The method of simulation for the CNC incremental forming was studied based on the Z-map model, and the related software system was developed. The system can realize the real-time simulation on CNC incremental forming according to the NC code inputted and runs stably and reliably, which can be used not only to verify the forming NC code and optimize the forming parameters, but also to predict the thickness of formed parts and then estimating the formability, thus can save the cost and time than the actual trial forming.

## Acknowledgements

The author gratefully acknowledges the financial support from the Natural Science Foundation of Liaoning (No. 20082012) and the Aerospace Science Foundation of China (No. 2009ZA54005).

## References

[1] A. Kochan: Assembly Automation Vol. 21(2001), p. 321.
[2] J.J. Park and Y.H. Kim: J. of Materials Processing Technology Vol. 140(2003), p. 447.
[3] M. Rauch, J.Y. Hascoet and J.C. Hamann: Int. J. of Material Forming Vol. 11(2008), p. 1191.
[4] C. Henrard, A.M. Habraken and A. Szekeres: Advanced Materials Research Vol. 6(2005), p. 533.
[5] Y. Minoru, G. Manabu and S.Y. Atsumi: J. of Materials Processing Technology Vol. 199(2008), p.163.
[6] G. Ambrogioa, I. Costantino, L. Filice and M. Muzzupappa: J. of Materials Processing Technology Vol. 153(2004), p. 501.
[7] H. Iseki: J. of Materials Processing Technology Vol. 111(2001), p. 150.
[8] J.H. Mo and F. Han: China Mechanical Engineering Vol. 19(2008), p. 491.(In Chinese)
[9] G. Hirt, J. Ames, M. Bambach, and R. Kopp: Annals of the CIRP Vol. 53(2004), p. 203.

*Advanced Materials Research Vols. 201-203 (2011) pp 103-107*
*© (2011) Trans Tech Publications, Switzerland*
*doi:10.4028/www.scientific.net/AMR.201-203.103*

# The Research and Realization of Efficient DDA Interpolation Algorithm for Multi-Axis Linear Linkage

Xiaoling Yan[1,a] , Jiaying Zhang [2,b] and Wanglong Wang [2,c]

[1]College of Mechanical Engineering, Beijing Technology and Business University, Beijing, China 102488

[2]Department of Equipment Remanufacturing, Academy of Armored Force Engineering, Beijing, China 100072

[a]yanxl@th.btbu.edn.cn [b]jyzhang0218@sohu.com [c]wwlwyd2002@sina.com.cn

**Keywords:** Efficient DDA Interpolation; Multi-Axis Linear Linkage; Left Normalized; The Maximum Amount of Movement

**Abstract.** A new efficient interpolation algorithm for multi-axis linear linkage is proposed in this paper, which uses the principle of DDA algorithm, its function be extended and improved. the left normalized data is used in this algorithm, the maximum amount of movement is used as the basis for the calculation of speed, the efficiency of the interpolation is improved and the uniformity of speed is ensured. At last machining result are presented, which shows that this algorithm is powerful to machine spherical surfaces and planes.

## Introduction

The interpolation principle is a very important component of CNC technology, there are a variety of interpolation methods, such as data sampling interpolation method, point by point comparison, the digital integration method (e.g. DDA interpolation) and other interpolation methods, each interpolation method has its advantages and disadvantages.

DDA interpolation method is characterized by its function can be expanded easily, is very convenient to achieve the second curve and multi-axis linear interpolation[1], so the DDA interpolation get widely applied in CNC contouring control , but the drawback is that the feed rate fluctuations, the error is large also. A new efficient interpolation algorithm for multi-axis linear linkage is proposed in this paper, which uses the principle of DDA algorithm, its function be extended and improved, so the uniformity of machine speed can be ensured and the efficiency of interpolation, the machining accuracy of work piece increased.

## Efficient DDA interpolation algorithm for spatial line

**Mathematical model.** Without loss of generality, set the intersecting line L of any two space planes, as shown in Fig. 1.

Set the equation of plane $\Pi_1$ is:

$$A_1 x + B_1 y + C_1 z = 0 \tag{1}$$

Set the equation of plane $\Pi_2$ is:

$$A_2 x + B_2 y + C_2 z = 0 \tag{2}$$

Therefore, the general form equation of line L is:

$$\begin{cases} A_1 x + B_1 y + C_1 z = 0 \\ A_2 x + B_2 y + C_2 z = 0 \end{cases} \tag{3}$$

If the starting point of spatial line doesn't coincide with the origin of coordinate system, we can translate the xyz axes[2], so that the spatial line become a line through the origin in the new coordinate system X'Y'Z', as shown in Fig. 2, this form of spatial line is called the desired standard form.

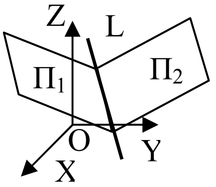

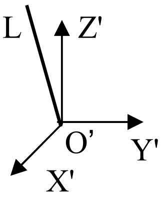

Fig. 1 Description of the spatial line Fig. 2 The standard form of spatial line

**Interpolation algorithm for spatial line in standard form.** We have gotten the standard form of spatial line which discussed above, suppose that we want to make pulse distribution along a line in the X'Y'Z' coordinate system, the starting point of the line is the coordinate origin O, end point is E ($x_e$, $y_e$, $z_e$), as shown in Fig. 3.

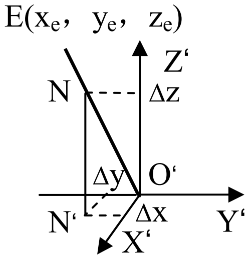

Fig. 3 The interpolation process of spatial line

Assume that $v_x$, $v_y$ and $v_z$ represent the speed of dynamic point N in X, Y and Z direction respectively, therefore the small increment of moving distance Δx, Δy, Δz in the X, Y and Z direction should be:

$$\begin{cases} \Delta x = v_x \Delta t \\ \Delta y = v_y \Delta t \\ \Delta z = v_z \Delta t \end{cases} \tag{4}$$

$$\frac{v_x}{X_e} = \frac{v_y}{Y_e} = \frac{v_z}{Z_e} = K \tag{5}$$

Where, K is proportional coefficient, in the time Δt, Parametric equation of displacement increment in x、y and z direction is :

$$\begin{cases} \Delta x = kx_e \Delta t \\ \Delta y = ky_e \Delta t \\ \Delta z = kz_e \Delta t \end{cases} \tag{6}$$

The process of the dynamic point N moving from the origin to the end point E can be considered as the cumulative results of each coordinate with increment of $kx_e$, $ky_e$ and $kz_e$ every Δt time interval, after summing up m times, x, y, z reach the terminal E ($x_e$, $y_e$, $z_e$) respectively, the following equations established:

$$\begin{cases} X = k\sum_{i=1}^{m} X_e \Delta t = kX_e m = X_e \\ Y = k\sum_{i=1}^{m} Y_e \Delta t = kY_e m = Y_e \\ Z = k\sum_{i=1}^{m} Z_e \Delta t = kZ_e m = Z_e \end{cases} \tag{7}$$

Therefore mk = 1, Eq. 7 shows that the proportion coefficient k and the time of accumulation m is a reciprocal relationship. Because m must be an integer, so k must be a decimal. The main consideration in selecting k is that increments Δx or Δy, Δz is less than 1, in order to ensure that the feed pulse distributed to each axis every time does not exceed one unit step, e.g.

$$\begin{cases}\Delta x = kX_e < 1 \\ \Delta y = kY_e < 1 \\ \Delta z = kZ_e < 1\end{cases} \tag{8}$$

Where, the maximum allowable value of $x_e$, $y_e$ and $z_e$ are limited by bits of controller and bytes in which coordinate values are stored. In general, if we suppose the register is n-bits, the maximum allowable value of $x_e$, $y_e$ and $z_e$ shall be $2^n$-1 (bits are all 1), if we take:

$$k = \frac{1}{2^n} \tag{9}$$

This will meet the requirements of Eq. 8, so that, not only the coefficient *K* can be determined , but also the requirement of Δx, Δy and Δz is less than 1 can be ensured. Therefore, the time of accumulation m which the tool from the origin to the end point will be:

$$m = \frac{1}{k} = 2^n \tag{10}$$

The key components of DDA interpolator are accumulator and integrated function register. An accumulator and a integrated function register are required in each coordinate direction. In general, before the start of interpolation, the accumulator is cleared, $x_e$, $y_e$, $z_e$ are stored in the registers respectively; after the start of interpolation, the contents stored in the integrated function registers will be added once in the corresponding accumulator with the arrival of each pulse Δt, the overflow after adding be regarded as feed pulse Δx (or Δy, Δz) that driving the corresponding axis, while the remainder are still stored in the accumulator; when the cumulative number of pulses m sent by the pulse source is just equal to the integrated function register's capacity of $2^n$, the overflow pulses is equal to the end coordinate value measured by pulse equivalent (the smallest unit ),the tool run to the end point.

## Discussions

During the process of DDA linear interpolation, the time interval of each program segment is fixed , This is because the accumulate operations($m=2^n$ ) must be finished, regardless of the length of Processing travel, so when the stroke is long , the tool run quickly, when the stroke is short ,the tool run slowly, the feed rate of each program segment is inconsistent, this will affect the quality of machining surface, the productivity of program segment which has short stroke is very low especially, in order to overcome this drawback, make the overflow pulse uniform, improve the overflow rate, the following two measures are taken in the efficient DDA interpolation algorithm.

**Left normalized data**. When the value of the integrated function is small, the there are i zeroes before the decimal point , these zeroes should be removed from the integrated function register, this is the process of left normalized data stored in the register.

The definition of normalized data: the MSB(Most Significant Bit) of number stored in register is 1;

The definition of non-normalized data: the MSB of number stored in register is 0.

When the value of the integrated function along X, Y or Z axis is small, shift these data left, when one of the coordinate values becoming normalized data, stop shifting left, when one bit of the data be shifted left, the value of the data will be doubled, p-bits be shifted left, the value will be $2^p$ times. Because $\Delta x=kx_e$, $k=1/2^n$, when p-bits have been shifted left, $\Delta x = k\, x_e 2^p = x_e /2^{n-p} = k' x_e$ , $k'=1/2^{n-p}$, so the time of accumulation $m=2^{n-p}$, the integrated function be shift left p-bits, the time of accumulation be reduced p times[3]. In order to ensure the integrated function which has been shifted left can reach the end point, the counter determining the end should be shift right at the same time. After the process of left normalized data, not only the overflow rate has been improved , but also the overflow pulse has become more uniform.

**The maximum amount of movement is used as the basis for calculation of speed.** During the process of conventional DDA interpolation, the synthesis feed rate fluctuations often, even if the data is normalized left, the speed fluctuations still exist. This is mainly due to there are some NULL operations during the process of interpolation operation, that is, in some interpolation cycle, the accumulator does not overflow, there is no feed axis, there is big variation in axis's speed, the efficiency of interpolation is low.

During the process of efficient DDA interpolation, the maximum amount of movement is used as the basis for calculation of speed, in each interpolation cycle, the axis having the maximum amount of movement has a pulse output, there is no phenomenon of NULL operations, so the interpolation efficiency is improved, the uniformity of speed is ensured.

If three are three movement axes, the amount of movement were $\Delta x$, $\Delta y$, $\Delta z$ respectively. Write $M = \max(\Delta x, \Delta y, \Delta z)$, $M = M + 1$. The accumulators were assigned initial value of $u = \Delta x$, $v = \Delta y$, $w=\Delta z$ respectively.

The contents stored in the integrated function registers will be added once in the corresponding accumulator with the arrival of each pulse $\Delta t$, then compared these values with M, if they are greater than or equal to M, the corresponding shaft output a pulse, while minus M from the data stored in the accumulator, to prepare for the next operation. At the same time, the interpolation pulse count minus 1, while the interpolation is not completed, this process is repeated until the interpolation complete. When the interpolation pulse count is reduced to 0, the interpolation complete.

If there is a line OE, it's starting point is the origin O (0,0,0), end point is E (4,3,4)., Assuming the number of bits for the accumulator and registers is 3, the maximum storage value is 7 ($J \geq 8$ overflow). If using the conventional DDA linear interpolation, it will requires 8 cycles, of which three cycles is NULL operations, there is no pulse output, interpolation calculation process is shown in Table 1, $J_E$ represents the counter determining the end, $J_{VX}$, $J_{VY}$, $J_{VZ}$ represents the integrated function register of x, y, z direction respectively, $J_{RX}$, $J_{RY}$, $J_{RZ}$ represents the accumulator of the x, y, z directions respectively.

While using the high efficient DDA linear interpolation algorithm, it requires only four cycles and each cycle has pulse output, so that a smooth tool movement can be obtained. Interpolation calculation process is shown in Table 2.

Table 1 Conventional DDA linear interpolation calculation process

| X Integrator | | | Y Integrator | | | Z Integrator | | | $J_E$ |
|---|---|---|---|---|---|---|---|---|---|
| $J_{VX}$ | $J_{RX}$ | $\Delta X$ | $J_{VY}$ | $J_{RY}$ | $\Delta Y$ | $J_{VZ}$ | $J_{RZ}$ | $\Delta Z$ | |
| 4 | 0 | | 3 | 0 | | | 0 | | 8 |
| 4 | 0+4 | | 3 | 0+3 | | 4 | 0+4 | | 7 |
| 4 | 4+4 | 1 | 3 | 3+3 | | 4 | 4+4 | 1 | 6 |
| 4 | 0+4 | | 3 | 6+3 | 1 | 4 | 0+4 | | 5 |
| 4 | 4+4 | 1 | 3 | 1+3 | | 4 | 4+4 | 1 | 4 |
| 4 | 0+4 | | 3 | 4+3 | | 4 | 0+4 | | 3 |
| 4 | 4+4 | 1 | 3 | 7+3 | 1 | 4 | 4+4 | 1 | 2 |
| 4 | 0+4 | | 3 | 2+3 | | 4 | 0+4 | | 1 |
| 4 | 4+4 | 1 | 3 | 5+3 | 1 | 4 | 4+4 | 1 | 0 |

Table 2 Efficient DDA linear interpolation calculation process （M=5）

| X Integrator | | | Y Integrator | | | Z Integrator | | | $J_E$ |
|---|---|---|---|---|---|---|---|---|---|
| $J_{VX}$ | $J_{RX}$ | $\Delta X$ | $J_{VY}$ | $J_{RY}$ | $\Delta Y$ | $J_{VZ}$ | $J_{RZ}$ | $\Delta Z$ | |
| 4 | 4 | | 3 | 3 | | 4 | 4 | | 11 |
| 4 | 4+4 | 1 | 3 | 3+3 | 1 | 4 | 4+4 | 1 | 8 |
| 4 | 3+4 | 1 | 3 | 1+3 | | 4 | 3+4 | 1 | 6 |
| 4 | 2+4 | 1 | 3 | 4+3 | 1 | 4 | 2+4 | 1 | 3 |
| 4 | 1+4 | 1 | 3 | 2+3 | 1 | 4 | 1+4 | 1 | 0 |

When using high efficient DDA interpolation method, before the interpolation operations, firstly determining the movement direction of each axis according to the tool's current position and the end position of interpolation, then the result is delivered to the motor driver of the corresponding shaft ;

secondly comparing the distance of each axis interpolation with the pulse equivalent, make a conversion, that is to say converting the distance to the corresponding number of pulses, then all movement axes' numbers of pulse involved in interpolation are added, their sum is regarded as an input parameters of the interpolation calculation (initial value of $J_E$). By comparing table 1 and table 2, we can see that using efficient DDA interpolation not only the interpolation speed is improved , but also the machine run smoothly, at the same time the interpolation accuracy is improved.

## Features of the hardware for realization of efficient DDA interpolation algorithm

Dual-CPU system has been used in the hardware system[4,5],the main CPU (MB90F346RSA) calculate the pulse period and the maximum amount of movement M, then The amount of movement of each axis and the value of M are transmitted from the main CPU to the Subordinate CPU (STC12C5404).The main CPU output fixed pulses which doesn't take up the resources of the main CPU, the Subordinate CPU make the interpolation calculation in each pulse cycle.

## Conclusion

The algorithm above has been realized by C programming language, we machining planes and spherical surfaces in vertical lift axis CNC milling machine( KRN XK5025), achieved good results. Machining results show that the efficient DDA algorithm for multi-axis linear linkages proposed in this paper is very effective, it has high efficiency of interpolation , smooth running during the process of machining, high precision of machining work piece, it is a interpolation algorithm that suitable for implementation in the NC system.

## Acknowledgement

The financial support of Beijing Natural Science Foundation (4062011) and Foundation for Young Teachers of Beijing Technology and Business University are gratefully acknowledged.

## References

[1] Information on http://www.busnc.com/ly/DDA/zhixian.htm（In Chinese）.

[2] dehua He, hongzan Bin, J.China Mechanical Engineering vol.5(4)(1994), p.11（In Chinese）.

[3] Ferrari M, Lemaitre G. Active optics methods for highly aspheric mirrors. In: Proceedings of SPIE the International Society for optical Engineering, 2000, 4003(5):34~42.

[4] X.Ai. Development and Application of High Speed Machining Technology. In: Proceedings of the International Conference on High Speed Machining, 2004:21~28.

[5] H.Schulz. Why High Speed Cutting. In: Proceeding of the International Conference on High Speed Machining, 2004:1~8.

*Advanced Materials Research Vols. 201-203 (2011) pp 108-112*
*© (2011) Trans Tech Publications, Switzerland*
*doi:10.4028/www.scientific.net/AMR.201-203.108*

# Finite Element Analysis on Structural Stress of 8×8 InSb Infrared Focal Plane Array with Underfill

Qingduan Meng[a], Ligong Sun and Jiexin Pu

School of Electronic Information Engineering, Henan University of Science and Technology, 471003, Luoyang, China

[a]qdmengly@mail.haust.edu.cn

**Keywords:** Finite Element Analysis; Focal Plane Array; Insb; Stress Concentration

**Abstract.** Based on viscoplastic Anand's model, the structural stress of 8×8 InSb infrared focal plane array (IRFPA) detector is systemically analyzed by finite element method, and the impacts of design parameters including indium bump diameters, heights and InSb chip thicknesses on both Von Mises stress and its distribution are discussed in this manuscript. Simulation results show that the maximum stress existing in InSb chip reaches minimum with indium bump diameter 32μm. Under this condition, for the fixed indium height, as the InSb chip thickness reduces from 21μm to 9μm in step of 3μm, Von Mises stress maximum values of InSb chip seems increases gradually, and when the indium bump height reduces from 21μm to 9μm in step of 3μm, its maximum Von Mises stress increase at random increment, do not show certain rules, and indium bump height seems to have a comparable effect on stress value with InSb chip thickness. When indium diameter, height and InSb chip thickness are set to 32μm, 15μm, and 12μm, respectively, the maximal Von Mises value existing in InSb chip reaches minimal value 628MPa, simultaneously the stress distribution at the contacts areas is uniform and concentrated, and this structure is promising to avoid device invalidation.

## Introduction

Indium antimonide (InSb) pn junctions are widely used as infrared photovoltaic detectors and imaging sensors for the 3-5μm spectral range [1,2]. To increase sensitivity and spatial resolution, photovoltaic diodes are usually placed in rectangular array or square array, then via indium bumps, assembled to a silicon readout integrated circuits (ROIC), after that underfill is dispensed between InSb die and Si ROIC substrate for increasing the reliability of flip-chip packaging. To obtain the lowest level of electronic noise possible to approach the photon noise limit, it is necessary to cryogenically cool the infrared focal plane array (IRFPA) to liquid nitrogen temperature (77K). Therefore, fracture in InSb chip usually occurs with the rapid temperature dropping process, due to the mismatch in the coefficients of thermal expansion between the silicon multiplexer and the InSb detector array, which will cause shearing mechanical strain on the bumps as the array is cooled to cryogenic temperatures. In order to reduce the InSb chip fracture possibility and improve the producibility, it is necessary to analyze the induced thermal strain and stress values and its distribution in InSb chip. At present time, the thermo-mechanical reliability of flip-chip assemblies is usually assessed by finite element simulations in conjunction with experimental verification, that is, basing on the strain and stress analysis, the structure reliability is assessed [3,4].

In 2009, Rui Wu Chang research group delivers the constitutive relations of indium in extreme-temperature in Anand's model [5], a rate and temperature dependent constitutive model, applied to represent the inelastic deformation behavior of indium at low temperatures down to -150℃. Based on the above research results, the structural stress of 8×8 InSb array detector with underfill dependent on both indium bump sizes and InSb thickness is systemically researched by finite element method, all these for finding the optimal structural sizes to avoid thermal stress concentration in InSb chip.

## Model Creation and Parameters Selection

When creating the finite element analysis model of InSb IRFPA detector, indium bumps are assumed to be octagonal prisms, and no defects existing in the whole device. InSb IRPFA is composed of InSb photodiode arrays, indium bumps array, Si ROIC and underfill encapsulant materials, just as shown in Fig. 1. InSb chip dimensions are 400μm×400μm×(9~21)μm, and attached to Si ROIC substrate with 8×8 indium bumps array, Si ROIC substrate dimensions are 500μm×500μm×300μm, indium bumps diameter has fixed at 32μm with 50μm pitch, and its height increases from 9μm to 21μm in step of 3μm. When the diameter of indium bump height is set at 32μm, the maximal Von Mises value existing in InSb chip reaches minimal values and its stress distribution is uniform at contacting areas between InSb chip and indium bump [6]. Here underfill encapsulant is dispensed between InSb die and Si ROIC substrate for increasing the reliability of flip-chip packaging. In order to describe the mesa structure locating between neighboring detectors elements, a triangular prisms, whose cross section area sides length are 2.83μm, 2.83μm and 4μm, respectively, are employed. Just as shown in Fig.1. Using the geometrical symmetry, only one eighth of the overall package is modeled. One eighth models contain 6 full and 4 half indium bumps.

InSb IFFPA finite element analysis model is created by top down method, that is, model is made up of block volume, then Booleans operation is used to divide the block, after than the glue command realizes the contacts between any neighboring components.

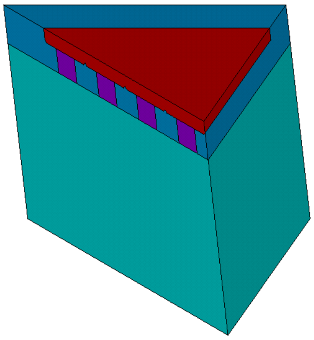

Fig. 1. Three dimensional model of infrared focal plane array device.

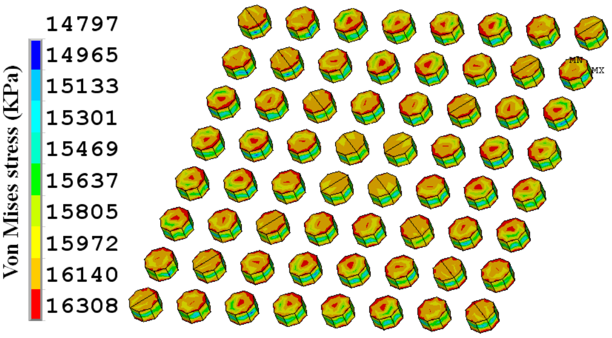

Fig. 2. Von Mises stress distribution of 3-D indium bumps.

Table 1 Liner elastic material parameters

| Materials | *Elastic modulus [E/Mpa]* | *Poison's ratio [μ]* | *CTE [$\alpha_1$ ppm/K]* |
|---|---|---|---|
| Si ROIC | 163000 | 0.28 | 2.50 |
| InSb chip | 409000 | 0.35 | 5.04 |
| Indium bump | 10600 | 0.45 | 33.00 |
| underfill | 9000 | 0.3 | 26.00 |

InSb chip, Si ROIC substrate and underfill are all considered to be linear elastic materials. All the employed parameters listed in table 1, E is the Young's modulus, μ is the Poisson's ratio, and CTE is the coefficient of thermal expansion (CTE). Flip chip process is completed at 370K, at this temperature, no residual stress is assumed to exist within the package. In the simulation, the temperature is gradually reduced from 370K to 77K, which causes thermal stresses to develop. Throughout the temperature drop, no transient heat transfer is considered and the temperature within the model is assumed to be uniform. About 71 seconds increments are taken to lower the temperature to ensure the accuracy. Horizontal displacements normal to the symmetrical surfaces are set to zero, at the same time, the displacement of Si ROIC substrate bottom surface center point remains zero.

Indium bump deformation is strongly temperature and time dependent, and associated with the irreversible, temperature and rate dependent inelastic characteristics, which are known to be viscoplastic [7-9]. Here Anand's viscoplastic constitutive model has been used to describe mechanics of constitutive relationship of indium bump [10, 11].

## Simulation Results Analysis

When temperature of InSb IRFPA is gradually reduced from 370K to 77K in 71 seconds, Von Mises stress distribution of indium bumps is illustrated in Fig. 2. The maximal Von Mises stress difference (1.6MPa) among indium arrays is so small that the Von Mises stress distribution is assumed to be uniform. The maximal Von Mises stress locating on the indium bump bottom surface locating at the second row and eighth column intersection, which neighbors on the indium bump with the longest distance to neutral point on the chip, so has almost the largest induced thermal stress.

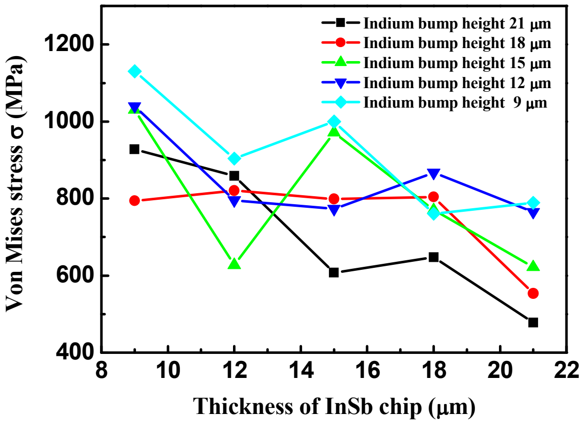

Fig. 3. Von Mises stress maximum values of InSb chip as a function of InSb thickness with varied indium bump standoff height.

In order to learn the effects from both indium bump height and InSb chip thickness on Von Mises stress value and its distribution in InSb chip, here the height of indium bump reduces from 21μm to 9μm in step of 3μm, and InSb chip thickness also decreases from 21μm to 9μm in step of 3μm. For any structure, model meshing, constraints, loading are identical for comparison of simulation results, just as shown in Fig. 3. For a fixed indium height, as the InSb chip thickness reduces from 21μm to 9μm, Von Mises stress maximum values of InSb chip seems increases gradually for indium bump height with 21μm, 15μm and 9μm, yet for indium bump height with 12μm, when the InSb chip thickness reduces from 12μm to 9μm, the Von Mises stress increases sharply, besides, the stress seems to have nothing to do with InSb chip thickness, and fluctuates at 800MPa, for indium bump height with 18μm, when the InSb chip thickness reduces from 21μm to 18μm, the Von Mises stress also increases sharply, besides, the stress also seems to have nothing to do with InSb chip thickness, and also fluctuates at 800MPa. When the indium bump height reduces from 21μm to 9μm in step of 3μm, the maximum Von Mises stress values increase at random increment, do not show certain rules, and indium bump height seems to have a comparable effect on maximal stress value with InSb chip thickness. To take account of the absorption coefficient for InSb material in middle wavelength infrared changes between $2\times10^{3}$ cm$^{-1}$ and $3\times10^{3}$ cm$^{-1}$, thus the corresponding light penetration depth is about 5μm and 3.3μm [12], according to absorption rule, once light transmits in the media for three penetration depths, it will be completely absorbed, so in this paper, we focus on InSb chip thickness from 9μm to 15μm. Apparently when indium diameter, height and InSb chip thickness are set to 32μm, 15μm, and 12 μm, respectively, the maximal Von Mises value existing in InSb chip reaches minimal value 628MPa. And now Von Mises stress distribution of InSb chip, underfill and Si ROIC are shown in Fig. 4 to Fig. 6, respectively.

Apparently, Von Mises stress existing on contact areas between InSb chip and indium bumps is concentrated and uniform, its stress value is about 300MPa, larger than that of its surrounding areas. The maximal stress value about 610MPa situates at the edge far away from neutral point, where the InSb chip is confined by its surrounding underfill encapsulant and does not shrink freely. The minimal stress value about 23MPa locates on the trough intersection zones. There is an obvious stress gradient from contact section center to non-contact region.

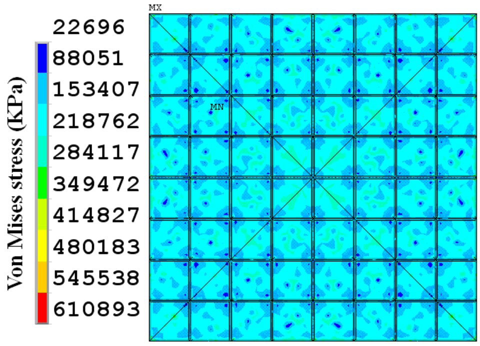

Fig. 4. Von Mises stress distribution of InSb chip bottom surface.

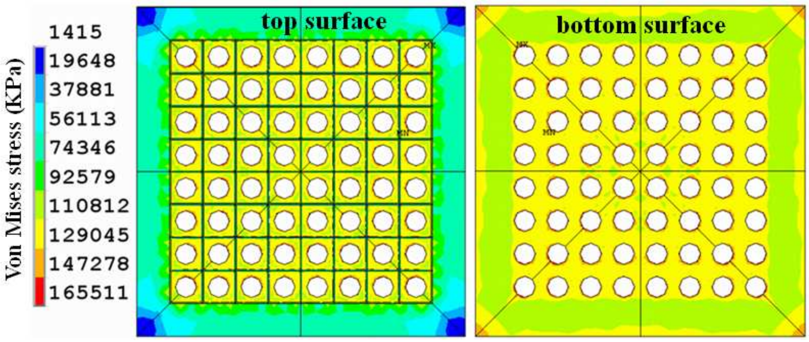

Fig. 5. Von Mises stress distribution of underfill.

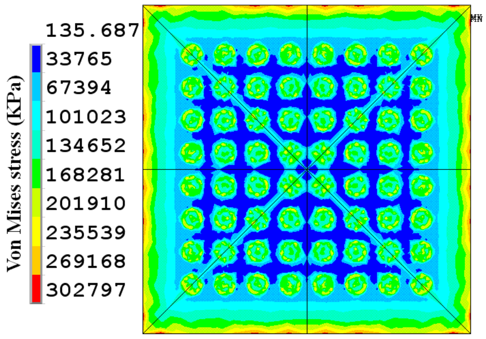

Fig. 6. Von Mises stress distribution of Si-CMOS readout integrated circuit.

Underfill encapsulant is usually dispensed in the gap between InSb chip and Si ROIC to provide mechanical reinforcement and reduce thermal stresses on indium bumps, all these for avoiding fatigue and crack growth during temperature cycles. When the temperature of 8×8 InSb IRFPA drops from 370K to 77K, Von Mises stress distribution in underfill is shown in Fig. 5. On the whole region under InSb chip, the stress distribution is uniform, and its stress value is about 120MPa, but around indium bump octahedral shell, the stress is apparently enlarged with maximal value 165MPa, and its minimum appears on the intersect region of convex triangular prisms, which is made of underfill locating in the troughs etching in InSb chip for isolating the neighboring detector cells. At the four corners of underfill top surface, Von Mises stress is small and no more than 20MPa, here the underfill can shrink freely, as for the four corners of underfill bottom surface, Von Mises stress is correspondingly enlarged for underfill is glued with Si ROIC and do not shrink freely. On the whole, the stress on underfill bottom surface is larger than that on its top surface, which comes from the larger thermal mismatch existing between underfill and Si ROIC. Compared with indium bump array, apparently the underfill bears most thermal strain, for its stress is almost tenfold as large as stress in indium bump array.

Von Mises stress distribution in Si ROIC is almost concentrated strongly on the contacting areas between indium bumps and Si ROIC, around the contacting areas, the Von Mises is so small that it is ignorable, besides, on the quadrilateral borders of Si ROIC top surface, there are several non-continuous spots where Von Mises stress are the largest, especially near the corner of Si ROIC top surface, just as shown in Fig. 6. This is distinctly different from the stress distribution in the structure without underfill, where the stress distribution on the quadrilateral borders of Si ROIC top surface is ignorable [13].

## Conclusion

Crack appearing in the InSb chip limited the InSb IRFPA final yield. Basing on finite element analysis, impacts on Von Mises stress and its distribution in the InSb IRFPA from the structure parameters, including indium bump diameters, heights and InSb chip thicknesses, are completely discussed in this manuscript. Simulation results show that as the indium diameter, standoff height and InSb thickness are set to 32μm, 15μm and 12μm, respectively, the maximal Von Mises value existing in InSb chip reaches minimal values 628MPa, and its stress distribution is uniform at all the contacting areas. These are favorable to reduce the crack happening in InSb chip, and improve the yield rate.

## References

[1] Gau Y. T., Dai L. K., Yang S. P., Weng P. K., Huang K. S. et al: Proceedings of The International Society for Optical Engineering, Vol. 4078 (2003), p. 467

[2] Parrish W. J., Blackwell J. D., Kincaid G. T. and Paulson R. C.: Proceedings of the International Society for Optical Engineering, Vol. 1540 (1991), p. 274

[3] J. H. L. Pang and D.Y.R. Chong: IEEE Transactions on Advanced Packaging, Vol. 24(4) (2001), p. 499

[4] Z. Zhang and C. P. Wong: IEEE Transactions on Advanced Packaging, Vol. 27(3) (2004), p. 515

[5] R. W. Chang and F. Patrick Mccluskey: Journal of Electronic Materials, Vol. 38(9) (2009), p.1855

[6] L. G. Sun, C. Meng and Q. D. Meng: Journal of Advanced Materials Research (2011), in press.

[7] S. Kim and H. Ledbetter: Materials Science and Engineering A, Vol. 252 (1998), p.139

[8] E. B. Hermida, D. G. Melo, J. C. Aguiar and D. E. Lopez: Journal of Alloys and Compounds, Vol. 310(1) (2000), p. 91

[9] R. P. Reed, C.N. McCowan and R. P. Walsh: Materials Science and Engineering, Vol. 102(2) (1988), p.227

[10] G. Z. Wang, Z. N. Cheng, K. Becker and J. Wilde: Journal of Electronic Packaging, Vol. 123(3) (2001), p.247

[11] Wilde J., Becker K., Thoben M., Blum W., Jupitz T., Wang G. and Cheng Z. N.: IEEE Transactions on Advanced Packaging, Vol. 23(3) (2000), p.408

[12] Antoni Rogalski: Progress in Quantum Electronics Vol. 27 (2003), p.59

[13] Q. D. Meng, X. L. Zhang, X. L. Zhang and W. G. Sun: Applied Mechanics and Materials Vol. 33-34 (2010), p.207

*Advanced Materials Research Vols. 201-203 (2011) pp 113-116*
*© (2011) Trans Tech Publications, Switzerland*
*doi:10.4028/www.scientific.net/AMR.201-203.113*

# Research on 3D Reconstruction of the Facial Surface Reverse Engineering

Jie Yang [1,2, a], Lei Zhao [1, b]

[1]Mechanical and Electronic Information Faculty, China University of Geosciences,

Wuhan, 430074, China

[2]School of Engineering, The University of California, Merced, California, 95343, U.S

[a]flyyangj@163.com, [b] flea0816@163.com

**Keywords:** 3D Facial Reconstruction; Reverse Engineering; Laser Digitizing Technology

**Abstract:** According to the surface integration of laser technology and computer-aided design and computer-aided manufacturing technology (CAD & CAM), a method that is rebuilt surface of three-dimensional facial reconstruction has been explored. A laser scanning system is used to collect the 3D discrete point data of the facial model, which will be cut up by their characteristics and curvature in order to make a 3D face reconstruction. The maximum reconstructive error is 0.2174mm. Application results indicate that the proposed method is quite satisfactory for facial reconstructive surgery, rehabilitation design and plastic surgery.

## Introduction

With the scientific and technological development, more and more advanced manufacturing technology participate in the medical technology field, such as reverse engineering, rapid prototyping technology and laser digitizing technology. Laser digitizing technology brings a particularly wide range of applications, which can provide modeling support for the medical industry. At present, 3D surface reconstruction of the face for many researchers has become the challenging subject [1]. The model can be used to simulate oral and maxillofacial surgery plastic surgery. Using rapid prototyping technology to create the complex surface models of human face, the communication between doctors and physicians, or doctors and patients, can not only be finished by the computer virtual technology, but also the 3D simulated surgery.

In this paper, based on the research of 3D Data acquisition method, a feasibility plan has been proposed that the point cloud is divided according to the characteristics of facial features and curvature. This method is fully different from the traditional way constructing patches from mesh lines and blending [2]. After analyzing the error between the original data and the reconstruction model, the results show that the method proposed in this paper can meet the clinical medicine requirements of Oral and Maxillofacial Surgery, facial plastic surgery on the precision and error.

## Data Acquisition

**System Composition and Working Principle.** The 3D surface reconstruction system mainly consists of two parts: A, data acquisition section. JS654N-type coordinate measuring instrument, with the Japanese origin of pairs of CCD, the U.S. imported laser generator, measurement accuracy is 0.02mm, working distance is 150mm, resolution is 768 × 576PAL, and scanning speed is 1500 points / sec. B, the data processing section. Computer ASUS (Intel Duo T6400, Memory 2G, Hard disk 320G), Windows XP OS, reverse engineering software (installing *Scan Manager* and *Imagerware V12.0).*

Fig. 1 shows the use of triangulation to obtain the basic principles of three-dimensional coordinates [3, 4]. The light issued by the laser passes through the amplitude grating components paralleling like the equidistant straight lines or interferometer, and forms a linear interference fringes projected onto the object**.** Because the changes of surface curvature or depth bring stripe deformation, the use of CCD (Charge Coupled device image sensor) camera could get the picture of this deformed fringe images. The data, such as measured point distance or location coordinates, can be obtained by the triangular geometric relations according to the laser beam's angle and imaging position in the CCD.

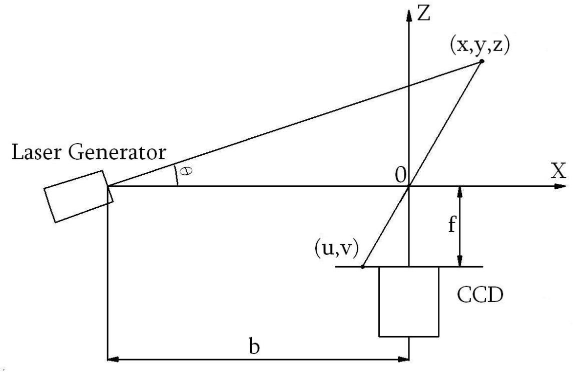

**Fig. 1** Principle of 3D coordinate measurement

The figure above, the origin of measurement coordinate system is the center point of CCD camera lens, $(x, y, z)$ is an arbitrary point on the surface, $(u, v)$ is imaging point of $(x, y, z)$ in the CCD camera, $f$ is the camera focal length, $b$ is the distance between laser projection center (light source) and the camera center, $\theta$ is the angle between the X-axis and a straight line which is formed by the measured point and the light source center. $b$, $f$, $\theta$ are the system parameters which are obtained through the calibration, $u$ and $v$ are the coordinate figures of image points on the sensitive surface of the CCD camera.

In the X-0-Z plane:

$$\frac{f}{u}=\frac{z}{x},\quad \frac{b+x}{z}=\cot\theta \qquad (1)$$

In the Y-0-Z plane:

$$\frac{f}{v}=\frac{z}{y},\quad \frac{x}{y}=\frac{u}{v} \qquad (2)$$

Therefore, 3D coordinates $(x, y, z)$ of the measured points can be obtained:

$$(x,y,z)=\frac{b}{f\cot\theta-u}(u,v,f) \qquad (3)$$

**Facial Three-Dimensional Data Acquisition.** Because the existing laser scanning range is limited, a facial surface model by 1:3 scaled down becomes the object of data acquisition in this paper. The scan parameters, the scan range and accuracy of the images acquisition can be set up according to clinical needs. Being selected the front of the face model as the main scanning direction, the mainly scan range is between the two ears and between chin and forehead. The scanning result is shown in Fig. 2 which is formed by 49954 points, and the file format is " *.asc ". The process of 3D surface reconstruction is shown in Fig. 3.

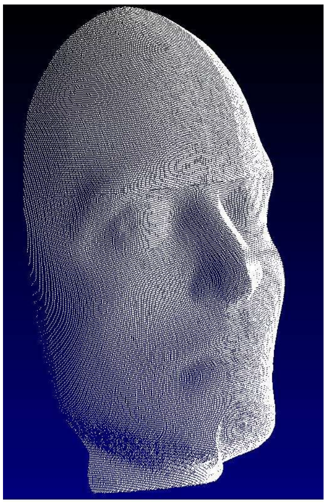

**Fig. 2** Point cloud of facial 3D coordinate

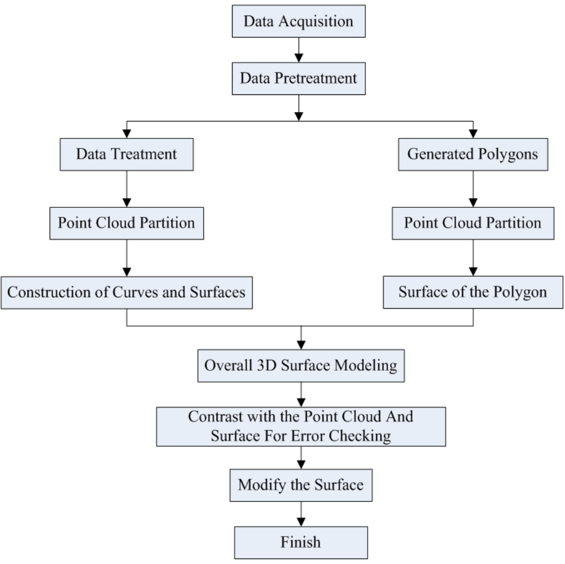

**Fig. 3** Process of 3D surface reconstruction

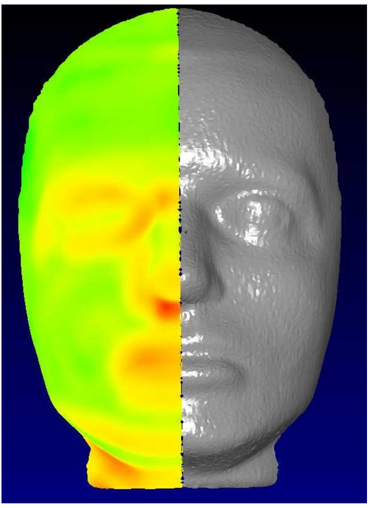

**Fig. 4** Result of curvature analysis of point cloud

## Facial Surface Reconstruction and Error Analysis

In this paper, reverse engineering software *Imageware* is used to carry out data processing and analysis. Throughout the measurement process, there are some random factors in addition to the accuracy of machine itself, such as some miscellaneous points. Therefore, before restoring into the CAD 3D model, it's necessary to process the point cloud, such as cutting, filtering, simplification, sorting and noise reduction. After processing, the curvature analysis of point cloud is shown in Fig.4, the left shows curvature changes and the right is original points which are shown as the polygonize cloud.

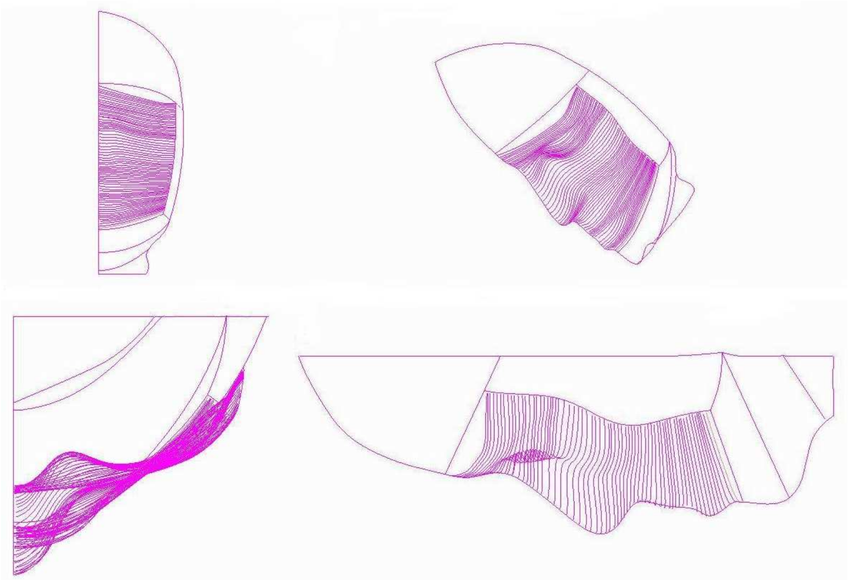

**Fig. 5** Divided curves of facial point cloud according to characteristics of facial features

On account of the facial surface being a symmetrical model, only half of the point cloud need to process on the process of cutting and 3D reconstruction, and the whole 3D model can be reconstructed with the image method. According to the curvature difference, point cloud is classified into one group whose curvature changes smoothly, such as the head, forehead, cheeks and chin. In this way, it will be a great increase of accuracy, because the eyes, nose and mouth have